

VARIABLE AMPLITUDE FATIGUE ANALYSIS USING SURROGATE MODELS AND
EXACT XFEM REANALYSIS

By

MATTHEW JON PAIS

A DISSERTATION PRESENTED TO THE GRADUATE SCHOOL
OF THE UNIVERSITY OF FLORIDA IN PARTIAL FULFILLMENT
OF THE REQUIREMENTS FOR THE DEGREE OF
DOCTOR OF PHILOSOPHY

UNIVERSITY OF FLORIDA

2011

© 2011 Matthew Jon Pais

To my mother and father who have always supported me in all that I have done

ACKNOWLEDGMENTS

I would first and foremost like to thank my advisor Dr. Nam-Ho Kim for his valuable insights and patience with me as we faced our challenges. He has prepared me to solve real world problems and he deserves many thanks.

Dr. Timothy Davis and Nuri Yeralan from the Computer Science Department at the University of Florida for their assistance in the creation and implementation of the exact XFEM reanalysis algorithm for quasi-static crack growth and optimization.

I would also like to thank the members of the Multidisciplinary Design and Optimization group at the University of Florida for their invaluable comments during my rehearsals. Extra thanks go to Dr. Alexandra Coppé and Dr. Felipe Viana for our collaboration during my time as part of the group.

Dr. Benjamin Smarslok at the Air Force Research Laboratory at Wright-Patterson Air Force Base for providing acceleration and velocity data from aircraft flights which were used to create data for the variable amplitude fatigue analysis.

Richard Pippy for the original creation of the wing box finite element model which was subsequently modified for use in the analysis of an airplane wing subjected to a variable amplitude fatigue analysis.

Dr. Nagaraj Arakere, Dr. Youping Chen, Dr. Timothy Davis, Dr. Raphael Haftka, and Dr. Bhavani Sankar for serving on my committee for their thoughtful insights as I worked toward this dissertation. Extra thanks go to Dr. Haftka for comments which lead to the development of the variable step size kriging algorithm.

Dr. Jorg Peters from the Computer Science Department at the University of Florida for his comments which lead to a conference paper discussing enrichment functions for weak discontinuities independent of the finite element mesh.

TABLE OF CONTENTS

	<u>page</u>
ACKNOWLEDGMENTS.....	4
LIST OF TABLES.....	8
LIST OF FIGURES	10
LIST OF ABBREVIATIONS.....	15
ABSTRACT.....	16
CHAPTER	
1 INTRODUCTION.....	18
Motivation.....	18
Fatigue Crack Growth.....	20
Computational Fracture Mechanics	26
Scope	28
Outline.....	30
2 THE LEVEL SET METHOD.....	32
Level Set Method for Closed Sections	32
Level Set Method for Open Sections	34
Summary.....	36
3 THE EXTENDED FINITE ELEMENT METHOD.....	37
General Form of the Extended Finite Element Method	37
Enrichment Functions.....	40
Crack Enrichment Functions	41
Inclusion Enrichment Functions.....	45
Void Enrichment Function	49
Integration of Element with Discontinuity	50
XFEM Software	52
Abaqus®	52
MATLAB® XFEM Code (MXFEM).....	54
Other XFEM Implementations	57
Summary.....	58
4 CRACK GROWTH MODEL.....	60
Stress Intensity Factor Evaluation	60
Crack Growth Direction.....	64

Crack Growth Magnitude	66
Finite Crack Growth Increment for Constant Amplitude Loading	67
Direct Fatigue Crack Growth	67
Classical Paris model.....	68
Modified Paris model	69
Equivalent Stress Intensity Factor	72
Integration of Fatigue Crack Growth Model	73
Example problem.....	77
Cycle Counting Methods.....	79
Summary	83
5 SURROGATE MODELS FOR HIGHER-ORDER INTEGRATION OF FATIGUE CRACK GROWTH MODELS.....	85
Integration of Ordinary Differential Equation	85
Surrogate Models	87
Kriging.....	88
Kriging for Integration of Fatigue Crack Growth Law.....	90
Constant Integration Step Size.....	90
Variable Integration Step Size	92
Example Problems	95
Center Crack in an Infinite Plate Under Tension.....	95
Edge Crack in a Finite Plate Under Tension	99
Inclined Center Crack in a Finite Plate Under Tension	102
Summary	105
6 AN EXACT EXTENDED FINITE ELEMENT METHOD REANALYSIS ALGORITHM.....	106
Reanalysis Methods	106
Exact Reanalysis by Modification of an Existing Cholesky Factorization.....	107
Example Problems	115
Reanalysis of an Edge Crack in a Finite Plate.....	115
Optimization for Finding Crack Initiation in a Plate with a Hole	117
Summary	119
7 VARIABLE AMPLITUDE MULTI-AXIAL FATIGUE ANALYSIS OF WING PANEL	121
Scaling of Normalized Flight Data from the Air Force Research Laboratory	121
Finite Element Wing Model.....	124
Wing Pressure Distribution.....	125
Finite Element Stress Analysis of Airplane Wing	133
Surrogate Models for Lift Coefficient, Stress Components, and Surface Area of Pressure Distribution	133
Analysis of Cracked Plate Subjected to Variable Amplitude Multi-axial Load History	135
Summary	142

8	CONCLUSIONS AND FUTURE WORK	145
	Conclusions.....	145
	Future Work.....	147
	Future Development of MXFEM	147
	Possible Application for the Exact XFEM Reanalysis Algorithm	147
	Possible Applications for Surrogate Integration	149
 APPENDIX		
A	MXFEM BENCHMARK PROBLEMS	151
	XFEM Enrichments.....	151
	Center Crack in a Finite Plate.....	151
	Edge Crack in a Finite Plate	153
	Inclined Edge Crack in a Finite Plate	154
	Hard Inclusion in a Finite Plate	155
	Void in an Infinite Plate.....	158
	Other Benchmarks.....	160
	Angle of Crack Initiation from Optimization.....	160
	Crack Growth in Presence of an Inclusion.....	162
	Fatigue Crack Growth	163
B	AUXILIARY DISPLACEMENT AND STRESS STATES.....	165
C	CONVERSION OF NORMALIZED FLIGHT DATA TO SCALED FLIGHT DATA .	166
D	STRESS HISTORIES FOR FLIGHT DATA FROM AFRL	170
	LIST OF REFERENCES.....	177
	BIOGRAPHICAL SKETCH.....	194

LIST OF TABLES

<u>Table</u>	<u>page</u>
5-1. Accuracy of kriging interpolation integration for fixed increment Δa for a center crack in an infinite plate of Al 2024 with $R = 0.5$	97
5-2. Accuracy of kriging extrapolation integration for fixed increment ΔN for a center crack in an infinite plate of Al 2024 with $R = 0.5$	98
5-3. Effect of material and initial crack size on estimated cycles to failure for the variable step size algorithm for a center crack in an infinite plate	99
5-4. Accuracy of kriging interpolation integration for fixed increment Δa for an edge crack in a finite plate of Al 2024 with $R = 0.5$	100
5-5. Accuracy of kriging extrapolation integration for fixed increment ΔN for an edge crack in a finite plate of Al 2024 with $R = 0.5$	101
5-6. Effect of material and initial crack size on estimated cycles to failure for the variable step size algorithm for an edge crack in a finite plate	102
5-7. Comparison of Euler and variable step size predictions for the coordinates (x_{final}, y_{final}) of the right crack tip marked with a dotted circle in Figure 5-6 and cycle number N_{fail} corresponding to a final crack size of 0.6 m from an initial crack size of 0.187 m for four different materials	103
7-1. Maximum and minimum values of normalized and scaled flight data with conversion relationship for Flight ID 152.....	124
7-2. The polynomial coefficients for the chord-wise pressure distribution	128
7-3. Area under the normalized pressure distribution for some angles of attack.....	132
7-4. The stress components for various angles of attack used in the lift and drag pressure distributions	133
7-5. Summary of the AFRL data, the number of cycles identified, and the number of function evaluations for each Flight ID.....	138
A-1. Convergence of normalized stress intensity factors for a full and half model for a center crack in a finite plate	152
A-2. Convergence of normalized stress intensity factors for an edge crack in a finite plate	154
A-3. Convergence of normalized stress intensity factors for an inclined edge crack in a finite plate	155

A-4. Comparison of the theoretical and MXFEM value for maximum energy release angle as a function of average element size	161
C-1. Normalized and scaled flight data with conversion for Flight ID 2	166
C-2. Normalized and scaled flight data with conversion for Flight ID 8	166
C-3. Normalized and scaled flight data with conversion for Flight ID 10	166
C-4. Normalized and scaled flight data with conversion for Flight ID 12	166
C-5. Normalized and scaled flight data with conversion for Flight ID 16	166
C-6. Normalized and scaled flight data with conversion for Flight ID 18	167
C-7. Normalized and scaled flight data with conversion for Flight ID 22	167
C-8. Normalized and scaled flight data with conversion for Flight ID 26	167
C-9. Normalized and scaled flight data with conversion for Flight ID 138	167
C-10. Normalized and scaled flight data with conversion for Flight ID 140	167
C-11. Normalized and scaled flight data with conversion for Flight ID 146	168
C-12. Normalized and scaled flight data with conversion for Flight ID 148	168
C-13. Normalized and scaled flight data with conversion for Flight ID 150	168
C-14. Normalized and scaled flight data with conversion for Flight ID 152	168
C-15. Normalized and scaled flight data with conversion for Flight ID 154	168
C-16. Normalized and scaled flight data with conversion for Flight ID 156	169
C-17. Normalized and scaled flight data with conversion for Flight ID 159	169
C-18. Normalized and scaled flight data with conversion for Flight ID 161	169
C-19. Normalized and scaled flight data with conversion for Flight ID 163	169

LIST OF FIGURES

<u>Figure</u>	<u>page</u>
1-1. Representative S-N curve for a material subjected to cyclic loading	18
1-2. Representation of the Mode I, Mode II, and Mode III opening mechanisms	22
1-3. An example of constant amplitude loading with characteristic parameters such as the maximum and minimum applied stresses and the stress ratio R	23
1-4. An example of an overload followed by an underload and an underload followed by an overload.....	25
1-5. Examples of possible traction-separation models that can be used as part of a cohesive zone model where σ_Y is the yield stress and δ_c is the critical separation	27
2-2. Example of the signed distance functions for an open section	35
3-1. The nodes enriched with the Heaviside and crack tip enrichment functions	42
3-2. One-dimensional bi-material bar problem	48
3-3. Comparison of the various inclusion enrichment functions and locations of the enriched degree(s) of freedom for a one-dimensional bar	48
3-4. Elements containing a discontinuity and the continuous subdomains for integration	51
3-6. Example problem to show plots generated by MXFEM	56
3-7. Example of the level set functions output from MXFEM	57
3-8. Example of the stress contours output from MXFEM	57
4-1. The elements within a specified radius for path-independence	63
4-2. Orientations of the critical and maximum normal stress planes.....	66
4-3. The use of the stress ratio correction factor M_R to condense the various stress ratios R into a single curve corresponding to $R = 0$	70
4-4. The plastic zone and crack sizes which are used in the modified Paris model to account for the effect of crack tip plasticity during load interactions.....	71
4-5. Plate with a hole subjected to tension to examine the effects of mesh density, crack growth increment, and number of elapsed cycles upon the convergence of crack path	78

4-6. Convergence of crack path as a function of the mesh density, crack growth increment, and number of elapsed cycles	78
4-7. Close up view of the crack paths for Δa around the hole	79
4-8. The strategy used to convert the bi-axial stress data into cyclic stress data which was suitable for use in a fatigue crack growth model.....	82
5-1. Available discrete points available which can be fit using a surrogate model	86
5-2. Surrogate model fit to either a complete or partial crack growth history	88
5-3. Comparison of an exact function and the corresponding kriging surrogate model for an arbitrary set of five data points	90
5-4. Integration of fatigue crack growth model from N_i to N_{i+1} using either Euler or midpoint approximation	92
5-5. Errors used to adjust the adaptive integration step size algorithm.....	94
5-6. An inclined center crack in a square finite plate under uniaxial tension	103
5-7. Comparison of cycle number and integration step size or percent error for surrogate for $R = 0.1$ and $R = 0.5$ for aluminum 2024.....	104
6-1. Finite element mesh with enriched nodes	109
6-2. Edge crack in a finite plate geometry used to test quasi-static crack growth with the reanalysis algorithm	115
6-3. Normalized computational time for stiffness matrix assembly as well as factorization and solving of system of linear equations as a function of number of iterations.....	117
6-4. Normalized computational time for stiffness matrix assembly as well as factorization and solving of system of linear equations as a function of number of mesh density	117
6-5. Edge crack in a finite plate geometry used to test optimization with the reanalysis algorithm	118
6-6. Normalized computational time for stiffness matrix assembly as well as factorization and solving of system of linear equations as a function of number of iterations.....	119
7-1. Coordinate system (x,y,z) and directional names for an airplane	122
7-2. Example of a wing box with span s , chord length c which is a function of y , and normalized x -coordinate u	125

7-3. Wing box model in the coordinate system that was used for this analysis.....	125
7-4. Comparison of elliptical loading model for various wing taper ratios.....	126
7-5. Examples of the changing pressure distribution over an airfoil as a function of the angle of attack	128
7-6. Normalized chord-wise coordinates u with maximum pressure coordinate u_0 pressure distribution P	128
7-7. Comparison of the changes in the maximum pressure location u_0 and subsequently the resulting pressure profile for some angles of attack α	129
7-8. The total normalized distribution along the airplane wing for $\alpha = 5^\circ$	129
7-9. Comparison between the angle of attack and the lift coefficient	131
7-10. The direction of the uniform pressure distribution defined by the drag	132
7-11. The stress histories for the two-dimensional stress components for Flight ID 152	135
7-12. Equivalent stress and identified cycles from equivalent stress for Flight ID 152	137
7-13. The boundary conditions and applied bi-axial stresses for the analysis of a panel on an airplane wing box subjected to variable amplitude fatigue.....	139
7-14. The initial and final crack geometries from the stresses identified through the normalized flight data from the AFRL	140
7-15. Close-up view of the final crack geometry from the stresses identified through the normalized flight data from the AFRL	141
7-16. Comparison of the crack length as a function of the cycle number for the 19 flights from the normalized AFRL data.....	141
7-17. The Mode I and Mode II stress intensity factor ranges for the 37,007 cycles ...	142
8-1. Possible crack propagation paths between dissimilar materials	148
A-1. Representative geometry for a center crack in a finite plate.....	152
A-2. Representative geometry for an edge crack in a finite plate.....	153
A-3. Representative geometry for an inclined edge crack in a finite plate.....	155
A-4. Representative geometry for a hard inclusion in a finite plate	156
A-5. The σ_{xx} contours for a hard inclusion	157

A-6. The σ_{xy} contours for a hard inclusion	157
A-7. The σ_{yy} contours for a hard inclusion	157
A-8. Representative geometry for a void in an infinite plate.....	158
A-9. The σ_{xx} contours for a void in an infinite plate	159
A-10. The σ_{xy} contours for a void in an infinite plate	159
A-11. The σ_{yy} contours for a void in an infinite plate	159
A-12. Representative geometry for a crack initiating at an angle θ for a plate with a hole	160
A-13. Comparison of crack paths to those predicted by Bordas for a hard and soft inclusion	163
A-14. Comparison between Paris model and XFEM simulation for fatigue crack growth for a center crack in an infinite plate	164
D-1. Stress history for Flight ID 2	170
D-2. Stress history for Flight ID 8	170
D-3. Stress history for Flight ID 10	170
D-4. Stress history for Flight ID 12	171
D-5. Stress history for Flight ID 16	171
D-6. Stress history for Flight ID 18	171
D-7. Stress history for Flight ID 22	172
D-8. Stress history for Flight ID 26	172
D-9. Stress history for Flight ID 138	172
D-10. Stress history for Flight ID 140	173
D-11. Stress history for Flight ID 146	173
D-12. Stress history for Flight ID 148	173
D-13. Stress history for Flight ID 150	174
D-14. Stress history for Flight ID 152	174

D-15. Stress history for Flight ID 154	174
D-16. Stress history for Flight ID 156	175
D-17. Stress history for Flight ID 159	175
D-18. Stress history for Flight ID 161	175
D-19. Stress history for Flight ID 163	176

LIST OF ABBREVIATIONS

AFRL	Air Force Research Laboratory
AMD	Approximate Minimum Degree Algorithm
CTOD	Crack tip opening displacement
DOF	Degrees of freedom
EPFM	Elastic plastic fracture mechanics
FE	Function evaluations
FEM	Finite element method
GUI	Graphical user interface
LEFM	Linear elastic fracture mechanics
LSM	Level set method
MXFEM	MATLAB [®] XFEM Code
PUFEM	Partition of unity finite element method
XFEM	Extended finite element method

Abstract of Dissertation Presented to the Graduate School
of the University of Florida in Partial Fulfillment of the
Requirements for the Degree of Doctor of Philosophy

VARIABLE AMPLITUDE FATIGUE ANALYSIS USING SURROGATE MODELS AND
EXACT XFEM REANALYSIS

By

Matthew Jon Pais

December 2011

Chair: Nam-Ho Kim
Major: Mechanical Engineering

Fatigue crack growth occurs as the result of repeated cyclic loading well below the stress levels which typically would cause failure. The number of cycles to failure for high-cycle fatigue is commonly of the order of 10^4 - 10^8 cycles to failure. Fatigue is characterized by a differential equation which gives the crack growth rate as a function of material properties and the stress intensity factor. Analytical relationships for the stress intensity factor are limited to simple geometries. A numerical method is commonly used to find the stress intensity factor for a given geometry under certain loading.

The use of kriging to assist higher-order approximations is introduced. Here stress intensity factor data is fit using a surrogate. This surrogate is used to extrapolate for the purpose of integration, which enables larger step sizes to be taken without a loss in accuracy for the solution of the governing differential equation. Furthermore, it was observed that for the extended finite element method a small portion of the global stiffness matrix is changed as a result of crack growth. It is possible to use this small portion to save on both the assembly and solution of the resulting system of linear equations. This results in savings in both the assembly and factorization of the stiffness

matrix for repeated simulations reducing the computational cost associated with numerical fatigue crack growth.

The use of the XFEM reanalysis algorithm allow for the analysis of non-proportional mixed-mode variable amplitude loading upon an airplane wing to be considered. An airplane wing box was analyzed using Abaqus[®]. The Abaqus[®] stress solution was used in coordination with airplane flight data provided by the Air Force Research Laboratory. This stress history is converted into a cyclic loading history through the use of the rainflow counting method. The resulting analysis is one where approximately 30,000 cycles elapse. Due to the non-proportional loading, each cycle must be modeled independently as the direction of crack propagation will be cycle-dependent creating a solution which would be very expensive with existing techniques.

CHAPTER 1 INTRODUCTION

Motivation

The nucleation and propagation of cracks in engineered structures is an important consideration for the design of a structure. In particular fatigue fracture, caused by repeated cyclic loading well below the yield stress of a material can cause sudden, catastrophic failure. The relationship between the applied stress and the number of cycles to failure is typically given by a material specific σ - N curve as shown in Figure 1-1. For fatigue failure once a small crack has formed, the cyclic loadings cause the material ahead of the crack to slowly fail and the crack grows. Initially a crack grows very slowly, maybe on the order of nanometers at a given cycle. Over time the crack growth accelerates. Once the crack reaches a critical length a_c a large amount of crack growth occurs rapidly and without warning. There are many incidents caused by the growth of fatigue cracks, many of which resulted in the loss of human lives.

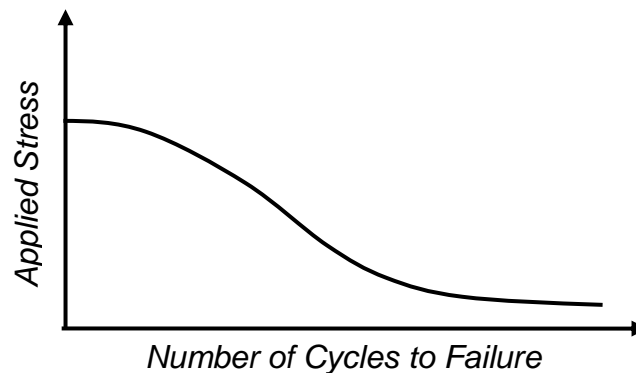


Figure 1-1. Representative S-N curve for a material subjected to cyclic loading. (Note that there is a point where if the applied stress is sufficiently small that the number of cycles to failure is infinite).

In 1952 the world's first jetliner the de Havilland Comet [1] was entered into service. In January and May of 1954 two of the Comets disintegrated during flights between New York and London. The failure was caused by fatigue cracks which

initiated near the front of the cabin on the roof. Over time the crack grew until it reached a window, causing sudden catastrophic failure. In 1957 the 7th President of the Philippines died [2] along with 24 others when fatigue caused a drive shaft to break, subsequently causing power failure aboard the airplane. In 1968 a helicopter [3] crashed in Compton, California due to fatigue failure of the blade spindle. Twenty one lives were lost.

In 1980 the Alexander L. Keilland [4] oil platform capsized killing 123 people. The main cause of the failure was determined to be a poor weld, reducing the fatigue strength of the structure. In 1985 Japan Flight 123 [5] from Tokyo to Osaka crashed in the deadliest plane crash in history. The incorrect repair of a prior incident where the tail of the airplane impacted the runway in 1978 eventually lead to fatigue failure. There were 4 survivors of the 524 people on the airplane. Fatigue cracks slowly grew until causing sudden rupture 7 years later. In 1988 an Aloha Airlines [6] flight between the Hawaiian islands of Hilo and Honolulu suffered extensive damage after an explosive decompression caused by the combined effects of a fatigue crack and corrosion. The plane safely landed in Maui with 94 survivors, 65 injuries and 1 death. In this case, the fracture was exacerbated by being in service well past it's design life (89,000 service hours instead of 75,000 design hours) as well as operating in a corrosive environment caused by exposure to high levels of humidity and salt. In 1989 a United Airlines flight [7] from Denver, Colorado to Chicago, Illinois crashed due to a maintenance crew failing to find a crack in a fan disk within the engine, 112 deaths occurred.

In 1992 a Boeing 747 [8] crashed in to the Bijlmermeer neighborhood in Amsterdam, Netherlands, killing 43. The plane crashed when fatigue failure did not

allow for the engine to cleanly separate from the wing as designed, leading to the accident. In 1998 an InterCityExpress train [9] crashed in Eschede, Germany caused by fatigue failure of the train wheels. Of the 287 passengers aboard, there were 101 deaths and 88 injuries. It is the deadliest train disaster in German history.

In 2002 China Airlines Flight 611 [10] broke apart during a flight killing all 225 people aboard the airplane. Similar to Japan Airlines Flight 123, an incorrect repair procedure allowed fatigue cracks to grow eventually causing failure. In 2005 metal fatigue caused a Chalk's Ocean Airways flight [11] from Fort Lauderdale, Florida to Bimini, Bahamas to crash in Miami Beach, FL after metal fatigue broke off the right wing. There were 20 casualties. In 2007 a Missouri Air National Guard F-15C Eagle [12] crashed due to a structural part not meeting specifications, leading to a series of fatigue cracks to develop and propagate. As recently as July 2009 a Southwest Airlines flight [13] from Nashville, Tennessee to Baltimore, Maryland had to make an emergency landing after a 'football sized' hole opened causing rapid decompression. Investigations are still undergoing. The series of accidents through history including those in the 1990s and 2000s show that there is still much work to be done to prevent fatigue failures from taking human lives.

Fatigue Crack Growth

Fatigue crack growth models are empirical models which are generally created by performing one or a series of experiments and fitting the resulting data to a function of the form [14]

$$\frac{da}{dN} = f(\Delta K) \quad 1-1$$

where da/dN is the crack growth rate and ΔK is the stress intensity factor ratio, which is a driving mechanism to crack growth. The stress intensity factor range ΔK can be calculated as

$$\Delta K = K_{\max} - K_{\min} \quad 1-2$$

where K_{\max} and K_{\min} are the stress intensity factors at the maximum and minimum applied stress during a given loading cycle. The stress intensity factor is used to describe the state of stress at the tip of a crack and depends upon, crack location, crack size, distribution and magnitude of loading, and specimen geometry. There are three modes of fracture [15] as shown in Figure 1-2. On the left is Mode I or opening mode. In the middle is the Mode II or in-plane shear mode. Finally, on the right is the Mode III or out-of-plane shear mode. In two-dimensions only Modes I and II is considered, while Mode III is also considered for three-dimensional problems. When multiple modes occur simultaneously, the underlying problem is commonly referred to as being mixed-mode. Mixed-mode fractures can be separated into the underlying Mode I, II, and III components through the use of methods such as the domain form of the contour integral [16-19].

For some simplified cases analytical expressions for the stress intensity factors are available [20], but for a more general case a numerical method such as the finite element method may be used to find the stress intensity factor. Specifically, the use of a method such as the crack tip opening displacement (CTOD) [15], J-integral [17] or the domain form of the contour integral [18, 19] may be used to extract the mixed-mode stress intensity factors from a finite element solution. Note that Eq. 1-1 does not provide the crack size directly. Rather, it provides the rate of crack growth at a given range of

stress intensity factor, which also depends on the current crack size. Thus, a numerical integration method should be employed to predict the crack growth by integrating the given fatigue model. In addition, the crack in a complex geometry may not grow in a single direction. The direction of future growth is often considered to be governed by the maximum circumferential stress criterion in the finite element framework as closed form solutions for the direction of crack growth are available [21].

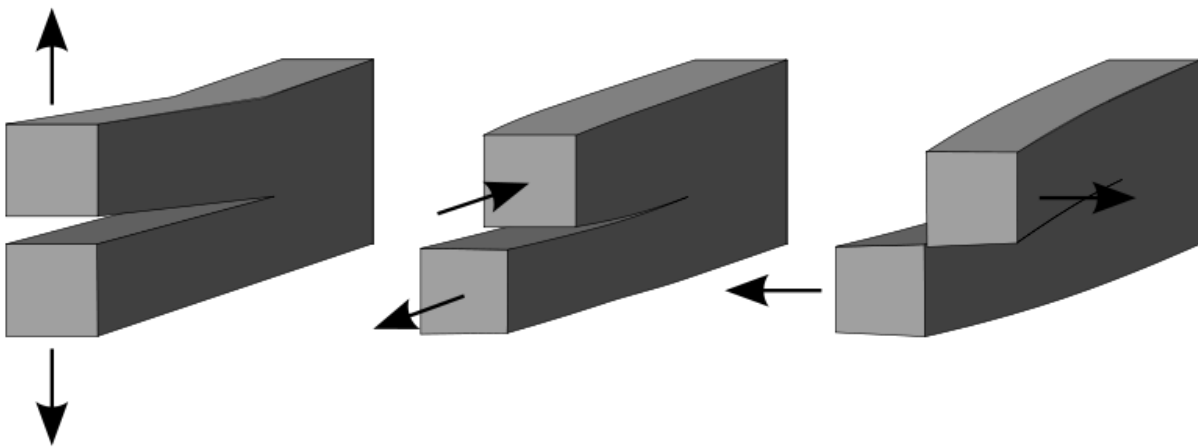


Figure 1-2. Representation of the Mode I, Mode II, and Mode III opening mechanisms.

There are two main opinions on how to attempt to approximate the solution of the governing differential equation in Eq. 1-1 for constant amplitude loading such as that shown in Figure 1-3: controlling cycles or crack increment. The first model assumes that a fixed number of cycles ΔN is chosen prior to starting the simulations [22]. Thus, Δa is variable, being initially small and increasing with the iteration number. At each crack growth iteration, ΔK is evaluated from an analytical formula or numerical simulation, which is then used to approximate the solution of the ordinary differential equation governing fatigue crack growth. Since the expression of ΔK is unknown as a function of crack size, the differential equation cannot be exactly integrated using any numerical integration technique. Instead, there are only values of ΔK at the current and all past

simulation iterations available for use during the integration. An explicit numerical integration method such as the forward Euler method [23] can be used to approximate the current growth increment Δa . The use of a higher-order integration method such as the midpoint [23] or Runge-Kutta [23] methods require additional approximations for the crack sizes which require the corresponding ΔK function evaluations. Furthermore, the required function evaluations may have no physical meaning, especially considering that crack growth does not occur at all instances within a loading cycle [24]. The forward Euler method requires small time steps to be accurate; otherwise crack growth will be under predicted. As the crack increment is based on ΔK , it is essential for the mesh to be sufficiently refined around the crack tip such that ΔK has converged and an accurate representation of the localized state of stress around the crack tip.

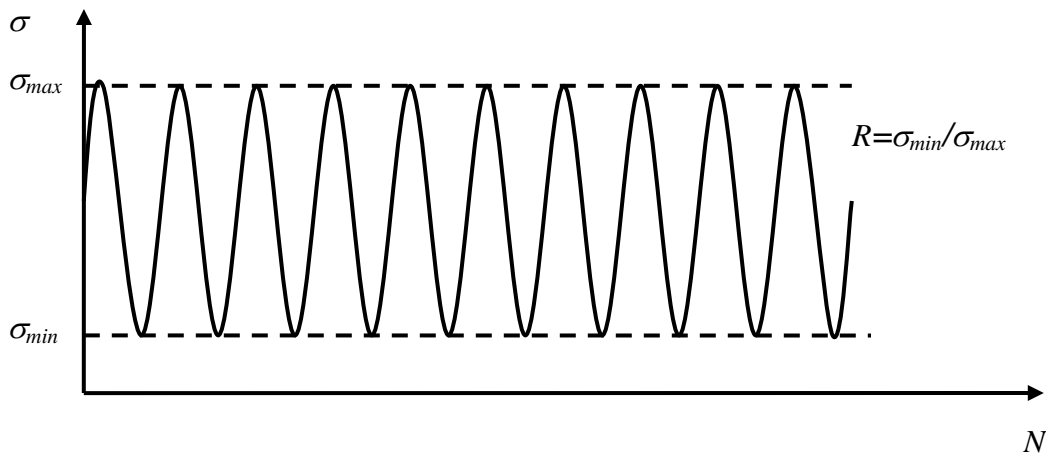


Figure 1-3. An example of constant amplitude loading with characteristic parameters such as the maximum and minimum applied stresses and the stress ratio R .

The other solution procedure assumes a fixed size of crack increment [25] at each simulation iteration. Therefore, the number of elapsed cycles is initially large and decreases with the iteration number. Here, the challenge is accurately back-calculating the number of elapsed cycles from the fixed crack growth data. The forward Euler

method is commonly applied to the back-calculation of the number of elapsed cycles [26], but as with the approach of fixing ΔN there must be care taken in selecting a sufficiently small value of ΔN for the forward Euler method to maintain accuracy. A higher-order approximation could be applied here as well, but discrete values of ΔK are not available for all data points required for the evaluation of the slope of the $a-N$ curve for these higher-order methods. These values require additional function evaluations.

For a constant amplitude loading simulation involving mixed-mode crack growth, it is also imperative that the choice of fixed Δa or ΔN be made with care. The path that the crack may take is also influenced by the choice of Δa or ΔN as having too large of a value of either can result in deviation from the crack growth path that would be predicted with the use of smaller growth increments. Once this deviation occurs the path of future crack growth is definitely affected, but this deviation is not clear to a user unless a convergence study with respect to crack path is performed. In the literature [22, 25], it is clear that the chosen fixed crack increments influence the crack path under mixed-mode loading.

For the case of variable amplitude fatigue where the applied loading does not have a constant amplitude, it may not be possible to choose an incremental Δa or ΔN and have an accurate solution to the governing differential equation given by Eq. 1-1. As the magnitudes of the applied stress are changing with each cycle, the crack path is changing on a cycle by cycle basis. Attempting to model this behavior considering multiple loading cycles at a time would assume a constant crack growth direction for many loading cycles and fail to capture the changes in the crack path based on the changes in the applied stress profile.

During each loading cycle, plasticity forms around the crack tip due to the stress concentration that the crack introduces into a material. There are many models for the size of this plastic zone [14, 15, 27]. The main challenge associated with modeling variable amplitude fatigue is with the interaction of overloads and underloads [14, 24, 27-30] and the associated changes in the plastic zone size. An overload can be considered to be a peak load which is an uncharacteristically large magnitude, while an underload is a valley load with an uncharacteristically small magnitude as shown in Figure 1-4.

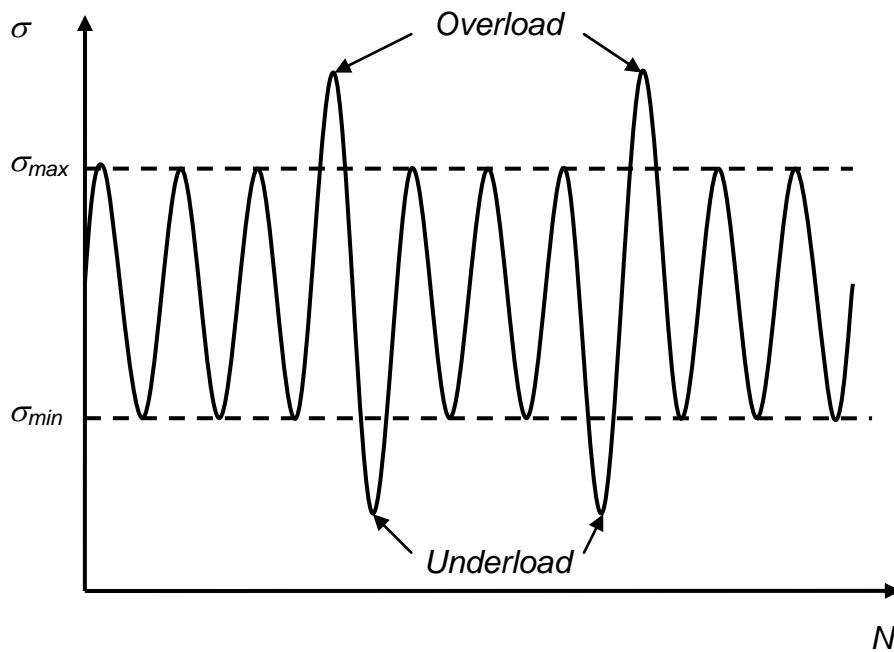


Figure 1-4. An example of an overload followed by an underload and an underload followed by an overload.

The effect of an overload is an increase in the crack tip plasticity compared to that which would come from the constant amplitude loading portion of Figure 1-4. This increase in plasticity acts to retard future crack growth. Similarly, an underload results in a reduced amount of plasticity compared to the constant amplitude loading portion of the cyclic loading curve. The two cases shown in Figure 1-4, an overload followed by an

underload and an underload followed by an overload result in different crack growth paths and must be considered for an accurate analysis of variable amplitude fatigue. Attempts to capture the behavior associated with the interaction between overload and underloads has been explored through the use of empirical models such as crack growth models [14, 27, 31-34], the small time scale model [24], the state-space model [29, 30] in addition to elastic plastic fracture mechanics (EPFM) analysis in the FEM [35, 36] as well as the extended finite element method (XFEM) [37, 38].

Computational Fracture Mechanics

With the ever increasing speed of computers, numerical methods such as the finite element method (FEM) are able to model problems with increasing fidelity and increasing complexity, but finite element modeling of fatigue crack growth is still a challenging computational fracture mechanics problem. As the finite element mesh must conform to the geometry, the mesh around the crack tip must be recreated [25] whenever growth occurs. Even if a concept such as crack-blocks [39] is used where a small region around a crack tip is remeshed at each iteration, the computational demands of the remeshing can contribute significantly to the simulations especially if a large number of iterations of crack growth are to be modeled. In addition to the localized mesh reconstruction around the crack tip, care needs to be taken to ensure accuracy in the crack path, displacement, and stress intensity factors with FEM.

It is possible to model crack growth based on the cohesive zone model in the classical FEM framework [40]. The cohesive zone model assumes that crack growth can be represented as a traction-separation model as shown in Figure 1-5. Special cohesive zone elements can then be used which allow for crack growth without the need to remesh. However, some knowledge about the crack path is needed *a priori* in

order to define which elements in the mesh will be cohesive elements instead of traditional methods. The model is based on the assumption that once the yield stress σ_Y is reached, the material properties start to degrade until some critical separation distance $\bar{\delta}_c$ is reached. At this point the given element/interface in the finite element model can no longer sustain loading and fracture occurs.

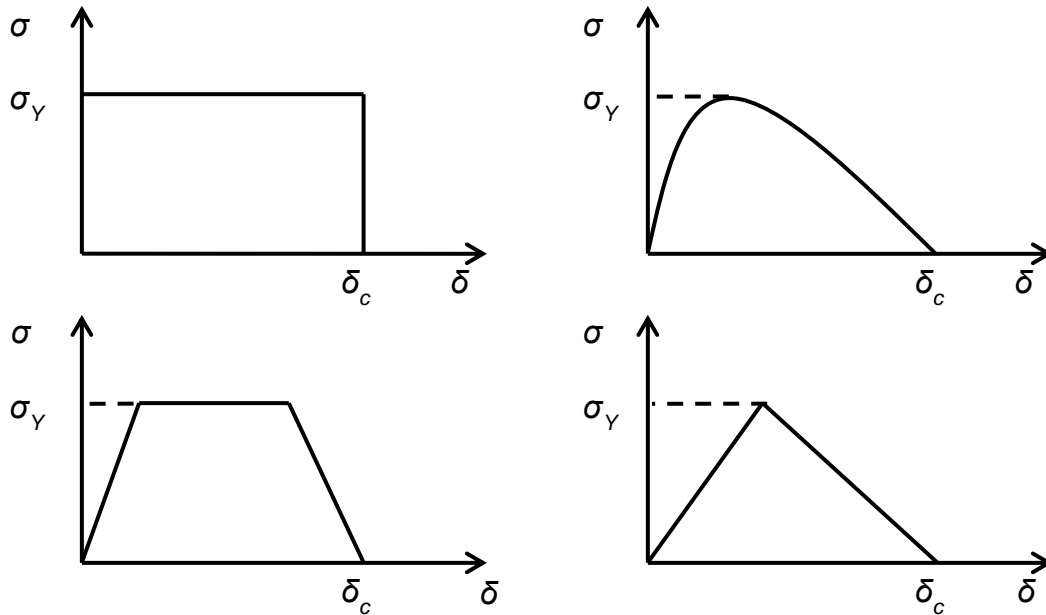


Figure 1-5. Examples of possible traction-separation models that can be used as part of a cohesive zone model where σ_Y is the yield stress and $\bar{\delta}_c$ is the critical separation.

The main challenge in cohesive zone models is to create an accurate model for the given traction-separation relationship for a given material system including the shape of the traction-separation model and the critical separation distance [40-42]. It is often the case that the parameters of the traction-separation model for a given material change according to the length scale in the model and corresponding experimental tests. In practice, it can be the case that small changes to the parameters in the traction-separation model result in substantial differences in the resulting finite element solution [40]. Moody [41] introduced a series of experiments which can be used to

determine the traction-separation relationship. Scheider [42] explored the use of finite element simulations to determine the traction-separation relationship. The shape of the softening function that will be used to degrade the material properties is also of much importance [40].

The XFEM [25] alleviates the challenges associated with the mesh conforming to the geometry by allowing discontinuities or other localized phenomena to be represented independent of the finite element mesh. Enrichment functions based on linear elastic fracture mechanics (LEFM) are available which are independent of material, unlike cohesive zone models, which are material and possible length-scale dependent. Additional functions, referred to as enrichment functions, are introduced into the displacement approximation through the property of the partition of unity [43]. Additional nodal degrees-of-freedom are also introduced that act to 'calibrate' the enrichment functions as well as are used for interpolating within an element and in the calculation of stresses or stress intensity factors using a method such as the domain form of the contour integrals. While there is no need to worry about mesh construction or the need to create a traction-separation relationship, the XFEM still requires the convergence of the crack path, displacement, and stress intensity factors for accurate crack modeling.

Scope

The goals and scope of this work are focused on accurate modeling of fatigue crack growth under constant and variable amplitude loading for complex geometries with unknown $\Delta K - a$ relationships with computational efficiency and high accuracy. In particular the following topics are addressed:

Increasing the allowable step size for a given fixed increment of Δa or ΔN without a loss in accuracy when approximating the solution to the governing ordinary differential equation for constant amplitude loading. The influence that this increased step size has on the convergence of the crack path is also considered. A surrogate model is exploited to enable the use of higher-order approximations to the calculation of magnitude and direction of crack growth with a single expensive function evaluation. A variable step size algorithm is also introduced to better allocate the available computational resources based on the accuracy of the surrogate model when extrapolating.

The fundamental formulation of the XFEM is exploited to enable the modeling of quasi-static crack growth with reduced computational time through an exact reanalysis algorithm. When crack growth occurs, the changes to the global stiffness matrix are limited to a localized number of elements about the crack tip. Here, a supernodal Cholesky factorization is used to exploit these properties. During the first XFEM simulation, the full stiffness matrix is formed and a Cholesky factorization is performed. In all subsequent iterations this Cholesky factorization is directly modified to account for the changes to in the stiffness matrix caused by crack growth. Computational savings are realized for both the assembly and factorization of the global stiffness matrix. This reanalysis algorithm is also employed as a means to consider optimization problems in the XFEM framework where the location of a discontinuity is iteration dependent.

Multi-axial variable amplitude fatigue analysis is performed for the case where the stress components are non-proportional. In this problem, traditional approaches based upon Δa or ΔN fail as the crack growth direction becomes cycle dependent. As the crack path is unknown, the likelihood of having an analytical equation available for the stress

intensity factors as a function of crack size is small. Due to the variable amplitude loading, the changing plasticity at the crack tip caused by the varying maximum and minimum applied loads affects the crack growth rate. A test problem of an airplane wing panel subjected to biaxial stresses during 19 flights based upon normalized flight data from the Air Force Research Laboratory (AFRL) is considered. A method to scale and convert the normalized data into equivalent biaxial loading cycles is given.

Outline

Chapter 2 introduces the level set method for tracking closed and open sections. This method is used to track the location of discontinuities in the XFEM as they do not conform to the mesh. This includes cracks, inclusions and voids. Chapter 3 introduces the extended finite element method. First the general form is considered. Then enrichment functions are introduced for cracks, inclusions and voids. A discussion of the commercial and open-source implementations of XFEM is presented. Chapter 4 details the domain form of the contour integral for the extraction of mixed-mode stress intensity factors from a XFEM analysis of a cracked body. Criteria which determine the direction of crack growth are introduced. Finally, fatigue crack growth models predicting the magnitude of crack growth are given and limitations associated with these models are discussed. In addition, rainflow counting methods are introduced for the purposes of converting stress histories into equivalent stress cycles. Chapter 5 introduces the use of a surrogate model for increased accuracy in the integration of the ordinary differential equation governing fatigue crack growth allowing larger step sizes to be considered without loss of accuracy for the case of constant amplitude loading. A surrogate model may also be used to enable higher-order approximations to the crack growth direction. An algorithm is also presented where the step size dynamically changes based on the

surrogate accuracy in order to minimize the number of finite element simulations needed. Chapter 6 introduces and details the use of a reanalysis algorithm to make the repeated simulations of crack growth in a quasi-static environment affordable, allowing for additional simulations in a fixed amount of time. The sparse Cholesky factorization is detailed as well as the algorithms which can be used to modify an existing sparse Cholesky factorization. The proposed reanalysis algorithm leads to reduced computational cost for repeated XFEM simulations. Chapter 7 details the variable amplitude fatigue analysis procedure including the calculation of stress histories from aircraft flight data, the conversion of these stress histories into cyclic loads which are used in fatigue model prediction, and the prediction of crack growth under variable amplitude loading using surrogate models and an exact XFEM reanalysis algorithm. Chapter 8 summarizes the research as well as suggesting possible areas of future work.

CHAPTER 2 THE LEVEL SET METHOD

Level Set Method for Closed Sections

The level set method was introduced by Sethian and Osher [44] as a numerical method which can be used to track the evolution of interfaces and shapes. The method is based on evolving an interface subjected to a front velocity given by the physics of the underlying problem which is being modeled. Level set methods have been used in a wide range of engineering applications in topics such as compressible [45] and incompressible [46] flow, computer vision [47], image processing [48], manufacturing [49-51] and structural optimization [52, 53]. While the figures given in this chapter are two-dimensional, the principles can also applied to three-dimensional problems [54, 55].

The level set method is used to discretize the domain of interest into discrete points. Each of these points is assigned a signed distance value from that point to the nearest intersection with the interface denoted Γ . A continuous level set function $\phi(\mathbf{x})$ is introduced where \mathbf{x} is a point in the domain of interest Ω . The level set function can be characterized as a function of the domain and with a time component as

$$\begin{aligned}\phi(\mathbf{x}, t) < 0 & \quad \text{for } \mathbf{x} \in \Omega \\ \phi(\mathbf{x}, t) > 0 & \quad \text{for } \mathbf{x} \notin \Omega . \\ \phi(\mathbf{x}, t) = 0 & \quad \text{for } \mathbf{x} \in \Gamma\end{aligned}\tag{2-1}$$

Thus, points inside the domain of interest are given negative signs, points outside of the domain of interest are given positive signs, and points on the interface have no sign as their signed distance is zero. An example of the signed distance function for a circular domain is given in Figure 2-1. From Eq. 2-1 it can be noted that at any time t the location of the interface can be found as the locations where

$$\phi(\mathbf{x}, t) = 0 \quad 2-2$$

and is commonly referred to as the zero level set of ϕ .

The evolution of the level set function is usually assumed to follow the Hamilton-Jacobi equation [44] where the evolution can be predicted as

$$\frac{\partial \phi}{\partial t} = v |\nabla \phi| \quad 2-3$$

where v is the front velocity and $\nabla \phi$ is the spatial gradient of the level set function. The solution of Eq. 2-3 is usually approximated using finite differencing techniques [23] which provide sufficient solution accuracy when the time step is small. When the forward finite difference technique is considered, the derivative of ϕ with respect to time can be approximated as

$$\frac{\phi_{i+1} - \phi_i}{\Delta t} + \mathbf{V}_i \cdot \nabla \phi_i = 0 \quad 2-4$$

where ϕ_{i+1} is the updated level set value, ϕ_i is the current level set value, \mathbf{V}_i is the front velocity vector, and Δt is the elapsed time between i and $i+1$. Equation 2-4 can be rewritten in a more convenient form in two-dimensions as

$$\phi_{i+1} = \phi_i - \Delta t \left(u_i \frac{\partial \phi_i}{\partial x} + v_i \frac{\partial \phi_i}{\partial y} \right) \quad 2-5$$

where u_i is the front velocity in the x-direction and v_i is the front velocity in the y-direction. In Eqs. 2-4 and 2-5 the time step Δt is limited by the Courant-Friedrichs-Lewy (CFL) condition [56] which ensures that the approximation to the solution of the partial differential equation converges. The CFL condition is given as

$$\Delta t < \frac{\max(\Delta x, \Delta y)}{\max(u, v)} \quad 2-6$$

where Δx and Δy are the grid spacing in the x and y-directions. In practice, the level set function needs to only be defined in a narrow band [57-59] around the interfaces of interest or can be represented using the fast marching method [60], a variant of the level set method with improved computational efficiency.

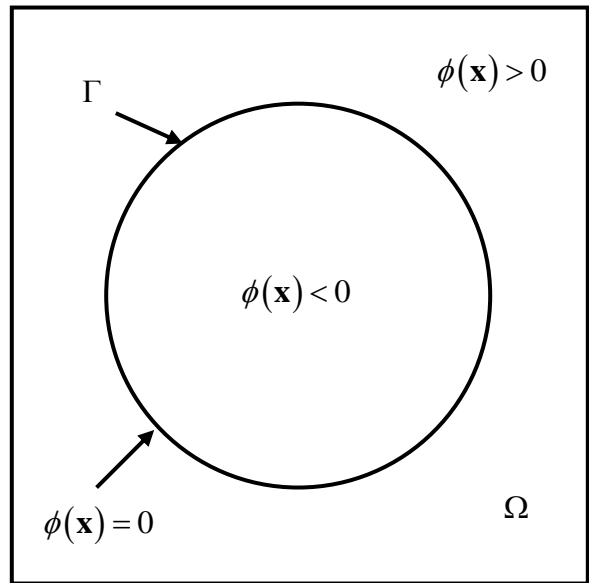


Figure 2-1. Example of a signed distance function for a closed domain.

Level Set Method for Open Sections

The version of the level set method presented in the previous section is only valid for a closed section. For an open section, the definition of the interior, exterior, and interface as defined in Eq. 2-1 no longer have a physical meaning. Stolarska [57] introduced a modified version of the level set method which allows for open sections to be tracked with the use of multiple level set functions. An open section as shown in Figure 2-2 can be described by two level sets $\phi(\mathbf{x})$ and $\psi(\mathbf{x})$. The interface of interest is given as the intersection of $\phi(\mathbf{x})$ and $\psi(\mathbf{x})$ where

$$\phi(\mathbf{x}) < 0 \text{ and } \psi(\mathbf{x}) = 0. \quad 2-7$$

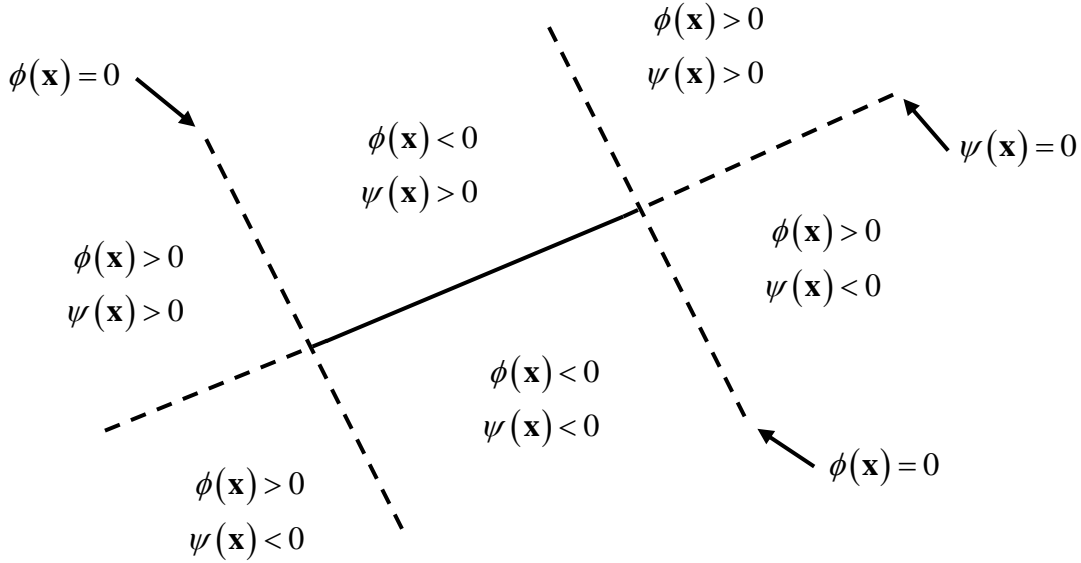


Figure 2-2. Example of the signed distance functions for an open section. (Note: the interface of interest is given as the region where phi is negative and psi is equal to zero).

An updating algorithm for these two coupled level set function is also given by Stolarska [57]. For the case of the $\phi(\mathbf{x})$ level set function, the update is identical to that presented in Eqs. 2-3 - 2-5. Two regions are defined with respect to the $\psi(\mathbf{x})$ level set function, $\Omega^{\text{update}} = \phi(\mathbf{x}) > 0$ and $\Omega^{\text{no update}} \leq 0$ which correspond to the regions which will and will not be updated. The level set function $\psi(\mathbf{x})$ is updated in two-dimensions according to

$$\begin{aligned} \psi_i^{n+1} &= \psi_i^n && \text{in } \Omega^{\text{no update}} \\ \psi_i^{n+1} &= \pm \left| (x - x_i) \frac{F_y}{\|F\|} - (y - y_i) \frac{F_x}{\|F\|} \right| && \text{in } \Omega^{\text{update}} \end{aligned} \quad 2-8$$

where the crack tip displacement vector is given as $\mathbf{F} = (F_x, F_y)$ and the current crack tip is given by the coordinates (x_i, y_i) . The sign of the updated value ψ_i^{n+1} is chosen to correspond to the location of that node with respect to Figure 2-2.

Summary

The level set method allows for a closed or open section to be tracked by defining signed distance values at discrete points in the domain of interest. The value of the level set function at these points is then updated based on the front velocity at each point in the domain using a finite difference technique to approximate the solution to the governing partial differential equation. The CFL condition is used to ensure that the solution of the differential equation converges. The level set method seems to be ideal for use in a finite element environment where the nodes of the finite element mesh could be used as the fixed points in the level set algorithm. The finite element shape functions could be used to interpolate within an element to identify the values of the level set function if this would be of interest.

CHAPTER 3
THE EXTENDED FINITE ELEMENT METHOD

General Form of the Extended Finite Element Method

The extended finite element method (XFEM) allows for discontinuities to be represented independent of the finite element mesh by exploiting the partition of unity finite element method [43] (PUFEM). In this method additional functions, commonly referred to as enrichment functions, can be added to the displacement approximation as long as the partition of unity is satisfied, i.e. $\sum N_I(\mathbf{x})=1$ for all \mathbf{x} where $N_I(\mathbf{x})$ are the finite element shape functions. The XFEM uses these enrichment functions as a tool to represent a non-smooth behavior of field variables, such as stress across the interface of dissimilar materials or displacement across cracks. In general, the enrichment functions introduced into the displacement approximation are only defined over a small number of elements relative to the total size of the domain. Additional degrees of freedom are introduced in all elements where the discontinuity is present, and depending upon the type of function chosen, possibly some neighboring elements which are known as blending elements.

The additional functions used in the displacement approximation are commonly called enrichment functions and the approximation takes the form:

$$\mathbf{u}^h(\mathbf{x}) = \sum_I N_I(\mathbf{x}) \left[\mathbf{u}_I + \sum_J v^J(\mathbf{x}) \mathbf{a}_I^J \right] \quad 3-1$$

where \mathbf{u}_I are the classical finite element degrees of freedom (DOF), $v^J(\mathbf{x})$ is the J th enrichment function at the I th node, and \mathbf{a}_I^J are the enriched DOF corresponding to the J th enrichment function at the I th node. The enriched degrees of freedom introduced by Eq. 3-1 generally do not have a physical meaning and instead can be considered as a

calibration of the enrichment functions which result in the correct displacement approximation. Note that Eq. 3-1 does not satisfy the interpolation property, $\mathbf{u}_I = \mathbf{u}^h(\mathbf{x}_I)$, due to the enriched DOF, instead additional calculations are required in order to calculate the physical displacement using Eq. 3-1. The interpolation property is important in practice in applying boundary or contact conditions. Therefore, it is common practice to shift [61] the enrichment function such that

$$\Upsilon_I^J(\mathbf{x}) = \nu^J(\mathbf{x}) - \nu_I^J(\mathbf{x}) \quad 3-2$$

where $\nu_I^J(\mathbf{x})$ is the value of the J th enrichment function at the I th node. As the shifted enrichment function now takes a value of zero at all nodes, the solution of the resulting system of equations satisfies $\mathbf{u}_I = \mathbf{u}^h(\mathbf{x}_I)$ and the enriched DOF can be used for additional actions such as interpolation and post-processing operations. Here, the shifted enrichment functions are referred to with upper case characters, and the unshifted enrichment functions are referred to with lower case characters. The shifted displacement approximation is given by

$$\mathbf{u}^h(\mathbf{x}) = \sum_I N_I(\mathbf{x}) \left[\mathbf{u}_I + \sum_J \Upsilon_I^J(\mathbf{x}) \mathbf{a}_I^J \right] \quad 3-3$$

where $\Upsilon_I^J(\mathbf{x})$ is the J th shifted enrichment function at the I th node. Hereafter, $N_I(\mathbf{x})$ and $\Upsilon_I^J(\mathbf{x})$ will be written as N_I and Υ_I^J .

The Bubnov-Galerkin method [62] may be used to convert the displacement approximation given by Eq. 3-3 into a system of linear equations of form

$$\mathbf{Kq} = \mathbf{f} \quad 3-4$$

where \mathbf{K} is the global stiffness matrix, \mathbf{q} are the nodal DOF, and \mathbf{f} are the applied nodal forces. By appropriately ordering degrees of freedom, the global stiffness matrix \mathbf{K} can be considered as

$$\mathbf{K} = \begin{bmatrix} \mathbf{K}_{uu} & \mathbf{K}_{ua} \\ \mathbf{K}_{ua}^T & \mathbf{K}_{aa} \end{bmatrix} \quad 3-5$$

where \mathbf{K}_{uu} is the classical finite element stiffness matrix, \mathbf{K}_{aa} is the enriched finite element stiffness matrix, and \mathbf{K}_{ua} is a coupling matrix between the classical and enriched stiffness components. The elemental stiffness matrix \mathbf{K}_e for any member of \mathbf{K} may be calculated as

$$\mathbf{K}_e = \int_{\Omega^h} \mathbf{B}_\alpha^T \mathbf{C} \mathbf{B}_\beta d\Omega \quad \alpha, \beta = u, a \quad 3-6$$

where \mathbf{C} is the constitutive matrix for an isotropic linear elastic material, \mathbf{B}_u is the matrix of classical shape function derivatives, and \mathbf{B}_a is the matrix of enriched shape function derivatives. The general form of \mathbf{B}_u and \mathbf{B}_a is given by

$$\mathbf{B}_u = \begin{bmatrix} N_{I,x} & 0 & 0 \\ 0 & N_{I,y} & 0 \\ 0 & 0 & N_{I,z} \\ 0 & N_{I,z} & N_{I,y} \\ N_{I,z} & 0 & N_{I,x} \\ N_{I,y} & N_{I,x} & 0 \end{bmatrix}; \quad \mathbf{B}_a = \begin{bmatrix} (N_I \Upsilon_I^J)_{,x} & 0 & 0 \\ 0 & (N_I \Upsilon_I^J)_{,y} & 0 \\ 0 & 0 & (N_I \Upsilon_I^J)_{,z} \\ 0 & (N_I \Upsilon_I^J)_{,z} & (N_I \Upsilon_I^J)_{,y} \\ (N_I \Upsilon_I^J)_{,z} & 0 & (N_I \Upsilon_I^J)_{,x} \\ (N_I \Upsilon_I^J)_{,y} & (N_I \Upsilon_I^J)_{,x} & 0 \end{bmatrix} \quad 3-7$$

where $N_{I,i}$ is the derivative of $N_I(\mathbf{x})$ with respect to x_i and $(N_I \Upsilon_I^J)_{,i}$ is the derivative of

$N_I(\mathbf{x}) \Upsilon_I^J(\mathbf{x})$ with respect to x_i . In practice, $(N_I \Upsilon_I^J)_{,i}$ is calculated with the product rule:

$$\frac{\partial(N_I(\mathbf{x})\Upsilon_I^J(\mathbf{x}))}{\partial x_i} = \frac{\partial(N_I(\mathbf{x}))}{\partial x_i}\Upsilon_I^J(\mathbf{x}) + N_I(\mathbf{x})\frac{\partial(\Upsilon_I^J(\mathbf{x}))}{\partial x_i}. \quad 3-8$$

Similarly, \mathbf{q} and \mathbf{f} in Eq. 3-4 are given by

$$\mathbf{q}^T = \{\mathbf{u} \quad \mathbf{a}\}^T \quad 3-9$$

where \mathbf{u} and \mathbf{a} are vectors of the classical and enriched degrees of freedom and

$$\mathbf{f}^T = \{\mathbf{f}_u^T \quad \mathbf{f}_a^T\} \quad 3-10$$

where \mathbf{f}_u and \mathbf{f}_a are vectors of the applied forces for the classical and enriched components of the displacement approximation. The vectors \mathbf{f}_u and \mathbf{f}_a are given in terms of applied tractions $\bar{\mathbf{t}}$ and body forces $\bar{\mathbf{b}}$ as

$$\mathbf{f}_u = \int_{\Gamma_i^h} N_I \bar{\mathbf{t}} d\Gamma + \int_{\Omega^h} N_I \bar{\mathbf{b}} d\Omega \quad 3-11$$

and

$$\mathbf{f}_a = \int_{\Gamma_i^h} N_I \Upsilon_I^J \bar{\mathbf{t}} d\Gamma + \int_{\Omega^h} N_I \Upsilon_I^J \bar{\mathbf{b}} d\Omega. \quad 3-12$$

Stress and strain must be calculated with the use of the enrichment functions and enriched degrees of freedom such that the effect of the discontinuity within a particular element is considered. Therefore the strain and stress may be calculated as

$$\boldsymbol{\varepsilon} = [\mathbf{B}_u \quad \mathbf{B}_a] \{\mathbf{u} \quad \mathbf{a}\}^T \quad 3-13$$

and

$$\boldsymbol{\sigma} = \mathbf{C}\boldsymbol{\varepsilon}. \quad 3-14$$

Enrichment Functions

The XFEM has been used to solve a wide range of problems involving discontinuities. In general, discontinuities can be described as either strong or weak. A

strong discontinuity can be considered one where both the displacement and strain are discontinuous, while a weak discontinuity has a continuous displacement but a discontinuous strain. There exist enrichment functions for a variety of problems in areas including cracks, dislocation, grain boundaries, and phase interfaces [63-66]. Aquino [67] has also studied the use of proper orthogonal decomposition to incorporate experimental data into the displacement approximation for cases with no logical choice of enrichment function. Fries [68] introduced the use of hanging nodes in the XFEM framework with respect to inclusions, cracks, and fluid mechanics to allow for automated mesh refinement around discontinuities.

Crack Enrichment Functions

The modeling of cracks in the XFEM has been thoroughly explored [63-66, 69, 70]. Belytschko [71] was the first to study cracks in the XFEM framework based on the element-free Galerkin crack enrichment of Fleming [72]. Moës [25] introduced the use of the Heaviside enrichment function to simplify the representation of the crack away from the tip. Work has been done in two [25, 57, 71, 73, 74] and three-dimensions [54, 58-60, 75] for linear elastic [25, 54, 57-60, 71, 73-75], elastic-plastic [37, 76], and dynamic [77-81] fracture.

The common practice is to incorporate two enrichment functions into the XFEM displacement approximation to represent a crack. A Heaviside step function [25] is used to represent the crack away from the tip and a more complex set of functions is used to represent the crack tip asymptotic displacement field. The Heaviside step function is given as

$$h(\mathbf{x}) = \begin{cases} 1, & \text{above crack} \\ -1, & \text{below crack} \end{cases} \quad 3-15$$

It can be noticed that the enrichment given by Eq. 3-15 introduces a discontinuity in displacement across the crack. For a linear elastic crack tip, four enrichment functions [72] are used to incorporate the crack tip displacement field into elements containing the crack tip:

$$\phi_{\alpha}(\mathbf{x})_{,\alpha=1-4} = \sqrt{r} \left[\sin \frac{\theta}{2}, \cos \frac{\theta}{2}, \sin \theta \sin \frac{\theta}{2}, \sin \theta \cos \frac{\theta}{2} \right] \quad 3-16$$

where r and θ are the polar coordinates in the local crack tip coordinate system the origin is at the crack tip and $\theta = 0$ is parallel to the crack. Note that the first enrichment function in Eq. 3-16 is discontinuous across the crack behind the tip in the element containing the crack tip, acting as the Heaviside enrichment does. Should a node be enriched by both Eqs. 3-15 and 3-16, only Eq. 3-16 is used as shown in Figure 3-1 where the Heaviside and crack tip nodes are denoted by filled circles and squares.

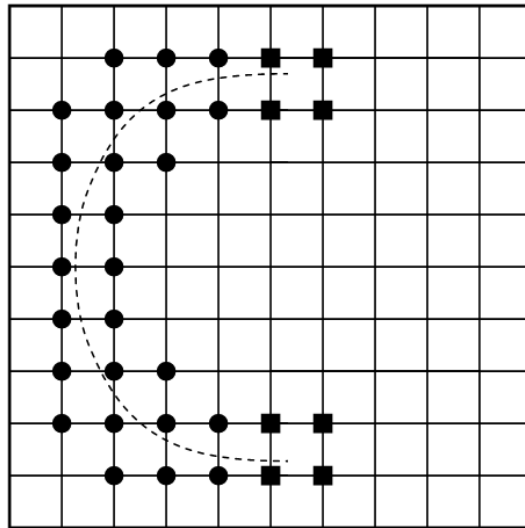


Figure 3-1. The nodes enriched with the Heaviside and crack tip enrichment functions.

Elgeudj [37, 38] identified crack tip enrichment functions [37] which can be used to capture the elastic plastic fracture behavior of the Hutchinson-Rice-Rosengren (HRR) singularity [82, 83]. The HRR singularity is a model for confined plasticity in the fatigue

of power-law hardening materials. From a Fourier analysis three basis functions were identified, and the basis with the lowest rank was chosen as the XFEM enrichment function. These basis functions are given by

$$\phi_{\alpha}(\mathbf{x})_{,\alpha=1-6} = r^{1/(n+1)} \left[\sin \frac{\theta}{2}, \cos \frac{\theta}{2}, \sin \frac{\theta}{2} \sin \theta, \cos \frac{\theta}{2} \sin \theta, \sin \frac{\theta}{2} \sin 3\theta, \cos \frac{\theta}{2} \sin 3\theta \right] \quad 3-17$$

where n is the power-law hardening exponent for the given material. Comparison between the enrichment functions of Eq. 3-16 and Eq. 3-17 showed very similar predictions in stress intensity factors between the elastic and elastic-plastic case for several values of n . These crack tip enrichment functions were then implemented to model elastic-plastic fatigue crack growth [38] for a material subjected to a combination of overload and underload conditions with a very limited number of loading cycles. The goal of this work was the capture the underlying plasticity evolution caused by the interaction of overload and underloads. In benchmark problems the stress intensity factor results do not show a significantly different prediction in stress intensity factor over the traditional crack tip enrichment method, but require significantly more computational resources for a given analysis. The similarity between the elastic plastic and linear elastic cases is likely due to the confined plasticity about the crack tip during fatigue crack growth. This was also observed by Anderson in the classical FEM [84].

Alternative crack tip conditions have also been explored such as bi-material cracks [85], cohesive cracks [86-88], branching cracks [89], cracks under frictional contact [38, 90], fretting fatigue cracks [91], interfacial cracks [76, 85, 92, 93], cracks in orthotropic materials [94], and cracks in piezoelectric materials [95]. Mousavi [96] introduced a unified framework for the enrichment of homogeneous, intersecting, and branching cracks through the use of harmonic enrichment functions. The XFEM has also been

used to study a variety of problems involving cracks including: the effect of cracks in plates [97, 98], crack detection and identification [99-101], shape optimization [26], and optimization with changing crack location using a reanalysis technique [22].

Because the XFEM mesh does not need to conform to the domain, a method must be used to track of the location of the cracks. To this end the use of the open segment level set method introduced by Stolarska [57] and detailed in Chapter 3 is used. Two level set functions are used to track the crack, the zero level set of $\psi(\mathbf{x})$ represents the crack body, while the zero level sets of $\phi(\mathbf{x})$, which is orthogonal to the zero level set of $\psi(\mathbf{x})$, represents the location of the crack tips. The two enrichment functions given in Eqs. 3-15 and 3-16 can be calculated in terms of $\phi(\mathbf{x})$ and $\psi(\mathbf{x})$ such that

$$h(\mathbf{x}) = h(\psi(\mathbf{x})) = \begin{cases} 1 & \text{for } \psi(\mathbf{x}) > 0 \\ -1 & \text{for } \psi(\mathbf{x}) < 0 \end{cases} \quad 3-18$$

Furthermore, the polar crack tip coordinates are given as

$$r = \sqrt{\psi^2(\mathbf{x}) + \phi^2(\mathbf{x})} \quad \text{and} \quad \theta = \arctan \frac{\psi(\mathbf{x})}{\phi(\mathbf{x})}. \quad 3-19$$

The enriched nodes corresponding to the crack tip enrichment can also be determined through the use of the level set functions defining the crack. Consider an element where the maximum and minimum values of $\psi(\mathbf{x})$ and $\phi(\mathbf{x})$ are given as ψ_{\max} , ψ_{\min} , ϕ_{\max} , and ϕ_{\min} . Then an element is enriched with the Heaviside enrichment when

$$\phi_{\max} < 0 \quad \text{and} \quad \psi_{\max} \psi_{\min} \leq 0 \quad 3-20$$

and the crack tip enrichment when

$$\phi_{\max} \phi_{\min} \leq 0 \quad \text{and} \quad \psi_{\max} \psi_{\min} \leq 0. \quad 3-21$$

Therefore, the extended finite element and level set methods complement one another well for the tracking of the location of the cracks. The representation of cracks in three-dimensions [54, 58, 60] follows a similar methodology. In practice the level sets are defined in only a narrow band about the crack as discussed in Chapter 2 or the fast marching method [54, 60] is used.

The convergence rate of XFEM with crack enrichment functions has been an area of interest [65, 102-107], particularly with respect to the challenges presented by the partially enriched or blending elements caused by the crack tip enrichment. No blending issues exist with the Heaviside function as it vanishes along all element boundaries. It was noticed by Stazi [104] that the convergence rate for the XFEM was lower than the equivalent traditional finite element problem. Chessa [108] identified that the partially enriched crack tip elements lead to parasitic terms in the displacement approximation and introduced an enrichment dependent assumed strain model to increase the convergence rate. Fries [102] introduced a linearly decreasing enrichment weight function in the blending elements to increase convergence. An area [103, 109, 110] instead of single element crack tip enrichment has also been shown to increase convergence. Through the use of these methods the convergence rate of cracked domains with the XFEM has become equivalent to the equivalent traditional finite element problem [65, 102, 107].

Inclusion Enrichment Functions

The modeling of material interfaces independent of the finite element mesh through the element-free Galerkin [111] as well as partition of unity finite element method [55, 61, 63, 65, 66, 112-115] has been studied. The enrichment function should

incorporate the behavior of the weak discontinuity, i.e., continuous displacement, but discontinuous strain. The Hadamard condition [113] given by

$$\mathbf{F}^+ - \mathbf{F}^- = \mathbf{a} \otimes \mathbf{n}^+ \quad 3-22$$

where \mathbf{F} is the deformation gradient, \mathbf{n}^+ is the outward normal material interface, and \mathbf{a} is an arbitrary vector in the plane. The Hadamard condition must be satisfied by the chosen enrichment function.

Sukumar [113] first introduced the use of the absolute value enrichment in terms of the level set function $\zeta(\mathbf{x})$, which gives the shortest signed distance from a given point to the interface between the two materials. Therefore, the enrichment function takes the form:

$$v(\mathbf{x}) = |\zeta(\mathbf{x})|. \quad 3-23$$

The enrichment function is assumed to be nonzero only over the domain of support for the enriched nodes, as with the crack enrichment function. For a bi-material boundary-value benchmark problem the absolute value enrichment given by Eq. 3-23 led to a convergence rate which was lower than the equivalent traditional finite element method problem where the mesh conforms with the material interface. It was hypothesized that the poor convergence was related to the blending elements containing a partial enrichment. In an attempt to improve the convergence rate a smoothing algorithm was introduced to reduce the effects of the blending elements which increased the convergence rate, but did not equal the traditional finite element method.

Moës [55] studied modeling complex microstructure geometries with the use of level set defined material interfaces and introduced a new enrichment function. The modified absolute value enrichment takes the form:

$$\Upsilon(\mathbf{x}) = \sum_I N_I(\mathbf{x}) |\zeta_I| - \left| \sum_I N_I(\mathbf{x}) \zeta_I \right|. \quad 3-24$$

Note that the enrichment function given by Eq. 3-24 is zero at all nodes and thus, does not need to be shifted such that traditional degrees of freedom are recovered automatically. If an interface corresponds to the mesh, then no nodes are enriched as the enrichment function will be zero and the problem will be equivalent to the traditional finite element problem. The same benchmark problem considered by Sukumar [113] was considered as well as a similar problem in three-dimensions. In two-dimensions the convergence rate was shown to equal the traditional finite element method. In three-dimensions the convergence rate was slightly less than the traditional finite element method. This method is considered the current state-of-the-art for modeling inclusions with the XFEM.

Pais [112, 115] considered an element-based enrichment instead of nodal enrichment where the displacement approximation took the form

$$\mathbf{u}^h(\mathbf{x}) = \sum_I N_I(\mathbf{x}) \mathbf{u}_I + \nu(\mathbf{x}) \mathbf{a}_e \quad 3-25$$

where $\nu(\mathbf{x})$ is a piecewise linear enrichment function where

$$\nu(\mathbf{x}) = \begin{cases} \nu_I(\mathbf{x}) = 0 \\ \nu(\zeta(\mathbf{x}) = 0) = 1 \end{cases} \quad 3-26$$

and \mathbf{a}_e are elemental degrees of freedom. Thus, the enrichment function vanishes at all nodes and takes a value of one at the interface locations. The proposed method allows for the number of elemental degrees of freedom to be equal to the number of dimensions of the problem. The resulting system of equations needs fewer degrees of freedom than either the traditional or extended finite element method to represent the

same domain. It was found that the convergence rate is comparable to the absolute value enrichment given by Eq. 3-23, due to errors in the prediction of the shear stress distribution in two and three-dimensions. A comparison of the enrichment functions for Eqs. 3-23-3-25 is given for the case of a bi-material bar shown in Figure 3-2. A comparison of the enrichment functions and locations of the enriched degrees of freedom for the absolute value, modified absolute value and element-based enrichment functions is given in Figure 3-3.



Figure 3-2. One-dimensional bi-material bar problem.

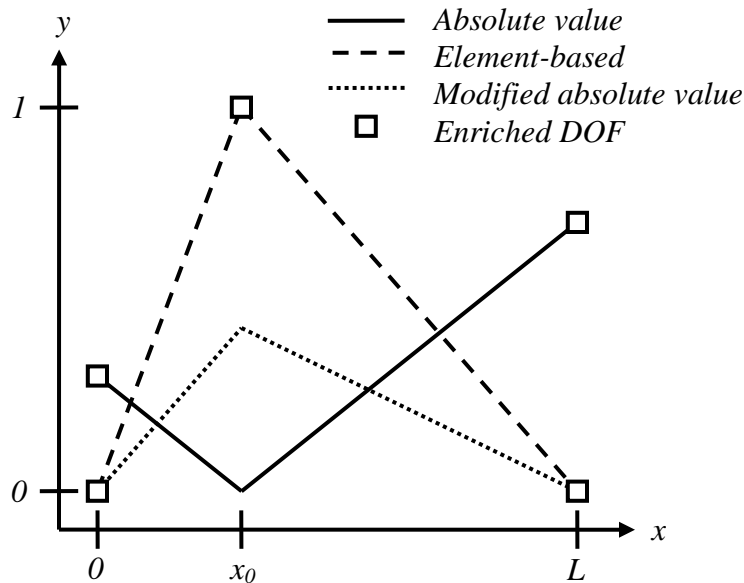


Figure 3-3. Comparison of the various inclusion enrichment functions and locations of the enriched degree(s) of freedom for a one-dimensional bar.

The problem given in Figure 3-2 can be solved using the absolute value enrichment, modified absolute value enrichment, or element-based enrichment all of

which yield equivalent final answers. When additional elements are considered, the smoothing of the absolute value enrichment presents a challenge not found with the modified absolute value or element-based enrichment for recovering the theoretical displacement. Due to the improved convergence rate for the modified absolute value enrichment this method is the most popular approach in the literature for modeling inclusions with XFEM. For the most part, continued work in the area of modeling inclusions in the XFEM tends to application oriented instead of focusing upon the development of enrichment functions which offer improved performance.

Other work on modeling inclusions in the XFEM include a unified model for the representation of arbitrary discontinues and discontinuous derivatives [61]. The imposition of constraints along moving or fixed interfaces was considered by Zilian [114]. Dirichlet and Neumann boundary conditions for arbitrarily shaped interfaces were presented for a general enrichment function. Instead of Lagrange multiplier [116, 117] or penalty method [118] approaches, a mixed-hybrid method was introduced. Constant boundary tractions, prescribed displacement differences and prescribed interfacial displacement states were applied to a bi-material problem. Hettich [119, 120] studied the modeling and failure of the interface between fiber and matrix in composite materials.

Void Enrichment Function

Daux [89] was the first to represent voids with the XFEM. Sukumar [113] later extended the void enrichment to take advantage of the use of the $\chi(\mathbf{x})$ level set function to track the void. Unlike the other enrichment functions presented here, the void

enrichment function does not require additional DOF; instead the displacement approximation for a domain with a hole takes the form

$$\mathbf{u}^h(\mathbf{x}) = V(\mathbf{x}) \sum_I N_I(\mathbf{x}) \mathbf{u}_I \quad 3-27$$

where $V(\mathbf{x})$ takes a value of 0 inside the void and 1 anywhere else. In practice, integration is simply skipped where $\chi(\mathbf{x}) < 0$. Additionally, nodes whose support is completely within the void are considered fixed DOF.

Integration of Element with Discontinuity

An area where the XFEM differs from the classical finite element method is on the scheme used to perform the numerical integration of Eq. 3-6 as challenges arise in elements which contain a discontinuity. Standard Gauss quadrature [23] requires that the integrands are smooth, which is not the case for an element containing a strong or weak discontinuity. The approach introduced by Moës [25] was to divide a two-dimensional element into a set of triangular subdomains, where the discontinuity was placed along the boundary of one of the subdomains. Integration would then be performed over each subdomain, resulting in a series of integrations over continuous domains. The common number of gauss points for integration in each triangular subdomain with the Heaviside enrichment is 3 while 7 are used for the crack tip enrichment functions given in Eq. 3-16 [73]. An example of an element completely cut by a crack as well as containing a crack tip and the associated subdomains for integration are shown in Figure 3-4. The creation of the subdomains is straightforward with the use of Delaunay tessellation for the nodal coordinates along with the coordinates of the zero level set of $\psi(\mathbf{x})$ in the parametric space.

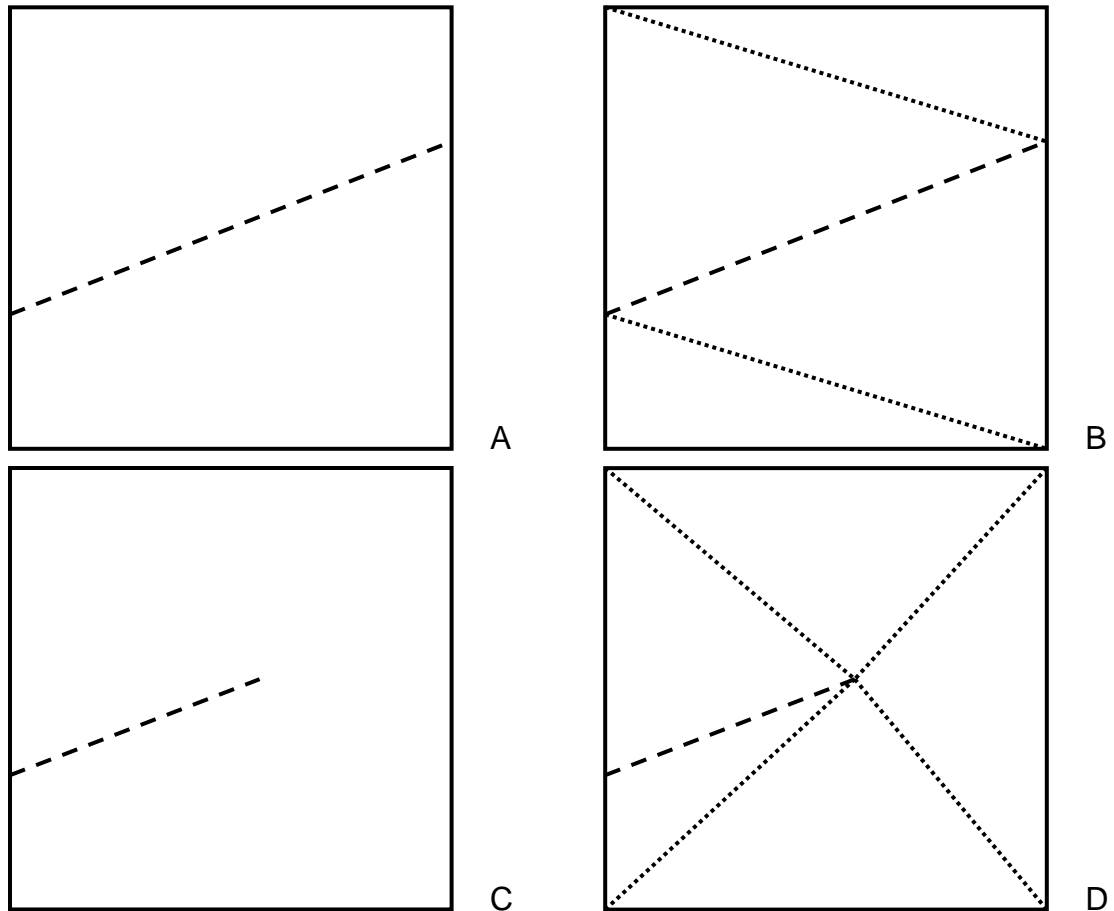


Figure 3-4. Elements containing a discontinuity and the continuous subdomains for integration. A) element cut by crack, B) element cut by crack divided into four continuous subdomains, C) element containing crack tip, D) element containing crack tip divided into 5 continuous subdomains.

Elguedj [37, 38] introduced a hybrid integration method for the case of modeling the evolution of plasticity of an elastic-plastic crack on a structured mesh. Elements which were within a given radius around the crack tip were subdivided into 16 square subdomains. Within each square subdomain, 16 gauss points were used in order to track the evolution of plasticity within the model. As the crack evolved, all gauss points associated with previous plasticity were updated and additional elements were divided into subdomains according to crack growth. Note that 256 gauss points are used for an elastic-plastic crack enriched element, while one would expect an average of 35 gauss

points for the case without plasticity. The implication is that in addition to solving a nonlinear system of equations to capture the plasticity based on the HHR singularity model, more gauss points will be used for a comparable simulation. This leads to a computational problem which is much more demanding if plasticity is to be modeled with XFEM.

In three-dimensions, it is possible to decompose elements cut by planar cracks into a series of tetrahedrons [75] in a similar fashion to that of two-dimensional elements. Mousavi also explored integration over arbitrary polygons [121] with an application to XFEM [121] and through the use of the Duffy transformation [122], showing excellent accuracy in the presence of singularities. Sukumar [123] presented a method for the integration of an arbitrary polygon based on Schwarz-Christoffel conformal mapping. Yamada [124] presented a hybrid numerical quadrature scheme based on a modified Newton-Cotes quadrature scheme. Park [125] introduced a mapping method for integration of discontinuous enrichments. Other methods are detailed by Belytschko [63] and Fries [66].

XFEM Software

Due to the relatively short history of the XFEM, commercial codes which have implemented the method are not prevalent. There are however, many attempts to incorporate the modeling of discontinuities independent of the finite element mesh by either a plug-in or native support [66, 126-129]. As most of these implementations are works in progress there are various limitations on their practical use.

Abaqus[®]

In 2009, the Abaqus[®] 6.9 release [128] introduced basic XFEM functionality to the Abaqus[®] CAE environment. The Abaqus[®] implementation of the XFEM is somewhat

different from that which was previously presented in this chapter. The implementation is based on the phantom node method which was introduced by Hansbo [130] and subsequently modified by Song [131] and Rabczuk [132]. The fundamental difference between this implementation and the original XFEM is that the discontinuity is described by superimposed elements and phantom nodes. In effect, an element is only defined in an area where an element is continuous. Several elements are combined together such that the total behavior of a discontinuous element is described. The method implemented by Abaqus[®] considers a cohesive crack model, which is only enriched with the Heaviside function given by Eq. 3-18. Note that it has been shown repeatedly that the use of only the Heaviside enrichment leads to poor accuracy of the resulting J-integral calculation [129]. As a result of this enrichment scheme, all enriched elements must be completely cut by the crack, as no crack tip field is considered.

Some limitations with modeling crack growth within Abaqus[®] using the XFEM are:

- Only the STATIC analysis procedure is allowed
- Only linear continuum elements are allowed with or without reduced integration
- No fatigue crack growth models are available
- No intersecting or branching cracks are allowed
- A crack may not turn more than 90° within a particular element

The Abaqus[®] 6.9: Extended Functionality [127] update allows for energy release rate and stress intensity factors to be evaluated for three-dimensional cracked domain. There is currently no method available for the extraction of stress intensity factors in two-dimensions. In practice, the modeling of crack growth within Abaqus[®] with the current implementation of the XFEM is challenging. As the formulation is based on the cohesive model the same challenges exist of solving the system of equations as with

cohesive elements and methods such as viscous regularization must be applied to solve the system of equations. Care must be taken to choose the regularization parameters in a way that has a minimal impact on the resulting solution. The Abaqus® 6.10 [133] update enables parallel processing of some XFEM simulations. The Abaqus® 6.10: Extended Functionality [36] update enables low cycle fatigue predictions.

MATLAB® XFEM Code (MXFEM)

Basic functionality of the XFEM was implemented by Pais [134] in MATLAB® for two-dimensional plane stress and plane strain problems. This code has been given the name MATLAB® XFEM Code (MXFEM) rectangular domain may be defined with a structured grid of linear square quadrilateral elements with arbitrary loading and boundary conditions. Enrichments provided include the homogeneous [25] crack, inclusion [55] and void [89, 113]. All discontinuities are tracked using the level set method detailed in Chapter 3 and enrichment functions are calculated from level set values as detailed previously in this chapter. The $\phi(\mathbf{x})$ and $\psi(\mathbf{x})$ level set functions track the crack, the $\chi(\mathbf{x})$ level set function tracks the voids, and the $\zeta(\mathbf{x})$ level set function tracks the inclusions. Integration of enriched elements is done through subdivision of elements into triangular regions [25, 73].

A variety of plotting outputs may be requested including: level set functions, finite element mesh, deformed finite element mesh, elemental and contours of stress, and stress-intensity factor history for growing cracks. A graphical user interface (GUI) is available which offers simplified functionality compared to the direct modification of the input file. The GUI writes an input file based on the values of the GUI and then solves the problem. An example of the GUI is given in Figure 3-5. Examples of some of these

plots are given for the geometry shown in Figure 3-6, Figure 3-7, and Figure 3-8, which contains a circular inclusion below the crack and a void above the crack.

The domain form of the contour integrals [18, 19] is used to calculate the mixed-mode stress intensity factors. The mixed-mode stress intensity factors are used in the critical plane approach [133] or the maximum circumferential stress criterion [18] to give the direction of crack extension. Crack growth may be modeled using either a constant increment of growth or a fatigue crack growth model, such as Paris model [34] or a modified Paris model [14, 27] which considers the effects of variable amplitude loading. Four models [133, 135-137] are available for the conversion of the mixed-mode stress intensity factors into an equivalent stress intensity factor range. For the case of variable amplitude loading a separate input file may be used to define the cycle-dependent loading parameters for the two-dimensional state of stress. Either the forward Euler method or surrogate models as presented in Chapter 4 can be used in the integration of the fatigue model. Surrogate models are used through the use of the SURROGATES Toolbox [138]. All crack growth problems are solved using the reanalysis algorithm presented in Chapter 5.

Additional functionality includes an optimization algorithm for finding some optimum crack location and the ability to define a variable load history. The code has been prepared in an attempt to facilitate other models for crack growth direction, equivalent stress intensity factor, and fatigue crack growth models. Benchmark problems for the various enrichment functions are provided in Appendix A including: crack, inclusion, and void enrichment functions, fatigue crack growth, and optimization to identify the crack location with maximum energy release rate for a plate with a hole.

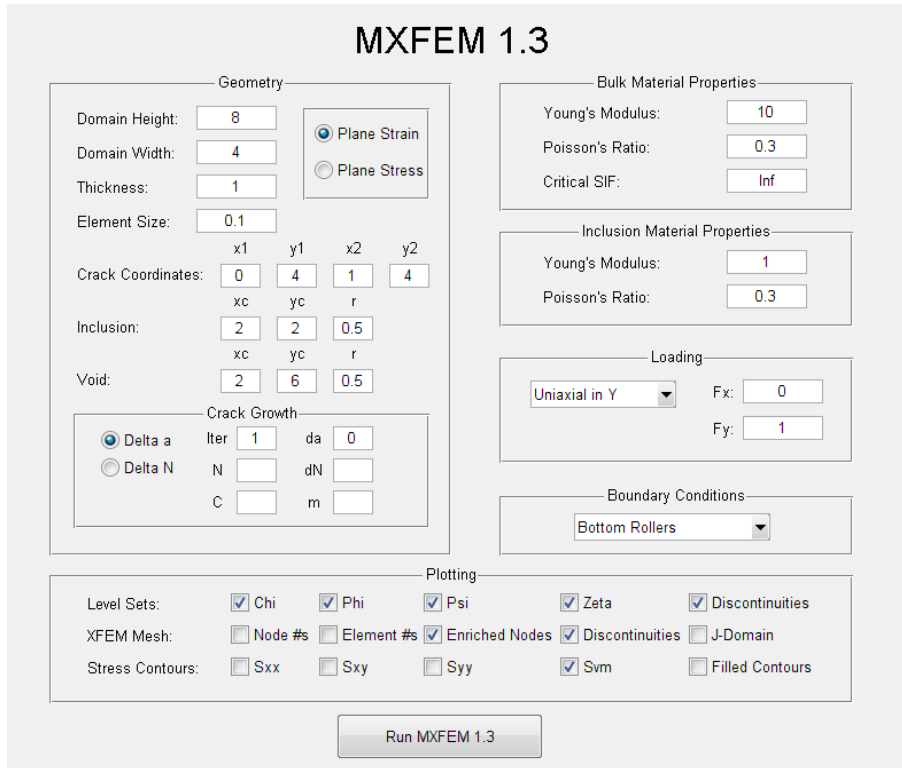


Figure 3-5. MXFEM GUI for automated input file creation.

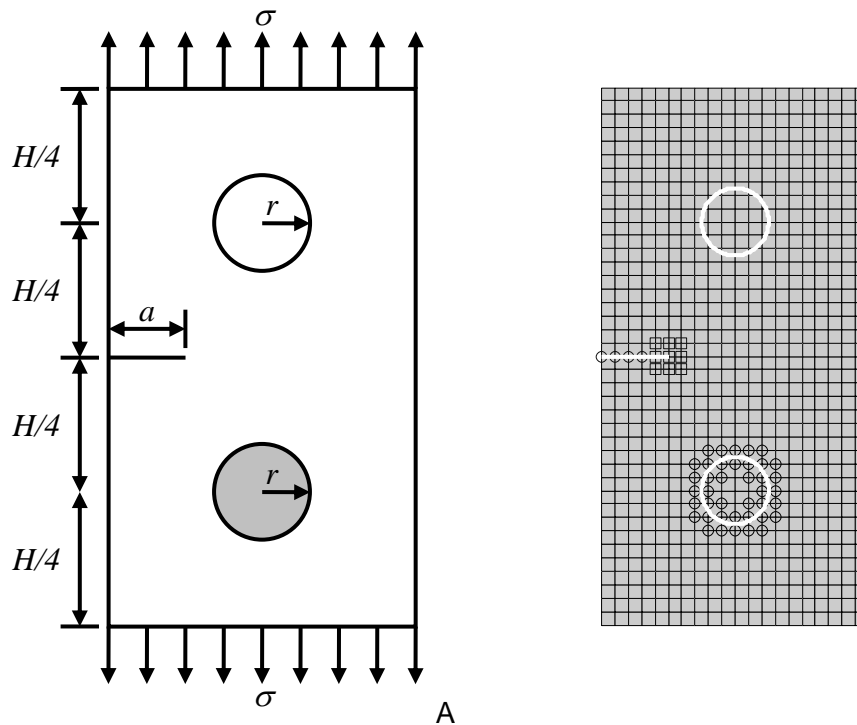


Figure 3-6. Example problem to show plots generated by MXFEM. A) The geometry being considered, B) Example of the mesh output from MXFEM where circles and squares denote the Heaviside and crack tip enriched nodes and the circles denote the inclusion enriched nodes.

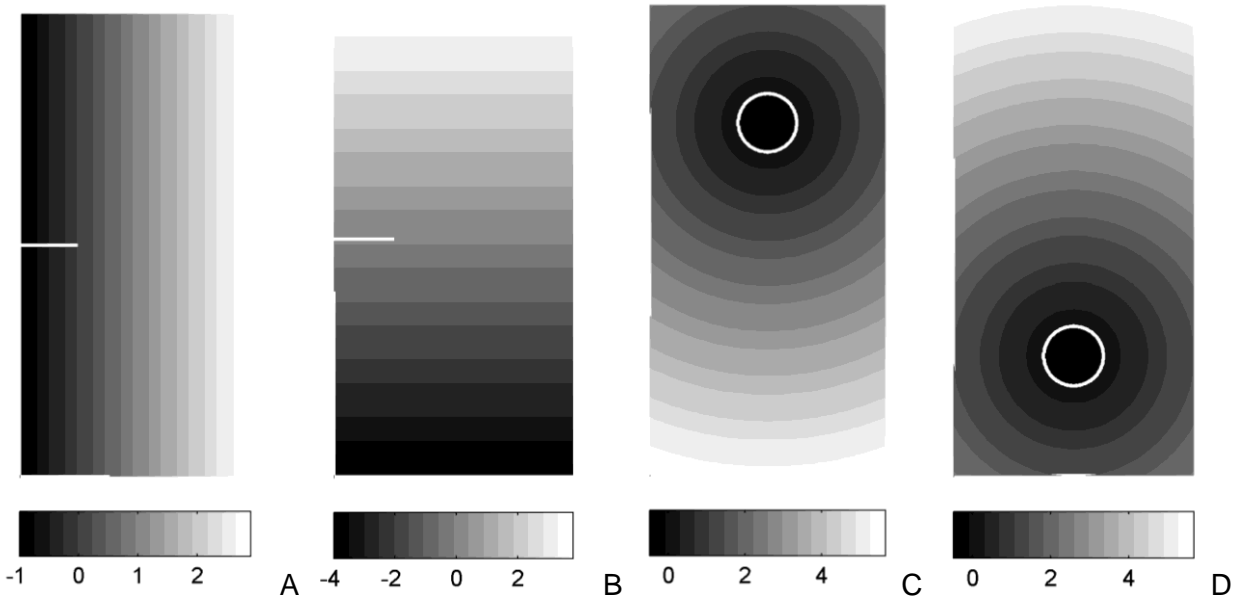


Figure 3-7. Example of the level set functions output from MXFEM. A) $\phi(\mathbf{x})$, B) $\psi(\mathbf{x})$, C) $\chi(\mathbf{x})$, D) $\zeta(\mathbf{x})$.

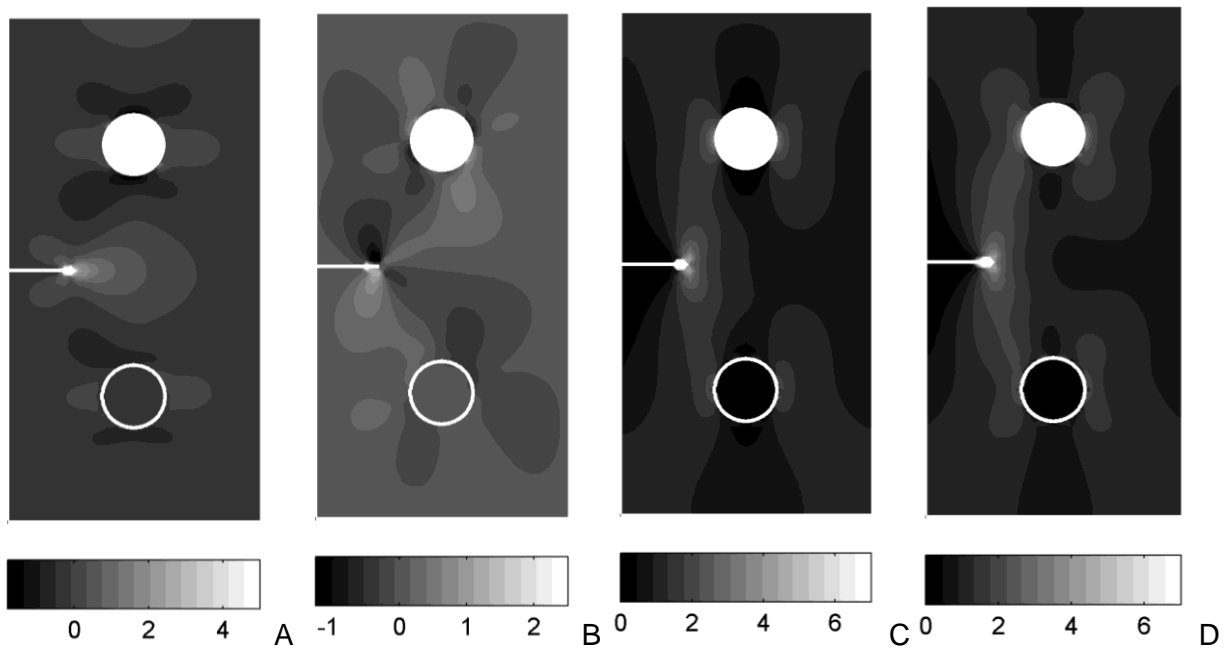


Figure 3-8. Example of the stress contours output from MXFEM. A) σ_{xx} , B) σ_{xy} , C) σ_{yy} , D) σ_{vm} .

Other XFEM Implementations

Bordas [69] implemented the XFEM as a object-oriented library in C++. Cenaero [139] has implemented XFEM functionality into the Morfeo finite element environment.

Giner [129] implemented the XFEM in Abaqus[®] with the traditional crack tip enrichment scheme for modeling two-dimensional growth through the use of user defined elements. Global Engineering and Materials, Inc. [126, 140] is developing a XFEM-based failure prediction tool as an Abaqus[®] plug-in which includes a small time scale fatigue model [24] for variable amplitude loading. Sukumar [73, 74] implemented the XFEM in Fortran, specifically the finite element program Dynaflow[®]. Wyart [141] discussed the implications of the implementation of the XFEM in general commercial codes. Some amount of functionality is also available in getfem++ [142] and openxfem++ [143].

Summary

The XFEM allows for strong and weak discontinuities to be represented independent of the finite element mesh by incorporating discontinuous functions into the displacement approximation through the partition of unity finite element method. Additional nodal degrees of freedom are introduced at the nodes of elements cut by a discontinuity. An assortment of enrichment functions are available for a variety of crack tip conditions and the Heaviside step function is used to model the crack away from the tip. Elastic-plastic crack tip enrichment functions are available for materials which power-law hardening based on the HHR singularity model. The stress intensity factor results do not show a significantly different prediction in stress intensity factor over the traditional crack tip enrichment method, but require significantly more computational resources for a given analysis. Inclusions are modeled using the modified absolute value enrichment, which shows convergence equivalent to that of the classical finite element method. Voids can be incorporated through the use of a step function and without additional nodal degrees of freedom. Integration of elements containing

enriched degrees of freedom, and therefore a discontinuity require special integration treatment through the use of either a subdivision or equivalent algorithm.

As the discontinuities do not correspond to the finite element mesh, some other method must be used to track the discontinuities. The level set method for open sections is used to track any cracks in the domain. The level set method for closed sections is used to track inclusions and voids. The level set values are used as part of the definition of the enrichment functions, leading to a symbiotic relationship between the extended finite element and level set methods.

A version of the XFEM for the modeling of cohesive cracks has been introduced in Abaqus[®] 6.9, but it is not without its limitations. An implementation within MATLAB[®] had been completed here. The XFEM is also available through the use of plug-ins or some open source finite element codes.

CHAPTER 4 CRACK GROWTH MODEL

Stress Intensity Factor Evaluation

The most common way to extract the mixed mode stress intensity factors is through the use of the domain form of the interaction integrals [16, 18, 19, 85] in two [25, 73, 89] or three-dimensions [54, 59, 75]. The domain form of the interaction integrals is an extension of the J-integral originally introduced by Cherepanov [144] and Rice [17]. In the domain form, the line integral specified by the J-integral is converted to an area integral which is much more amenable to use with finite element simulations. As the J-integral is used to calculate the energy release rate for a given crack, the interaction integrals are used to extract the mixed-mode stress intensity factors. This method has been shown to have excellent accuracy when applied to suitable meshes for many crack conditions including homogenous [25], bi-material [85], and branching [89] cracks. Other methods [63, 64, 66] have also been explored in the literature.

For a general mixed-mode homogeneous crack in two-dimensions the energy release rate G can be expressed in terms of the relationship between the J-integral, stress intensity factors and effective Young's modulus E_{eff} as

$$G = J = \frac{K_I^2}{E_{eff}} + \frac{K_{II}^2}{E_{eff}} \quad 4-1$$

where E_{eff} is defined by the state of stress as

$$E_{eff} = \begin{cases} E & \text{plane stress} \\ \frac{E}{1-\nu^2} & \text{plane strain} \end{cases} \quad 4-2$$

where E is Young's modulus and ν is Poisson's ratio. The J-integral takes the form

$$J = \int_{\Gamma} \left(W n_1 - \sigma_{jk} n_j \frac{\partial u_k}{\partial x_1} \right) d\Gamma \quad 4-3$$

where W is the strain energy density. Equation 4-3 can be rewritten in the equivalent form using the Dirac delta which is easier to implement in finite element code as

$$J = \int_{\Gamma} \left(W \delta_{1j} - \sigma_{ij} \frac{\partial u_i}{\partial x_1} \right) n_j d\Gamma. \quad 4-4$$

In order to calculate the mixed-mode stress intensity factors, two displacement and stress states are superimposed onto one another. Auxiliary stress and displacement states are superimposed onto the stress and displacement solution from XFEM. The auxiliary stress and displacement states at the crack tip introduced by Westergaard [145] and Williams [146] for a homogenous crack and by Sukumar [85] for a bi-material crack are used in the calculation of the mixed-mode stress intensity factors. The auxiliary stress and displacement states for a homogeneous crack are given in Appendix B. Hereafter, the XFEM states are given as $u_{ij}^{(1)}$, $\varepsilon_{ij}^{(2)}$, and $\sigma_{ij}^{(2)}$ while the auxiliary states are given as $u_{ij}^{(2)}$, $\varepsilon_{ij}^{(1)}$, and $\sigma_{ij}^{(1)}$. The superposition of stress states into Eq. 4-4 leads to

$$J^{(1+2)} = \int_{\Gamma} \left[\frac{1}{2} (\sigma_{ij}^{(1)} + \sigma_{ij}^{(2)}) (\varepsilon_{ij}^{(1)} + \varepsilon_{ij}^{(2)}) \delta_{1j} - (\sigma_{ij}^{(1)} + \sigma_{ij}^{(2)}) \frac{\partial (u_i^{(1)} + u_i^{(2)})}{\partial x_1} \right] n_j d\Gamma. \quad 4-5$$

The expansion of the terms of Eq. 4-5 allows for the J-integral to be separated to the auxiliary state $J^{(2)}$, XFEM state $J^{(1)}$, and interaction state $I^{(1,2)}$ given by

$$I^{(1,2)} = \int_{\Gamma} \left[W^{(1,2)} \delta_{1,j} - \sigma_{ij}^{(1)} \frac{\partial u_i^{(2)}}{\partial x_1} - \sigma_{ij}^{(2)} \frac{\partial u_i^{(1)}}{\partial x_1} \right] n_j d\Gamma \quad 4-6$$

where $W^{(1,2)}$ is the interaction strain energy density given as

$$W^{(1,2)} = \sigma_{ij}^{(1)} \varepsilon_{ij}^{(2)} = \sigma_{ij}^{(2)} \varepsilon_{ij}^{(1)}. \quad 4-7$$

The two superimposed stress states can be expressed using Eq. 4-1 after rearrangement as

$$J^{(1+2)} = J^{(1)} + J^{(2)} + \frac{2(K_I^{(1)}K_I^{(2)} + K_{II}^{(1)}K_{II}^{(2)})}{E_{eff}}. \quad 4-8$$

Therefore, from Eqs. 4-6 and 4-8, the interaction state is given as

$$I^{(1,2)} = \frac{2(K_I^{(1)}K_I^{(2)} + K_{II}^{(1)}K_{II}^{(2)})}{E_{eff}}. \quad 4-9$$

The stress intensity factors for the XFEM state $K_I^{(1)}$ and $K_{II}^{(1)}$ are given by selecting $K_I^{(2)} = 1$ and $K_{II}^{(2)} = 0$, followed by $K_I^{(2)} = 0$ and $K_{II}^{(2)} = 1$ such that $K_I^{(1)}$ and $K_{II}^{(1)}$ are:

$$K_I^{(1)} = \frac{I^{(1, \text{Mode I})} E_{eff}}{2} \quad 4-10$$

where $I^{(1, \text{Mode I})}$ is the interaction integral for $K_I^{(2)} = 1$ and $K_{II}^{(2)} = 0$ and

$$K_{II}^{(1)} = \frac{I^{(1, \text{Mode II})} E_{eff}}{2} \quad 4-11$$

where $I^{(1, \text{Mode I})}$ is the interaction integral for $K_I^{(2)} = 0$ and $K_{II}^{(2)} = 1$.

The interaction integral in Eq. 4-6 is converted from a line integral into an area integral and a smoothing function q_s which takes a value of 1 on the interior of the line integral defined by Eq. 4-6 and a value of 0 outside of the integral. Elements for the integration are selected by choosing a radius from the crack tip. When this radius becomes sufficiently large the integral becomes path-independent; i.e., any path larger than the path-independent radius r_{ind} will yield equivalent solutions to Eq. 4-6. In practice

a radius of three elements about the crack tip is typically sufficient for path-independence. An example of the elements contained within a given radius from the crack tip is given in Figure 4-1. The divergence theorem is used to create the equivalent area integral

$$I^{(1,2)} = \int_A \left[\sigma_{ij}^{(1)} \frac{\partial u_i^{(2)}}{\partial x_1} - \sigma_{ij}^{(2)} \frac{\partial u_i^{(1)}}{\partial x_1} - W^{(1,2)} \delta_{1j} \right] \frac{\partial q_s}{\partial x_j} dA \quad 4-12$$

which is simpler to implement in the finite element environment.

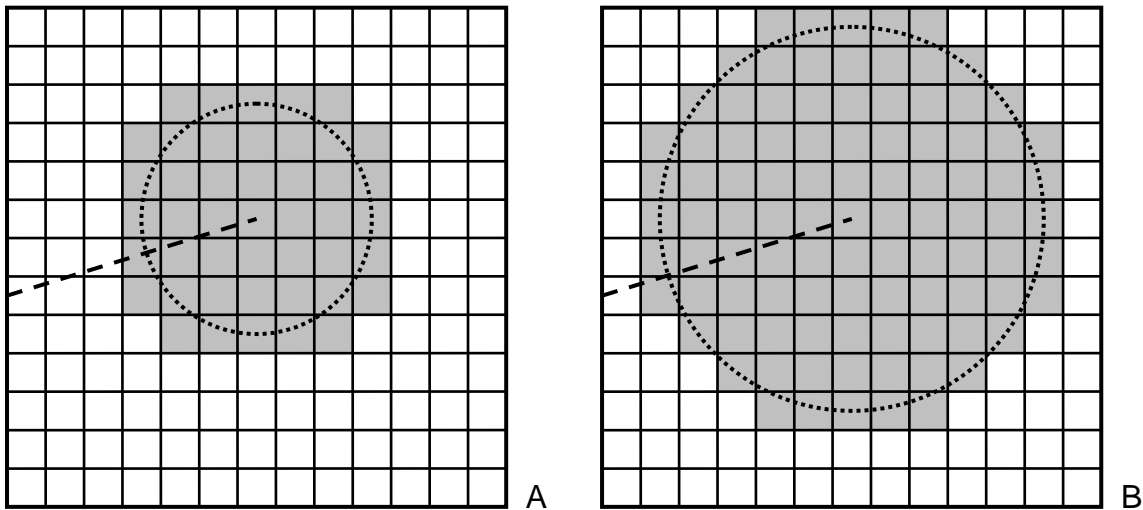


Figure 4-1. The elements within a specified radius for path-independence. A) Radius of three elements, B) Radius of 5 elements.

Other methods have also been used to extract the mixed-mode stress intensity factors using XFEM. Duarte [147] used a least squares fit of the localized stress state around the crack tip to extraction the stress intensity factors. Karihaloo [64] included higher-order terms of the asymptotic crack tip expansion in two-dimension which allowed for the stress intensity factors to be obtained directly without the use of interaction integrals. No equivalent extension has been performed in three-dimensions [63]. Lua [126, 148] introduced nodes along the crack fronts which were used with the crack-tip opening displacement [15] to calculate the mixed-mode stress intensity factors.

Recall that the crack-tip opening displacement approach for finding stress intensity factors is only valid for linear elastic cracks. Sukumar [60] attempted to evaluate the stress intensity factors directly from the enriched degrees of freedom corresponding to the crack tip enrichment function for pure mode I problem, but the accuracy of the stress intensity factors was found to be insufficient. A similar method was introduced by Liu [149] with much better results for homogeneous and bi-material cracks.

Crack Growth Direction

The direction of crack propagation is accepted to be a function of the mixed-mode stress intensity factors present at a crack tip. While there are several criteria available for both two [21, 133, 150-153] and three-dimensions [133, 153], in general they only differ in the angle of the initial kink, but then converge to similar crack paths [73]. In two-dimensions, these methods tend to give the angle of crack extension, which in general is the direction which will minimize K_{II} .

In two-dimensions the main criteria for the crack growth direction are the critical plane approach [133], maximum circumferential stress [151], maximum energy release rate [152] and the maximum strain energy density criterion [21]. Other criterion available in the literature are the criterion of energy release rates and the generalized fracture criterion [153]. The criterion which is most amenable to modeling crack growth with finite elements is the maximum circumferential stress, as the growth direction θ_c is given in a closed form solution in terms of the mixed-mode stress intensity factors. The maximum circumferential stress criterion [153] is given as the angle θ_c given by

$$\theta_c = -\arccos\left(\frac{2K_{II}^2 + K_I\sqrt{K_I^2 + 8K_{II}^2}}{K_I^2 + 9K_{II}^2}\right). \quad 4-13$$

Alternative, but equivalent formulas are given by Moës [25] as

$$\theta_c = 2 \arctan \left[\frac{1}{4} \left(\frac{K_I}{K_{II}} - \text{sign}(K_{II}) \sqrt{\left(\frac{K_I}{K_{II}} \right)^2 + 8} \right) \right] \quad 4-14$$

and Sukumar [73]

$$\theta_c = 2 \arctan \left[\frac{-2(K_{II}/K_I)}{1 + \sqrt{1 + 8(K_{II}/K_I)^2}} \right]. \quad 4-15$$

The critical plane approach [133] predicts that crack growth will occur along the angle specified by α as shown in Figure 4-2 for mixed-mode I and II loading as

$$\alpha = \beta + \gamma \quad 4-16$$

where the angles β and γ are

$$\beta = \frac{1}{2} \arctan \left(\frac{2K_{II}}{K_I} \right) \quad 4-17$$

and

$$\gamma = \begin{cases} \frac{1}{2} \arccos \left[\frac{-2 + \sqrt{4 - 4(1/s^2 - 3)(5 - 1/s^2 - 4s^2)}}{2(5 - 1/s^2 - 4s^2)} \right] & s \leq 1 \\ 0 & s > 1 \end{cases}. \quad 4-18$$

The parameter s is the ratio of the Mode I and II crack growth rates as

$$s = \frac{t_{-1}}{f_{-1}} = \frac{K_{II, da/dN}}{K_{I, da/dN}} \quad 4-19$$

where $K_{I, da/dN}$ and $K_{II, da/dN}$ are the stress intensity factors corresponding to a given crack growth rate da/dN . The critical plane approach has the benefit of matching the observations of Feng [154] where the crack paths were different for equivalent magnitude loads in the axial and torsion directions.

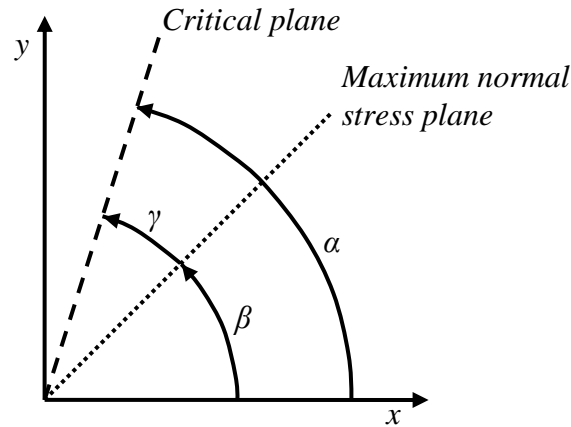


Figure 4-2. Orientations of the critical and maximum normal stress planes.

There are two options available for determining the direction of crack growth, the maximum circumferential stress and the critical plane approach. One difference between these two methods is that the critical plane approach considers the effect of the chosen material in addition to the current stress intensity factors through the use of the Mode I and II threshold stress intensity factors, which may not be available for many materials. Due to the simplicity of the maximum circumferential stress criterion and its acceptance in the XFEM literature [22, 57, 69, 71, 74, 86, 90, 129, 155], it will be the preferred method for determining the crack growth direction.

Crack Growth Magnitude

At each cycle of constant amplitude fatigue, the amount of crack growth may be on the order of nano-meters. In practice, the governing differential equation in Eq. 1-1 is solved at discrete points, which will be referred to as simulation iteration in this work. There are two main approaches presented in the literature for the amount of crack growth at a given simulation iteration for constant amplitude loading. The first method assumes that a known and finite amount of growth will occur at a given iteration. The second method assumes that some governing law, such as a fatigue crack growth law can be used to find the corresponding increment of growth at a particular iteration. For

the case of variable amplitude loading with an unknown correction factor model for the given crack geometry, the approaches used for constant amplitude loading are no longer valid and each cycle must be modeled in order to predict the magnitude and path of crack growth.

Finite Crack Growth Increment for Constant Amplitude Loading

In the literature, the selection of a constant crack growth increment is very popular [22, 57, 69, 71, 74, 86, 90, 129, 155]. At a given cycle the amount of crack growth is generally very small, approximately on the order of 10^{-8} . Therefore, it is more computationally attractive to choose a small increment of growth to represent many cycles instead of modeling them independently. The choice of Δa is almost always made *a priori*. It has been shown in the literature by Moës [25], Pais [22] and Edke [26] that the path of crack growth is related to the assumed increment. As the crack growth increment is reduced, crack path convergence can be observed. The convergence of crack path has also been related to the mesh density in the vicinity of the crack [22, 26].

Challenges with this method include selecting a Δa such that the crack path converges to the appropriate path. With a single analysis it is unclear how one can know whether or not the predicted crack path has converged. It is also unclear how to interpolate between the data points since the $a - N$ crack growth curve is nonlinear.

Direct Fatigue Crack Growth

The slow progressive failure of a structure caused by crack growth under cyclic loading is called fatigue. There are many fatigue crack growth models of varying complexity [14]. Most fatigue crack growth models are of the following form:

$$\frac{da}{dN} = f(\Delta K, R) \quad 4-20$$

where da/dN is the crack growth speed, ΔK is the stress intensity factor range, and R is the stress ratio. Many different models attempt to consider the effects of phenomenon [14] such as crack growth instability when the stress intensity factor approaches its critical value, threshold stress intensity factor, changing crack tip geometry, and elastic crack tip conditions. For a variable load history, the interactions between overloads and underloads are a crucial component of any fatigue crack growth model. An overload is a load which is substantially greater than the mean, while an underload is a load which is substantially less than the mean. Overloads increase crack tip plasticity which leads to less crack growth in resulting loading cycles. An underload has the opposite effect and leads to increased growth. The interaction of an overload and underload in subsequent cycles is not well understood. Recent work such as the state-space model [29, 30], small time scale model [24], and further modifications to fatigue models [14, 27] has resulted in better predictions of fatigue crack growth under variable amplitude loading.

Classical Paris model

The first fatigue model was presented by Paris [34] and will be referred to here as the classical Paris model. The relationship between the crack growth rate and the stress intensity factor range is given as

$$\frac{da}{dN} = C\Delta K^m \quad 4-21$$

where C is the Paris model constant, ΔK is the stress intensity factor range, and m is the Paris model exponent. The Paris model constant and exponent depend upon material properties and loading conditions which can be derived from fatigue testing data and are functions of the stress ratio R [156].

The classical Paris model given by Eq. 4-21 has limitations in its ability to model fatigue crack growth. Research has shown that for a given material there is a minimum stress intensity factor range which is required to cause crack growth which is commonly referred to as the threshold stress intensity factor range ΔK_{th} [14, 27, 157]. Crack closure [14, 28, 32] has been shown to be an important quantity to consider when modeling fatigue failure, but is not a part of the classical Paris model. The classical Paris model does not consider the applied stress ratio R which is the ratio between the minimum and maximum load for a given cycle [14, 27, 31, 33]. Therefore, for the case of variable amplitude loading where the stress ratio R is a function of the cycle number, each cycle would need its own value of C and m . For the case of loading which is variable in nature, the interaction between over-loads and under-loads is also not considered as no variable is used which considers the interaction between loading cycles.

Modified Paris model

One fatigue model which attempts to capture the behavior which is not part of the classical Paris model is a modified version of the Paris model introduced by Xiaoping [27] which will be subsequently referred to as the modified Paris model. Three additional parameters are added to the classical Paris model; ΔK_{th} which accounts for the threshold stress intensity factor range, M_R which accounts for the stress ratio effect, and M_p which accounts for the interaction between over-loads and under-loads. The modified Paris model takes the form

$$\frac{da}{dN} = C \left[(M_R M_p \Delta K)^m - \Delta K_{th}^m \right] \quad 4-22$$

where C and m are the same material properties for the classical Paris model. The value of the stress ratio correction factor M_R is given as

$$M_R = \begin{cases} (1-R)^{\beta_1} & -5 \leq R < 0 \\ (1-R)^\beta & 0 \leq R < 0.5 \\ (1.05 - 1.4R + 0.6R^2)^\beta & 0.5 \leq R < 1 \end{cases} \quad 4-23$$

The values of β and β_1 are found by calibrating fatigue data curves from several stress ratios such that they follow the same trend as is shown in Figure 4-3.

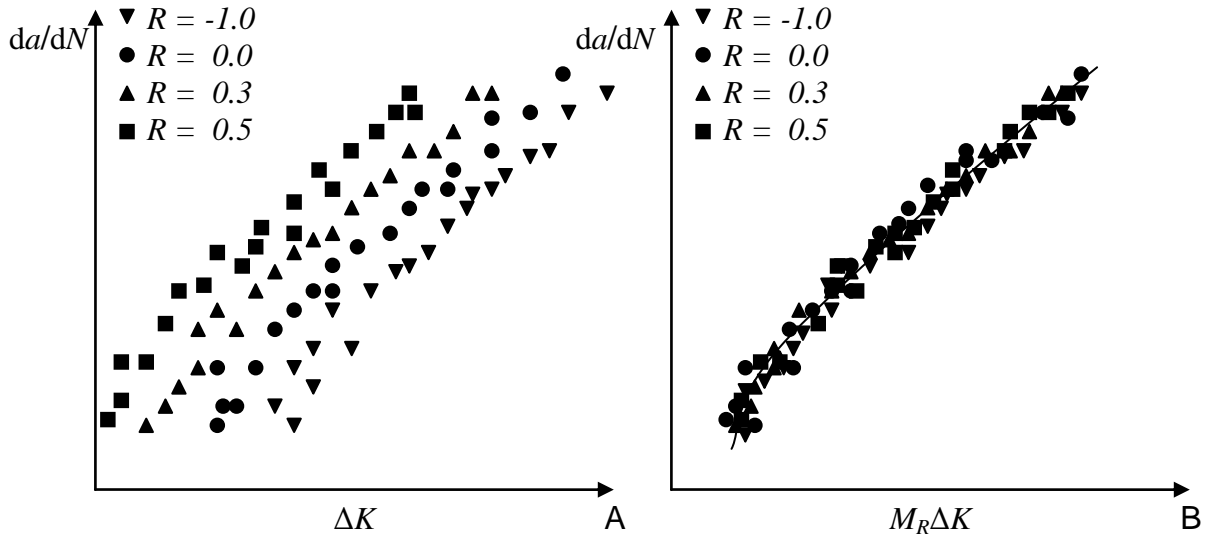


Figure 4-3. The use of the stress ratio correction factor M_R to condense the various stress ratios R into a single curve corresponding to $R = 0$ [27]. A) Fatigue data for some stress ratios R , B) Condensed fatigue data through the use of M_R .

The value of M_p is calculated as a function of the load interactions as

$$M_p = \begin{cases} \left(\frac{r_y}{a_{OL} + r_{OL} - a_i - r_\Delta} \right)^n & a + r_y < a_{OL} + r_{OL} - r_\Delta \\ 1 & a + r_y \geq a_{OL} + r_{OL} - r_\Delta \end{cases} \quad 4-24$$

where r_y is the plastic zone radius at the beginning of the cycle, a_{OL} is the crack length when the overload occurs, r_{OL} is the plastic zone radius when the overload occurs, a_i is

the characteristic crack length for the i th cycle, r_{Δ} is the change in plastic zone size caused by load interactions, and n is a shaping exponent determined by fitting to experimental data of overload and underload cases. These plastic zones are shown in Figure 4-4 where diameters are shown instead of radii. The plastic zone sizes follow

$$r_y = \alpha \left(\frac{K_I^{\max}}{\sigma_y^+} \right)^2; \quad r_{OL} = \alpha \left(\frac{K_I^{OL}}{\sigma_y^+} \right)^2; \quad r_{\Delta} = \alpha \left(\frac{\Delta K_u}{\sigma_y^-} \right)^2 \quad 4-25$$

where α is a plastic zone size factor, K_I^{\max} is the maximum stress intensity factor for the i th cycle, K_I^{OL} is the stress intensity factor when the overload occurs, ΔK_u is the interaction between loads given as $\Delta K_u = K_{I-1}^{\min} - K_I^{\min}$, σ_y^+ is the tensile yield stress of the material, and σ_y^- is the compressive yield stress of the material.

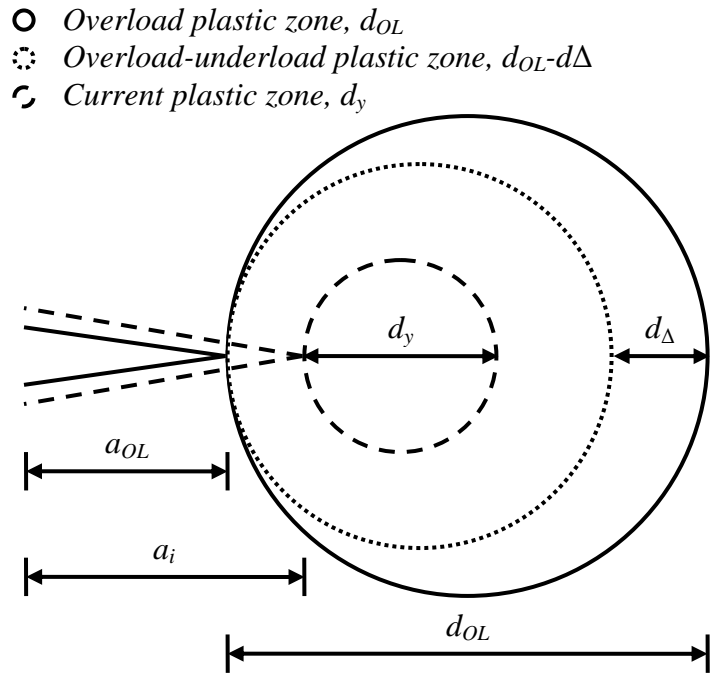


Figure 4-4. The plastic zone and crack sizes which are used in the modified Paris model to account for the effect of crack tip plasticity during load interactions.

The modified Paris model [27] has been validated for a variety of over-load, under-load, and combinations of over-load and under-load cases as well as variable amplitude

loading [27] showing improved agreement with experimental results compared to AFGROW [35] and FASTRAN [84] models and comparable agreement with the state-space model [29, 30]. While the modified Paris model proposed by Xiaoping [27] does not directly contain a crack closure model, the effects of crack closure are approximated by the tracking of plasticity associated with the interaction between the load cycles.

Equivalent Stress Intensity Factor

In order to apply the classical Paris model to mixed-mode loading, several relationships have been proposed for the calculation of a single effective stress intensity factor range which can be used in Eq. 4-21. Tanaka [136] proposed the relationship

$$K_{eq} = \sqrt[4]{K_I^4 + 8K_{II}^4} \quad 4-26$$

based on curve fitting observed experimental data. Yan [137] proposed a different correction from the maximum circumferential stress criterion as

$$K_{eq} = \frac{1}{2} \cos\left(\frac{\theta}{2}\right) \left[K_I (1 + \cos \theta) - 3K_{II} \sin \theta \right] \quad 4-27$$

where θ is given by Eqs. 4-13-4-15. Finally, a relationship based on energy release rate [135] is given as

$$K_{eq} = \sqrt{K_I^2 + K_{II}^2} . \quad 4-28$$

Liu [133] proposed a variety of equivalent stress intensity factors for any combination of Mode I, II, and III loading based upon the critical plane model. For the case of mixed-mode I and II loading the equivalent stress intensity factor is given as

$$K_{eq} = \frac{1}{B} \sqrt{(k_1)^2 + \left(\frac{k_2}{s}\right)^2 + A(k_H)^2} \quad 4-29$$

where k_1 , k_2 , and k_h are related to the given mixed-mode stress intensity factor values as

$$k_1 = \frac{K_I}{2} [1 + \cos(2\alpha)] + K_{II} \sin(2\alpha), \quad 4-30$$

$$k_2 = \frac{K_I}{2} \sin(2\alpha) + K_{II} \cos(2\alpha), \quad 4-31$$

and

$$k_H = \frac{K_I}{3}. \quad 4-32$$

The angle α in Eqs. 4-30 and 4-31 is calculated from the angle defining the critical plane as given by Eqs. 4-16 - 4-19. Finally, the constants A and B are found from the value of s from Eq. 4-19 as

$$A = \begin{cases} 0 & s \leq 1 \\ 9(s^2 - 1) & s > 1 \end{cases}, \quad 4-33$$

and

$$B = \begin{cases} \sqrt{\cos^2(2\gamma)s^2 + \sin^2(2\gamma)} & s \leq 1 \\ s & s > 1 \end{cases}. \quad 4-34$$

The choice of an equivalent stress intensity factor model is not a trivial task. The models based on the energy release rate and proposed by Tanaka do not require any information about the direction of crack propagation. Of these models, only the model of Liu considers and accounts for the effects of failure due to shear or tension according to the underlying model parameters. Therefore, this model will be the preferred choice.

Integration of Fatigue Crack Growth Model

For an arbitrary differential equation of the form $y'(x) = f(x, y(x))$ the goal is to predict the value of y_{i+1} while the current data is available up to y_i . The simplest numerical method available which is applicable to the current crack growth problem is the explicit forward Euler method [23] given as

$$y_{i+1} = y_i + hf(x_i, y_i) \quad 4-35$$

where h is the step size from x_i to x_{i+1} . Note that $f(x_i, y_i)$ is the slope of $y(x)$ at x_i ; therefore a linear approximation is being made from x_i to x_{i+1} using the slope at the x_i . This method has been popular in engineering applications because it only requires evaluating the slope at the current step, which often required expensive computational simulation. For example, in the case of crack growth simulation, $f(x_i, y_i)$ corresponds to calculating the stress intensity factor with given crack size y_i . Therefore, evaluating $f(x_i, y_i)$ requires a finite element modeling with the current geometry of the crack. If a different method, such as the backward Euler method, is used, then $f(x_{i+1}, y_{i+1})$ is required, which is the stress intensity factor corresponding to the unknown crack size y_{i+1} . Therefore, there exists a fundamental difficulty to use a numerical integration method other than the forward Euler method.

The simplest approach to integrating the Paris model for fatigue crack growth is the use of the forward Euler method. Here the stress intensity factor range at the current crack geometry is the only information needed to find the increment of growth between the current and future crack geometries. The growth increment is calculated as

$$\Delta a_i = \Delta N \left[C (\Delta K_i)^m \right] \quad 4-36$$

where i is the current increment. The corresponding number of elapsed cycles can be approximated as

$$\Delta N_i = \frac{\Delta a}{C (\Delta K_i)^m} \quad 4-37$$

for a fixed increment of crack growth. As the forward Euler method only uses the slope at the current point and linearly interpolates to the next crack size it can lead to large inaccuracies for relatively small crack growth increments. Although the physical meaning of ΔN is the number of elapsed cycles, in this model it is treated as a continuous variable as crack growth occurs over tens of thousands of cycles. Choosing a larger ΔN results in needing fewer finite element simulations while sacrificing accuracy.

Although the forward Euler method can resolve the issue related to evaluating the slope at unknown crack sizes, it has a drawback in slow convergence; the accuracy of the method is proportional to the step size, h . In crack growth analysis, the step size represents the number of fatigue loading cycles between two evaluation points. Since cracks grow slowly throughout the lifecycle of a product, a small step size means tens of thousands of simulations. Therefore, it is highly desired to use a numerical integration method that allows a larger step size, while maintaining accuracy.

There are numerous numerical methods that allow larger step sizes for integration, but the midpoint integration method is used as a demonstration tool in this paper. The midpoint method [23] generally provides a better accuracy than the forward Euler method as it takes the slope at the midpoint between the current and future data points $x_{i+1/2}$ and uses that value to approximate the interval from x_i to x_{i+1} such that

$$y_{i+1} = y_i + hf \left(x_i + \frac{h}{2}, y_{i+1/2} \right). \quad 4-38$$

As it is rare for $y_{i+1/2}$ to be evaluated directly, $y_{i+1/2}$ it can be approximated as

$$y_{i+1} = y_i + hf \left(x_i + \frac{h}{2}, y_i + \frac{h}{2} f(x_i, y_i) \right). \quad 4-39$$

The accuracy of the method is proportional to h^2 ; therefore, it allows a larger step size for the same accuracy with the forward Euler method. While the midpoint approximation specifies a crack length for the evaluation at the midpoint location, no direction is specified. For a mixed-mode crack growth problem, the direction of crack growth can be approximated based upon the first required function evaluation at $f(x_i, y_i)$. This may limit the choice of integration step size however, as in effect an Euler approximation is used for the crack growth direction while a higher-order approximation is used for the crack growth magnitude.

In terms of integrating the Paris model is the use of the midpoint method where the growth increment is calculated as

$$\Delta a_i = \Delta N \left[C (\Delta K_{i+1/2})^m \right] = \Delta N \left[C \left(\Delta K \left(a_i + \frac{\Delta N}{2} C (\Delta K (a_i))^m \right) \right)^m \right] \quad 4-40$$

where $i+1/2$ is the midpoint between the current and next increment. Similarly, ΔN_i is given as

$$\Delta N_i = \frac{\Delta a}{C (\Delta K_{i+1/2})^m} = \frac{\Delta a}{C \left(\Delta K \left(a_i + \frac{\Delta a_i}{2} \right) \right)^m} \quad 4-41$$

Here the slope at the midpoint of the current cycle is used to extrapolate ahead to $i+1$.

This leads to a better approximation of the crack size at the next increment as a more accurate approximation of the slope over the entire interval of the chosen growth increment is used. This method requires additional function evaluations at $i+1/2$ for each crack geometry, effectively doubling the number of function evaluations needed for the given simulation.

With regards to the XFEM, crack growth models have been limited primarily to the Paris model and modeling in terms of the crack growth increment Δa . Belytschko [61] used it to drive the crack growth for a plate with holes, but no specifics about how the classical Paris model was used is given. Gravouil [58] coupled the level set method to the classical Paris model, but no clear definition of the number of elapsed cycles was given. Instead the growth was governed by assuming N to be equivalent to the traditional time for the level set method. Sukumar [60] calculated the increment of crack growth Δa as

$$\frac{\Delta a}{\Delta a_{\max}} = \left(\frac{K_I}{K_I^{\max}} \right)^m \quad 4-42$$

where Δa_{\max} was taken as $0.05a_0$ for initial crack length a_0 for a value of K_I^{\max} corresponding to the maximum value of K_I along the crack front. Note that here a value for Δa_{\max} acts very similarly to that of a fixed Δa such that a small value is required to ensure convergence.

Example problem

An example is provided here where an XFEM analysis was performed on a plate with a hole as shown in Figure 4-5. The chosen plate dimensions were a width of 4 m and a height of 8 m with a hole with radius 1 m centered at (2,2) m. The edge crack has an initial length of 0.5 m. The material properties for the plate were chosen as Young's modulus of 10 MPa, Poisson's ratio of 0.33, Paris model constant and exponent of $1.5 \cdot 10^{-10}$ and 3.8 respectively. The applied stress was 14.5 MPa. The purpose of this study was to attempt to assess the effect that the mesh density and crack growth increments Δa and ΔN on the predicted crack path as shown in Figure 4-6.

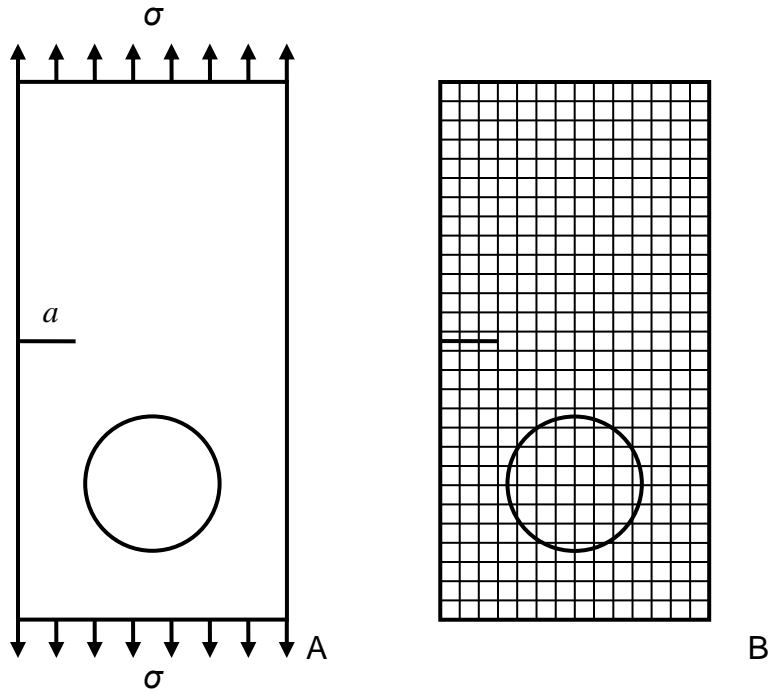


Figure 4-5. Plate with a hole subjected to tension to examine the effects of mesh density, crack growth increment, and number of elapsed cycles upon the convergence of crack path. A) Geometry, B) Example mesh.

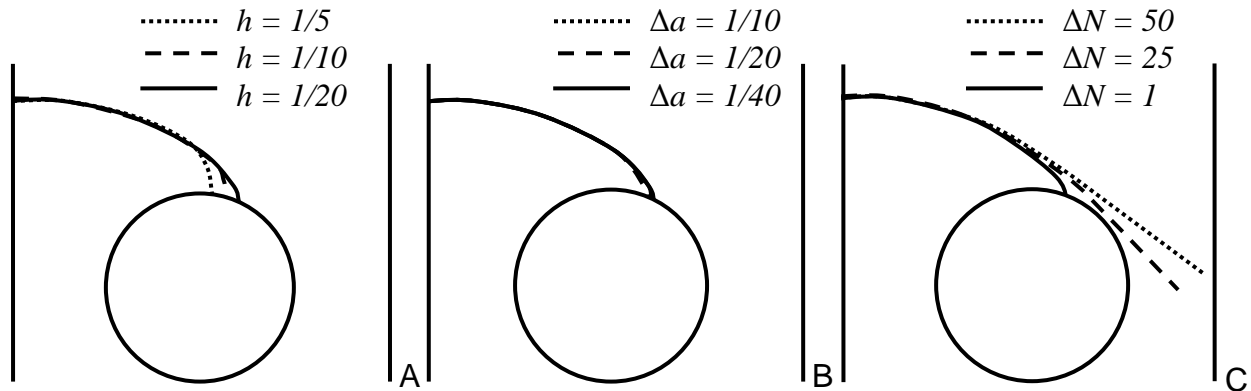


Figure 4-6. Convergence of crack path as a function of the mesh density, crack growth increment, and number of elapsed cycles. A) Mesh density, B) Δa , C) ΔN .

From Figure 4-6 it is clear that the choice of mesh size is very important as expected. Without a sufficiently refined mesh, the accuracy of the stress intensity factors will be poor leading to an inaccurate prediction of the crack growth direction. The crack path is relatively insensitive to the choice of Δa in this choice, but there is deviation between the steps if a close up image of the crack paths near the hole is

examined as in Figure 4-7. The most sensitive case is that of ΔN where the cases of $\Delta N = 25$, and 50 cycles actually miss the hole as predicted by $\Delta N = 1$. This reinforces the observations that the direct solution of a fatigue crack growth model is very sensitive to the choice of mesh, and crack growth increment.

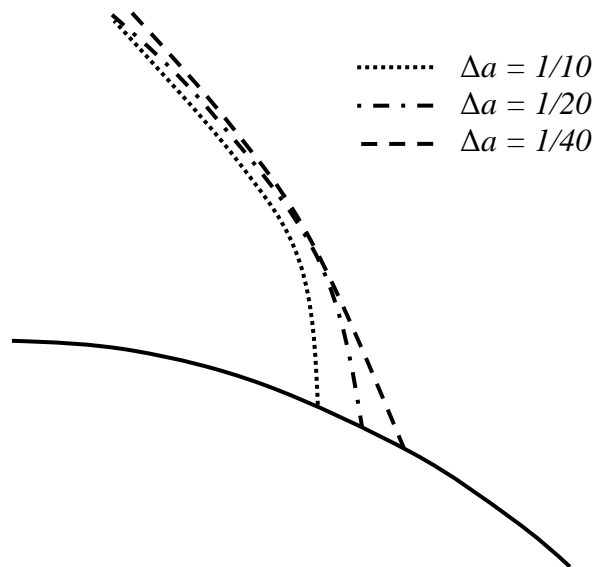


Figure 4-7. Close up view of the crack paths for Δa around the hole.

Cycle Counting Methods

In the life estimation of a given structure it is necessary to convert the history of a given loading parameter for a given structure into cycles which allow for the application of a fatigue crack growth model. For structures which experience constant amplitude loading with a constant mean stress over the loading history, this is a trivial task.

However, for a structure where the mean and amplitude of loading are non-constant it is more challenging to determine what portion(s) of the given load parameter correspond with a single cycle of loading. This loading parameter can be any parameter of interest such as but not limited to acceleration, deflection, force, strain, stress, or torque.

Cycle counting methods do not consider the effect of the loading sequence when converting a given loading parameter into an equivalent cyclic history for the same

parameter. For many high-cycle fatigue applications, the loading sequence does not significantly affect the prediction of damage accumulation from a fatigue damage model instead of a fatigue crack growth model [158]. For the case of variable amplitude fatigue, it has been established that the order of loading has an effect on the crack growth prediction due to the changes in the plastic zone size caused by variable amplitude fatigue, however, including the plasticity in the evaluation of the stress intensity factors has little difference from the LEFM solution [37, 38, 159].

There are many methods available to attempt to convert a loading history into a cyclic history such as level crossing cycle counting, peak-valley cycle counting, range counting, range-pair method, and rainflow cycle counting method [160-165]. Of these methods, the focus here will be upon the use of the rainflow counting method where stress is the loading parameter of interest. To this end, the MATLAB[®] code *rainflow* by Nieslony [166, 167] which follows ASTM E 1049, Standard Practices for Cycle Counting in Fatigue Analysis is used to convert a given stress history into a series of cyclic loads.

For the case of non-proportional multi-axial stress histories the common practice is to first convert the multi-axial stress components (e.g. σ_{xx} , σ_{yy} , and σ_{xy} for two-dimensional stress) into a single equivalent stress σ_{eq} . In order to convert the multi-axial stress components into a single equivalent stress there are methods based upon approaches such as the critical plane method [158, 159, 168-170] or the Wang-Brown method [171, 172]. This equivalent stress is then used in coordination with some fatigue damage model such as

$$D_i = \frac{n_i}{N_{f_i}} \quad \text{for } i = 1, \dots, k \quad 4-43$$

where D_i is the amount of damage at cycle i , n_i is the number of cycles for a given applied load, k is the total number of loading cycles, and N_{f_i} is the number of cycles to failure at the same applied load. The cumulative damage C_i at cycle i is given as

$$C_i = \sum_{j=1}^i D_j \quad \text{for } i = 1, \dots, k. \quad 4-44$$

It is commonly assumed that once $C_i = 1$, a given structure is fully damaged, can no longer carry load, and has failed [15]. The fatigue damage model approach serves as the basis for the identification of cycles from multi-axial stress data.

For a two dimensional analysis, the equivalent biaxial stress [173] for use in a fatigue damage model can be calculated from

$$\sigma_{eq}^2 = \sigma_{xx}^2 + \sigma_{yy}^2 - \sigma_{xx}\sigma_{yy} + 3\sigma_{xy}^2. \quad 4-45$$

This equivalent stress can be used to identify the equivalent cyclic loading history. In effect, for a fatigue damage model, once the equivalent stress σ_{eq} has been calculated, the bi-axial stress components (e.g. σ_{xx} , σ_{yy} , and σ_{xy}) can be discarded as they will no longer be used. This is not the case here as the biaxial stresses are directly applied.

For variable amplitude fatigue, the interaction of the biaxial stresses will affect the magnitude and direction of crack growth and should be applied directly to a cracked plate. If a rainflow counting approach is applied to the individual stress components, it is likely that each component will have a different number of cycles. The biaxial stress components will be applied to a cracked plate in order to calculate K_I and K_{II} . Before the fatigue crack growth model can be directly applied, the stress history is converted into an equivalent cyclic stress history. First, the equivalent biaxial stress is calculated

by Eq. 4-45. These cycles will then be superimposed upon the individual stress components. This approach is detailed in Figure 4-8 where the conversion of the biaxial stresses to an equivalent stress, the rainflow counting of that equivalent stress, and the superposition of that equivalent stress onto the individual stress components is shown.

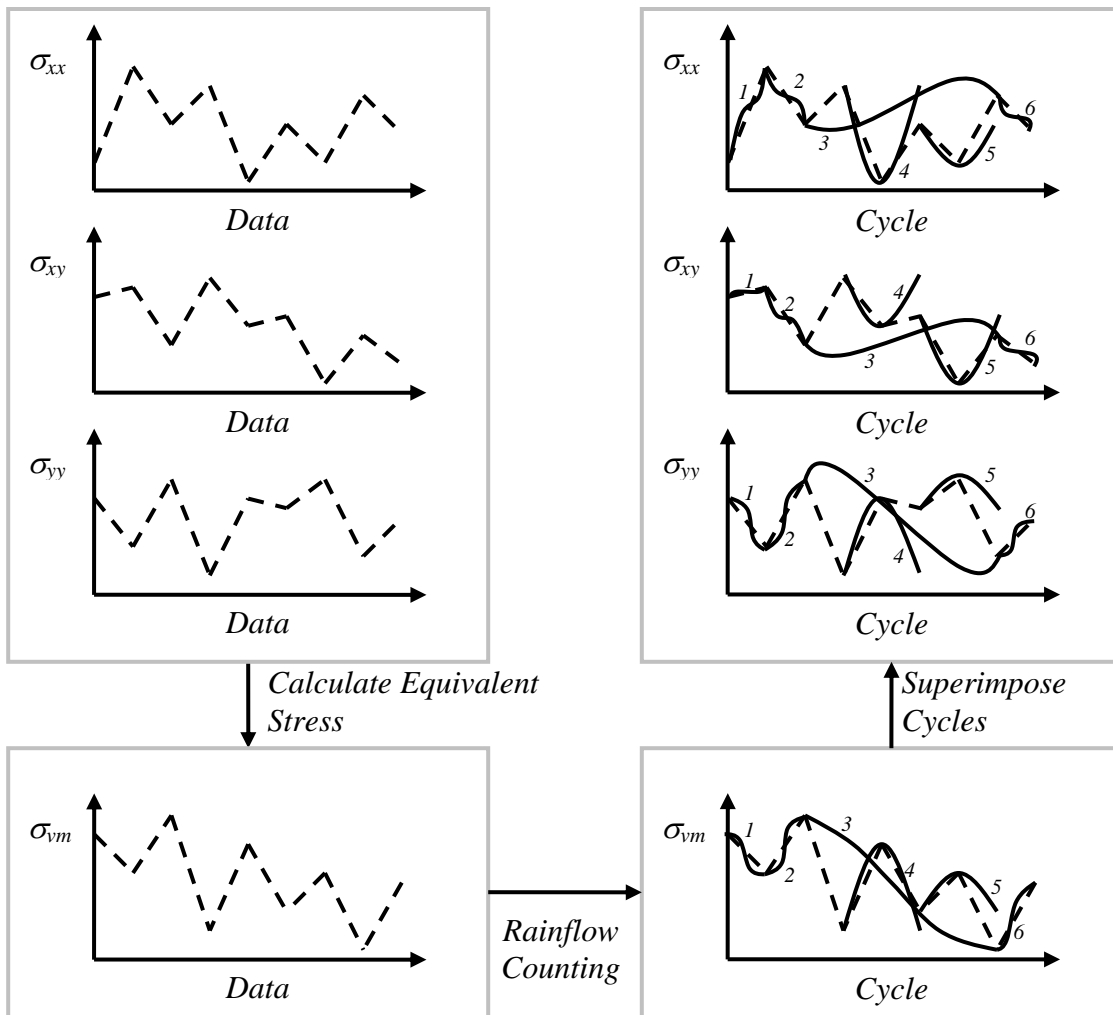


Figure 4-8. The strategy used to convert the bi-axial stress data into cyclic stress data which was suitable for use in a fatigue crack growth model.

An unexpected result of this procedure was that the ratio of σ_{xx} , σ_{xy} , and σ_{yy} are typically different at the peak and valley of a given cycle. This creates a need for two function evaluations, one at the maximum equivalent stress and one at the minimum equivalent stress for a particular loading cycle, to be conducted in order for the stress

intensity factor range to be calculated. It should be noted that while the individual stress components are being applied instead of the equivalent stress directly, the same cycles are being followed which were identified according to the equivalent stress.

Summary

Crack growth is modeled using mixed-mode stress intensity factors which are extracted from XFEM analysis with the use of the domain form of the contour integrals. Four models are given for the direction of crack growth based upon the mixed-mode stress intensity factors. The most popular of these models in the computational fracture mechanics community is the maximum circumferential stress criterion. For cases where shear may be a significant source of failure the Liu model may provide a better match to experimental data.

Two of the many fatigue crack growth models are introduced, the classical Paris model and a modified Paris model which has additional parameters to consider the effects of the stress ratio R , threshold stress intensity factor ΔK_{th} , and changes in the crack growth rate caused by the evolution of the plastic zone ahead of the crack tip under variable amplitude loading. Four models are presented for the calculation of an equivalent stress intensity factor range from the mixed-mode stress intensity factors. The model proposed by Liu will be used here based upon its superior performance when compared to a range of experimental data for failure caused by shear and tension.

The challenges with solution of a fatigue crack growth model were highlighted by an example of fatigue crack growth in a plate with an edge crack and a hole. The effects

of mesh density, crack growth increment, and the elapsed number of cycles were considered with respect to the convergence of the crack propagation path.

Finally, the rainflow counting method was introduced for the conversion of stress histories into equivalent cycles. As these models are usually used for fatigue damage prediction instead of direct fatigue crack growth modeling, the steps which are used in the identification of cyclic stress histories for the biaxial stresses is detailed. First, the equivalent biaxial stress is calculated. Cycles for the equivalent biaxial stress are calculated according to the rainflow counting method. These cycles are then superimposed upon the biaxial stresses, allowing for the biaxial stress components to be applied directly for the analysis of a cracked plate subjected to variable amplitude biaxial loading.

CHAPTER 5
SURROGATE MODELS FOR HIGHER-ORDER INTEGRATION OF FATIGUE CRACK
GROWTH MODELS

Integration of Ordinary Differential Equation

The objective of this chapter is to use a surrogate model to reduce the number of expensive function evaluations needed in the numerical integration of an ordinary differential equation which follows the general form

$$\frac{dy}{dx} = f(x, y). \quad 5-1$$

For an unknown function $f(x,y)$ a common method to approximate the solution is to discretize $f(x,y)$ into discrete points, where $f(x,y)$ is approximated using some numerical technique. In this work, finite element simulations are used to approximate $f(x,y)$. There are numerous methods available to approximate the solution to Eq. 5-1 at some y_{i+1} from some current state y_i , such as the forward Euler approximation which is

$$y_{i+1} = y_i + hf(x_i, y_i) \quad 5-2$$

where h is the integration step size given as $x_{i+1}-x_i$ or the midpoint approximation as

$$y_{i+1} = y_i + hf\left(x_{i+1/2}, y_i + \frac{h}{2}f(x_i, y_i)\right). \quad 5-3$$

The midpoint approximation allows for larger step sizes h to be taken compared to the forward Euler approximation for the same integration accuracy. However, this requires two function evaluations, one at x_i and another at $x_{i+1/2}$, which is one more than the forward Euler approximation requires.

For many engineering problems, no analytical equation is available for the right-hand-side given as $f(x, y)$. In some of these cases $f(x, y)$ can be approximated at

discrete (x, y) locations through the use of finite element analysis simulations.

However, these simulations can be expensive, especially for complex geometries. In the case of fatigue crack growth, the number of analysis needed further increases the cost of the finite element simulations needed to approximate $f(x, y)$. In this chapter, two cases with various amounts of knowledge about $f(x, y)$ are considered. First, the case where a history of discrete function evaluations is available is considered. A surrogate model is then fit to the discrete function evaluations and is used to interpolate the values of $f(x, y)$ required by the midpoint approximation, replacing finite element simulations at these points. Second, the case where only the discrete points up to (x_i, y_i) are available is considered. These two cases are shown in Figure 5-1 where (x_f, y_f) is some final value of (x, y) which ends a given analysis. A surrogate model is fit to the available data points and is used to extrapolate to y_{i+1} , replacing an expensive finite element simulation at that point. The methods introduced allow for the benefits of the midpoint approximation to be realized with the number of function evaluations needed for the forward Euler approximation.

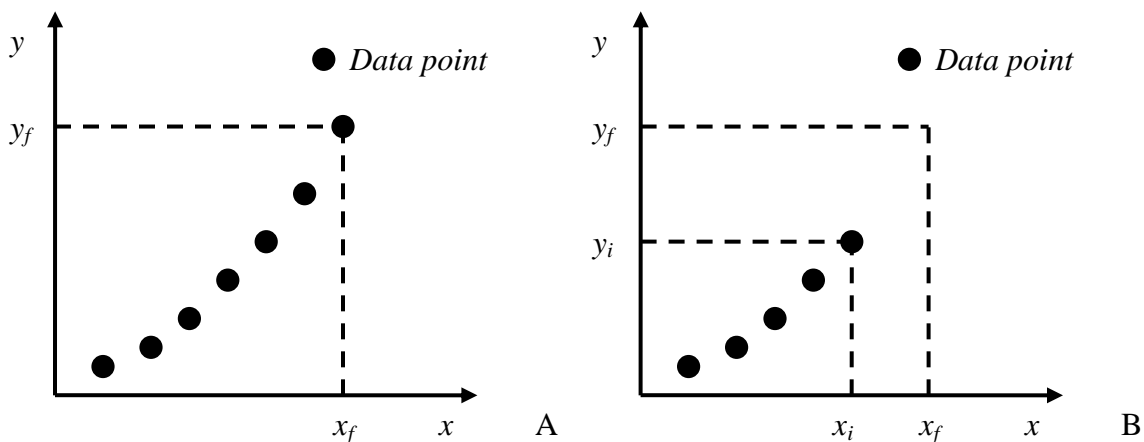


Figure 5-1. Available discrete points available which can be fit using a surrogate model. A) Complete history is available to (x_f, y_f) , B) History is available to (x_i, y_i) .

Surrogate Models

Surrogate models are commonly used to reduce the cost associated with the evaluation of expensive functions. Types of surrogate models include polynomial response surface [174], kriging [175-177], radial basis neural networks [178], and support vector regression [179]. Kriging is used here instead of other surrogate models based on an initial trial of various surrogate models. The results of these tests showed that all surrogates besides kriging would require additional tuning before they would provide acceptable accuracy, while kriging simply worked. While the results here were generated with kriging, the methods presented here should be applicable to any surrogate model which provides sufficient accuracy for interpolation and extrapolation.

Here three cases are considered, one for the case in Figure 5-1 where a complete history of discrete points is available and two where only the history up to some (x_i, y_i) is available. First, the approach of fitting surrogate models to the stress intensity factor and crack growth direction history is tested based on a fixed increment of crack growth Δa or a fixed number of elapsed cycles ΔN for a given crack geometry. When a fixed Δa is used, the relationship between ΔK and Δa is fit using a kriging surrogate. This surrogate is then used to approximate the corresponding cycle number N for a given crack size a such that the cyclic crack growth history can be obtained. Correspondingly, when a fixed ΔN is used, the relationship between ΔK and ΔN is fit using a kriging surrogate. This surrogate is then used to extrapolate forward in the cycle history so that a higher-order approximation to the chosen fatigue crack growth law can be used to find the corresponding Δa . Second, a variable integration step size algorithm is introduced for the automatic generation of a step size ΔN based on the accuracy in the surrogate

extrapolation of ΔK and the crack growth direction. This is an attempt to only perform expensive function evaluations when needed. These two cases are shown in Figure 5-2 where ΔK_c is the critical stress intensity factor range, a_c is the corresponding critical crack size, ΔK_i is the stress intensity factor range corresponding to the crack size at cycle N_i . Third, the case of mixed-mode crack growth is considered and the use of a surrogate model is introduced which enables the use of a higher-order approximation to the crack growth direction which would otherwise not be available.

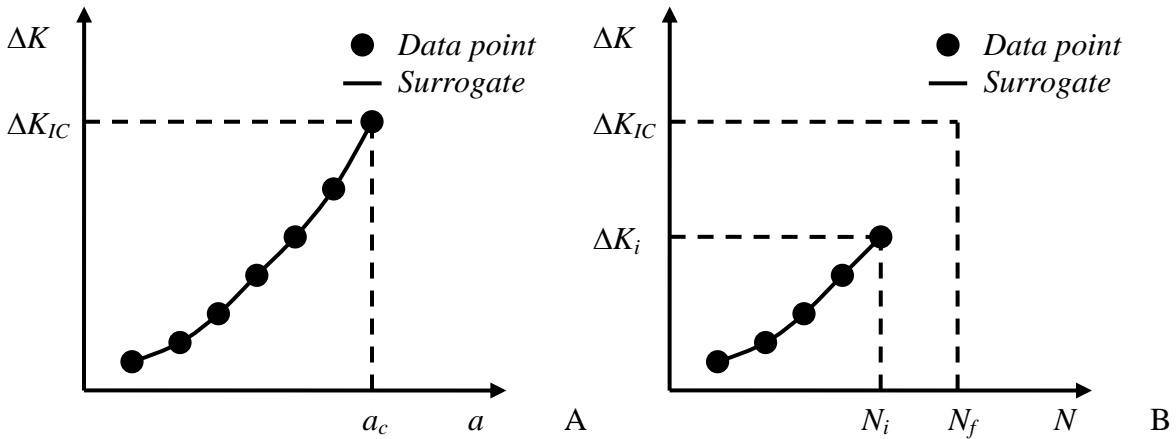


Figure 5-2. Surrogate model fit to either a complete or partial crack growth history. A) Complete history, surrogate for a - ΔK , B) Partial history, surrogate for N - ΔK .

Kriging

Kriging [175-177] can be used to represent a function of interest $y(\mathbf{x})$. As this function is expensive to evaluate, it may be approximated by a cheaper model $\hat{y}(\mathbf{x})$ based on assumptions on the nature of $y(\mathbf{x})$ and on the observed values of $y(\mathbf{x})$ at a set of data points called an experimental design. More explicitly,

$$y(\mathbf{x}) = \hat{y}(\mathbf{x}) + \varepsilon(\mathbf{x}), \quad 5-4$$

where $\mathbf{x} = [x_1, \dots, x_d]^T$ is a real d -dimensional vector and $\varepsilon(\mathbf{x})$ represents both the error of approximation and random errors.

Kriging estimates the value of the unknown function $y(\mathbf{x})$ as a combination of basis functions $f_i(\mathbf{x})$ such as a polynomial basis and departures by

$$\hat{y}(\mathbf{x}) = \sum_{i=1}^m \beta_i f_i(\mathbf{x}) + z(\mathbf{x}), \quad 5-5$$

where $z(\mathbf{x})$ satisfies $z(\mathbf{x}_k) = y(\mathbf{x}_k) - \sum_{i=1}^m \beta_i f_i(\mathbf{x}_k)$ for all sample points (\mathbf{x}_k) and is

assumed to be a realization of a stochastic process $Z(\mathbf{x})$ with mean zero,

$$\text{cov}(Z(\mathbf{x}_i), Z(\mathbf{x}_j)) = \sigma^2 R(\mathbf{x}_i, \mathbf{x}_j), \quad 5-6$$

and process variance σ^2 , and spatial covariance function given by

$$\sigma^2 = \frac{1}{p} (\mathbf{y} - \mathbf{X}\mathbf{b})^T \mathbf{R}^{-1} (\mathbf{y} - \mathbf{X}\mathbf{b}), \quad 5-7$$

where $R(\mathbf{x}_i, \mathbf{x}_j)$ is the correlation between $Z(\mathbf{x}_i)$ and $Z(\mathbf{x}_j)$, \mathbf{y} is the value of the actual responses at the sampled points, \mathbf{X} is the Gramian design matrix constructed using the basis functions at the sampled points, \mathbf{R} is the matrix of correlations $R(\mathbf{x}_i, \mathbf{x}_j)$ among sample points, and \mathbf{b} is an approximation of the vector of coefficients β_i of Eq. 5-5. Figure 5-3 shows the prediction and the error estimates of kriging. It can be noticed that since the kriging model is an interpolator, the error vanishes at sampled data points. It may be possible to use the variance provided by kriging as a means to assess its accuracy or to find an appropriate integration step size. Since many surrogate models do not provide an estimate of the variance, this approach has not been used. The goal was to create a general algorithm applicable to any surrogate model.

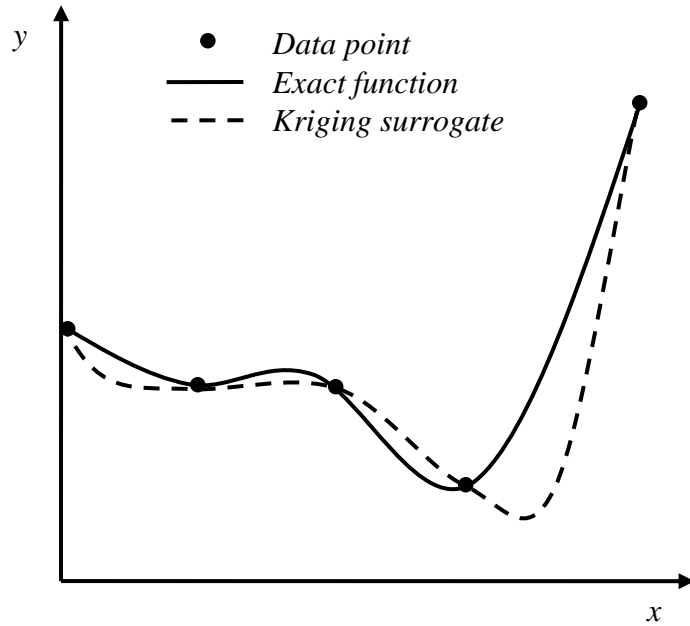


Figure 5-3. Comparison of an exact function and the corresponding kriging surrogate model for an arbitrary set of five data points.

Kriging for Integration of Fatigue Crack Growth Law

Constant Integration Step Size

The limitation on the types of methods which can be used in the direct integration of a fatigue model comes from the need to evaluate the stress intensity factor at some future crack tip position. The idea presented here is to use a surrogate model to fit the available stress intensity factor history and to replace some of the expensive finite element simulations with inexpensive function evaluations using the surrogate model. Two cases are considered: one in which there is a constant magnitude of crack growth Δa at each integration step, another where a constant number of elapsed cycles ΔN occurs for each integration step.

For the case of a fixed Δa , ΔN is calculated *a posteriori* to the function evaluations using either an Euler approximation as

$$\Delta N = \frac{\Delta a}{C(\Delta K(a_i))^m} \quad 5-8$$

or a midpoint approximation as

$$\Delta N = \frac{\Delta a}{C\left(\Delta K\left(a_i + \frac{\Delta a}{2}\right)\right)^m}. \quad 5-9$$

With a traditional approach the function evaluation $\Delta K(a_i + \Delta a/2)$ has not yet been completed and would require an additional expensive function evaluation. Through the use of surrogate models this extra function evaluation at $\Delta K(a_i + \Delta a/2)$ can be avoided by fitting a surrogate model to the $a - \Delta K$ history. The extra needed function evaluation can then be approximated using interpolation. Four initial data points are provided before the use of kriging. To get the three additional data points, the forward Euler method can be used with a small integration step size (e.g. $\Delta N = 1$) which has sufficient accuracy away from the critical crack length.

When a constant number of elapsed cycles ΔN is considered the corresponding amount of crack growth Δa for a given ΔN can be calculated using the forward Euler approximation as

$$\Delta a = \Delta N C (\Delta K(a_i))^m \quad 5-10$$

or the midpoint approximation as

$$\Delta a = \Delta N C \left(\Delta K \left(a_i + \frac{\Delta N}{2} C (\Delta K(a_i))^m \right) \right)^m. \quad 5-11$$

In Eq. 5-11, note that there are two expensive function evaluations, one for $\Delta K(a_i)$ and the other at the approximated value for $\Delta K(a_{i+1/2}) = \Delta K\left(a_i + 0.5\Delta N C (\Delta K(a_i))^m\right)$. The use

of surrogate models allows for only one expensive function evaluation to be required at $\Delta K(a_i)$. A surrogate model is fit to the $N - \Delta K$ history up to and including $\Delta K(a_i)$. The surrogate model is then used to extrapolate to $\Delta K(a_{i+1/2})$, replacing an expensive finite element simulation as shown in Figure 5-4.

For problems with mixed mode loading, two kriging surrogates are used. First, a surrogate is used to approximate the response of ΔK as a function of either the crack length a or the number of elapsed cycles N . The surrogate approximation is then used for a higher-order approximation to Paris model, such as the midpoint method given by Eqs. 5-9 and 5-11. Second, a surrogate is fit to the history for the history of crack growth direction θ in the global coordinate system. The same extrapolation and interpolation strategy using the surrogate model is used to enable higher-order approximations for the crack growth direction.

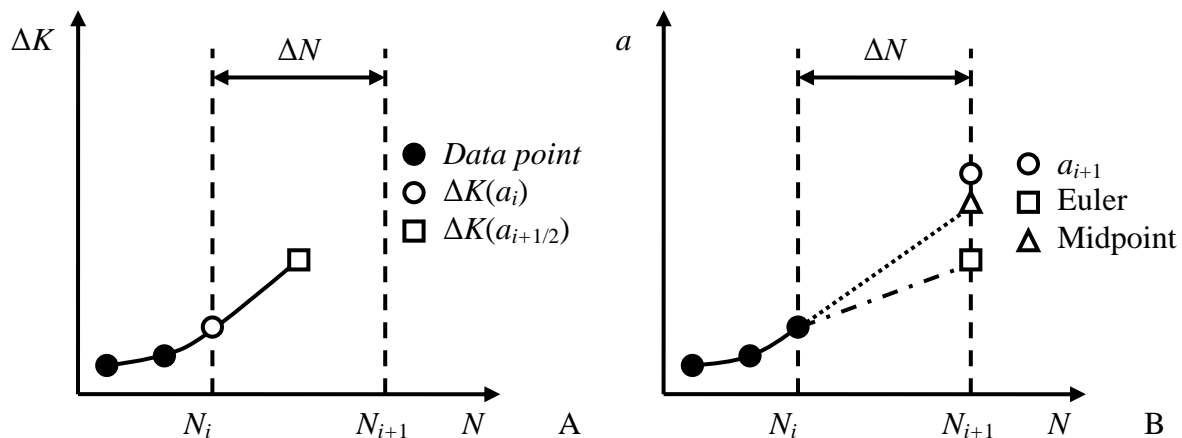


Figure 5-4. Integration of fatigue crack growth model from N_i to N_{i+1} using either Euler or midpoint approximation. A) Function evaluations needed for Euler and midpoint approximations, B) Accuracy of crack size calculation at N_{i+1} .

Variable Integration Step Size

There are numerical methods which will automatically adjust the integration step size to some allowable error [23]. However, these methods typically use function

evaluations to estimate the error associated with a given step size before choosing upon a step size to use. In the finite element framework, this algorithm would result in needless expensive function evaluations in order to determine the allowable step size. To avoid these additional function evaluations, an algorithm is presented which allows for the step size to be dynamically changed based on the accuracy of the surrogate extrapolation as shown in Figure 5-5. This algorithm should be useful for any surrogate model. For the case of adjusting the step size based on the prior accuracy, the $i+1^{\text{th}}$ step size can be found from the solution for the i^{th} crack geometry as

$$\Delta N_{i+1} = \Delta N_i \min \left[\left(\frac{e_t^K}{1 - \Delta K_{i+1}^{SUR} / \Delta K_{i+1}^{NUM}} \right)^{\alpha_k}, \left(\frac{e_t^\theta}{|1 - \theta_{i+1}^{SUR} / \theta_{i+1}^{NUM}|} \right)^{\alpha_t} \right] \quad 5-12$$

where ΔN_i is the current step size, e_t is the target allowable error in percent difference between the surrogate extrapolation and XFEM values at $i+1$, α is an exponent which determines how quickly the step size changes, and ΔK_{i+1} and θ_{i+1} are evaluated based on $i+1$ for the current crack geometry using either a numerical (e.g. XFEM) or surrogate (e.g. kriging) model. The step size is scaled based on the accuracy of the predicted value. For the case where either $\Delta K_{i+1}^{SUR} = \Delta K_{i+1}^{NUM}$ or $\theta_{i+1}^{SUR} = \theta_{i+1}^{NUM}$, then $\Delta N_{i+1} = 2\Delta N_i$.

The values of e_t^K and e_t^θ in Eq. 5-12 were found to be 0.001, while α_t and α_k were defined to be 0.1 based on a parameter study where a range of materials with unique C and m values and a variety of different initial crack sizes were used in the calibration of the variable integration step size algorithm. When the error shown in Figure 5-5 is greater than the target error, the integration step size is decreased. Similarly, when the error is smaller than the target error, the integration step size is increased.

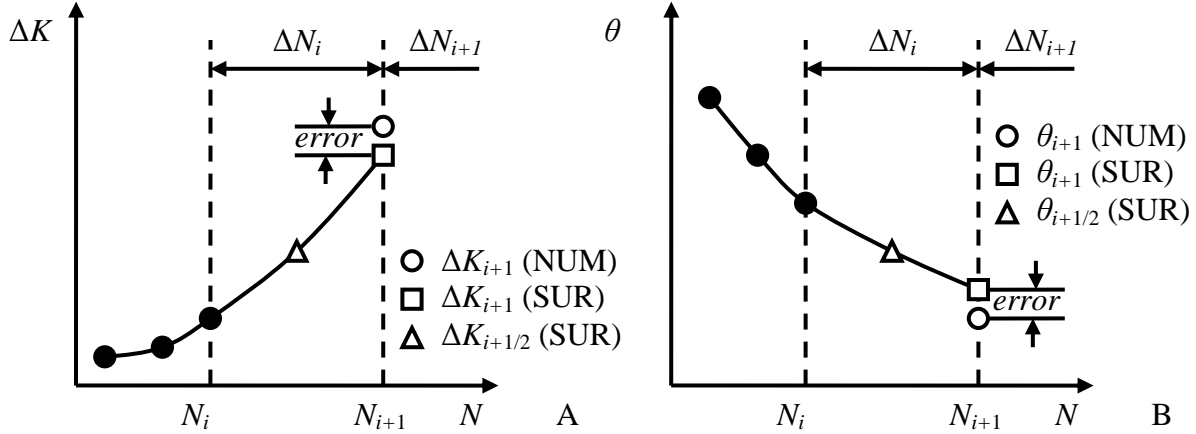


Figure 5-5. Errors used to adjust the adaptive integration step size algorithm. A) Error used to adjust integration step size according to stress intensity factor surrogate, B) Error used to adjust integration step size according to crack growth direction surrogate.

A summary of this approach follows. A series of XFEM simulations were performed to evaluate ΔK^{NUM} as a function of the crack size a . In addition, the angle of crack growth given in terms of the global coordinate system θ^{NUM} was evaluated as a function of crack size. Once these easily evaluated functions were available, the crack growth was simulated such that:

1. For crack geometry i , fit surrogate for history of ΔK^{NUM} and θ^{NUM} , evaluate ΔK^{SUR} and θ^{SUR} at $i+1/2$ and $i+1$.
2. Calculate the crack growth increment Δa from $\Delta a = \Delta N_i C (\Delta K_{i+1/2}^{SUR})^m$.
3. Calculate the crack growth increments in the x and y -directions from $\Delta x = \Delta a \cos(\theta_{i+1/2}^{SUR})$ and $\Delta y = \Delta a \sin(\theta_{i+1/2}^{SUR})$.
4. Update the crack tip location based on Δx and Δy , evaluate ΔK_{i+1}^{NUM} and θ_{i+1}^{NUM} .
5. Find the next step size from Eq. 5-12, repeat for next crack geometry. It is noted that the current dynamic step size determination scheme is not recovering the error at step $i+1$.

Example Problems

First a center crack in an infinite plate under uniaxial tension is considered. This case is convenient as it has a closed form solution for the crack size and stress intensity factor as a function of applied stress, loading cycle, and material properties. This allows for an estimate of the amount of error that can be expected by the use of kriging to provide data points instead of performing a function evaluation. The effect on the choice of a fixed Δa or ΔN is considered for the theoretical model of a center crack in an infinite plate to show the validity of the approach. The presented variable step size algorithm is also used for each example problem. Results are presented for each case as the final approximate value normalized by the exact final value of crack size or cycle number. A value of one denotes perfect agreement with the exact solution.

The tested materials and the corresponding material properties are aluminum 2024 at stress ratios of 0.1 ($C = 1.60 \cdot 10^{-11}$, $m = 3.59$, $K_{IC} = 30 \text{ MPa}\sqrt{m}$) and 0.5 ($C = 3.15 \cdot 10^{-11}$, $m = 3.59$, $K_{IC} = 30 \text{ MPa}\sqrt{m}$) as well as austenitic ($C = 1.36 \cdot 10^{-10}$, $m = 2.25$, $K_{IC} = 50 \text{ MPa}\sqrt{m}$) and martensitic ($C = 5.60 \cdot 10^{-12}$, $m = 3.25$, $K_{IC} = 50 \text{ MPa}\sqrt{m}$) steel [156]. The results are presented for each case as a function of the ratio between the theoretical solution and the calculated solution for either crack size or cycle number such that a value of one denotes no difference between the calculated and theoretical solutions. A value of 0.98 or 1.02 represents a 2 percent error in the calculated value.

Center Crack in an Infinite Plate Under Tension

First, a center crack in an infinite plate with initial crack length of 10 mm is considered. For the case of a center crack in an infinite plate under uniaxial tension of 78.6 MPa, the Mode I stress intensity factor [20, 180] is

$$K_I = \sigma\sqrt{\pi a} \quad 5-13$$

where σ is the applied stress, and a is the half crack length. By substituting Eq. 5-13 into Eq. 4-21 for Paris model and rearranging terms, the number of cycles for a crack to grow can be calculated using the following integration:

$$N = \int_{a_i}^{a_N} \frac{da}{C(\sigma\sqrt{\pi a})^m} = \left[\frac{a_N^{\frac{2-m}{2}} - a_i^{\frac{2-m}{2}}}{C\left(\frac{2-m}{2}\right)(\sigma\sqrt{\pi})^m} \right] \quad 5-14$$

where a_i is the initial crack size. Rearranging Eq. 5-14, the crack size a_N after N cycles can be calculated by

$$a_N = \left[NC\left(1 - \frac{m}{2}\right)(\sigma\sqrt{\pi})^m + a_i^{\frac{2-m}{2}} \right]^{\frac{2}{2-m}}. \quad 5-15$$

This allows for the midpoint method to be applied as a_N and K_I can be directly evaluated and used in the integration of Paris model at any cycle number. For a geometry without known relationship between ΔK and a a finite element solution would need to be performed at N_i at which time an Euler approximation could be used to approximate a_{i+1} , allowing a second finite element simulation to be performed and the midpoint method to be applied.

An aluminum 2024 plate with a stress ratio of 0.5 is chosen to validate the use of kriging extrapolation for the integration of the fatigue crack growth model. The critical stress intensity factor is reached for a crack size of 50 mm given an initial crack size of 10 mm in about 22,300 cycles. For a fixed Δa , the results are given in Table 5-1 where the data is presented as normalized values of the cycle at which the crack length is 50 mm. The kriging surrogate is used to calculate cycle number N for each discrete crack

length a as a post-processing operation. Comparing the midpoint approximation to the kriging midpoint approximation provides an indication in the amount of error introduced by using kriging to replace the additional function evaluation needed for the midpoint approximation. Thus, all kriging evaluations are based on interpolation. Recall that the common Δa used in the literature is $a_i/10$. For that crack growth increment, the Euler approximation has over 5 percent error. Through the use of the midpoint approximation, the error is reduced to less than 1 percent. Larger crack growth increments for the Euler method lead to very large errors, which can be drastically reduced through the use of the midpoint approximation. As interpolation is being used here it would also be possible to apply other higher-order approximations such as the Runge-Kutta method [23] for the back-calculation of elapsed cycles for a fixed Δa .

Table 5-1. Accuracy of kriging interpolation integration for fixed increment Δa for a center crack in an infinite plate of Al 2024 with $R = 0.5$. The number of function evaluations is denoted as FE.

Δa	Normalized $N(a = 50 \text{ mm})$					
	Euler	Euler FE	Midpoint	Midpoint FE	Kriging Midpoint	Kriging FE
$a_i/160$	1.00	640	1.00	1280	1.00	640
$a_i/80$	1.01	320	1.00	640	1.00	320
$a_i/40$	1.01	160	1.00	320	1.00	160
$a_i/20$	1.03	80	1.00	160	1.00	80
$a_i/10$	1.05	40	0.999	80	0.999	40
$a_i/5$	1.11	20	0.997	40	0.997	20
$a_i/2$	1.30	8	0.981	16	0.981	8
a_i	1.66	4	0.935	8	0.944	4

For a fixed ΔN , the results are given in Table 5-2 where the data is presented as normalized values of the crack length at cycle number 23,000. The kriging surrogate is used to extrapolate a stress intensity factor range allowing the midpoint method to be applied. The first observation from Table 5-2 is that the accuracy of Euler approximations is much more sensitive to changes in fixed ΔN when compared to a

fixed Δa . For this problem, the function evaluations are equal for each approach, in general midpoint would be twice as expensive as Euler or the kriging midpoint. However, the midpoint approximations are largely insensitive to the chosen crack growth increment. There is some loss of accuracy associated with the use of the midpoint approximation method when compared to the exact midpoint approximation. It should be noted that the kriging surrogate produced improved accuracy when compared to the midpoint approximation method. The kriging assisted midpoint method offers improved accuracy to the midpoint approximation method with less function evaluations.

Table 5-2. Accuracy of kriging extrapolation integration for fixed increment ΔN for a center crack in an infinite plate of Al 2024 with $R = 0.5$. The number of function evaluations is denoted as FE.

ΔN	Normalized $a(N = 23,000)$					
	Euler	Euler FE	Midpoint	Midpoint FE	Kriging Midpoint	Kriging FE
1	1.00	23,000	1.00	46,000	1.00	23,000
25	0.995	920	1.00	1,840	1.00	920
50	0.990	460	1.00	920	1.00	460
100	0.981	230	0.999	460	1.00	230
500	0.918	46	0.997	92	0.999	46
1000	0.856	23	0.989	46	0.995	23

To assess the applicability of the variable step size algorithm to a range of fatigue problems four different materials were chosen along with initial crack sizes of either 1 or 10 mm and grown to failure at 50 mm. As with the fixed step size approach, three data points are found using the forward Euler approach with $\Delta N = 1$ before the variable step size algorithm begins. The results for the materials and crack sizes is given in Table 5-3 where a comparison between the cycle where failure occurs based on the Euler N_{fail}^{euler} and kriging extrapolation N_{fail}^{KRG} methods with the number of function evaluations.

Note that the number of function evaluations for the Euler method is the same as N_{fail}^{euler} . It can be noted from the above table that the number of function evaluations that

the algorithm uses to model the crack growth to failure is generally independent of the number of cycles to failure. The general trend of the variable step size algorithm is that initially there are smaller steps, then the step size increases. When the crack approaches the critical crack size, the integration step size decreases ensuring an accurate solution. This behavior is shown in Figure 5-7, and while the problem being solved is different the trend of the integration step size curve is the same.

Table 5-3. Effect of material and initial crack size on estimated cycles to failure for the variable step size algorithm for a center crack in an infinite plate.

Material	a_i	N_{fail}^{theo}	N_{fail}^{KRG}	Kriging FunEval	Norm N_{fail}
Aluminum, $R = 0.1$	1	365,740	370,292	52	1.01
Aluminum, $R = 0.1$	10	44,301	44,358	49	1.00
Aluminum, $R = 0.5$	1	185,773	184,286	46	0.992
Aluminum, $R = 0.5$	10	22,502	23,121	50	1.02
Aust. Steel	1	808,426	813,819	61	1.01
Aust. Steel	10	285,645	292,556	55	1.02
Mart. Steel	1	2,103,878	2,085,640	67	0.991
Mart. Steel	10	346,500	347,733	55	1.00

Edge Crack in a Finite Plate Under Tension

For the case of an edge crack in a finite plate under uniaxial tension of 78.6 MPa the Mode I stress intensity factor [180, 181] is

$$K_I = \left[1.12 - 0.281 \frac{a}{W} + 10.55 \left(\frac{a}{W} \right)^2 - 21.72 \left(\frac{a}{W} \right)^3 + 30.39 \left(\frac{a}{W} \right)^4 \right] \sigma \sqrt{\pi a} \quad 5-16$$

where a is the crack length and W is the plate width. The plate width for this problem was $W = 0.2$ m. As there is no analytical expression for a_N , the crack length after 10,700 cycles was found to be 30 mm using the forward Euler method where the step size was reduced until convergence in crack size at 10,700 cycles was achieved.

For a fixed step size, aluminum 2024 with a stress ratio of 0.5 is chosen to validate the use of kriging extrapolation for the integration of the fatigue crack growth model with

a constant step size. The critical stress intensity factor is reached for a crack size of 50 mm given an initial crack size of 10 mm in about 11,000 cycles. For a fixed Δa , the results are given in Table 5-4 as normalized values of the cycle at which the crack length is 50 mm. The same number of function evaluations is shared by all integration methods. The kriging surrogate is used to calculate cycle number N for each discrete crack length a as a post-processing operation. Thus, all kriging evaluations are based on interpolation. The midpoint method was used here by evaluating Eq. 5-16 for any crack size a . This gives an error estimate for kriging interpolation. Here for a fixed crack growth increment of $a_i/10$ the corresponding Euler approximation has an error of 7 percent, while the midpoint approximation yields less than 1 percent error.

Table 5-4. Accuracy of kriging interpolation integration for fixed increment Δa for an edge crack in a finite plate of Al 2024 with $R = 0.5$. The number of function evaluations is denoted as FE.

Δa	Normalized $N(a = 50 \text{ mm})$					
	Euler	Euler FE	Midpoint	Midpoint FE	Kriging Midpoint	Kriging FE
$a_i/160$	1.00	640	0.996	1280	0.996	640
$a_i/80$	1.00	320	0.996	640	0.996	320
$a_i/40$	1.01	160	0.996	320	0.996	160
$a_i/20$	1.03	80	0.995	160	0.996	80
$a_i/10$	1.07	40	0.995	80	0.994	40
$a_i/5$	1.14	20	0.991	40	0.991	20
$a_i/2$	1.39	8	0.969	16	0.973	8
a_i	1.88	4	0.905	8	0.944	4

For a fixed elapsed number of cycles in each function evaluation, the exact results for the midpoint method are not available as there is no explicit value for a_N . From Table 5-5 where data is presented as normalized values of the crack length at cycle number 11,000 it is apparent that once again, the kriging assisted midpoint method allows for larger step sized compared to the forward Euler method. The number of function evaluations is equal for Euler and kriging integration. The kriging surrogate is

used to extrapolate a stress intensity factor range allowing the midpoint method to be applied. The exact midpoint method may not be applied to this problem as no closed form solution for $a(N)$ is known to the authors for the stress intensity factor given by Eq. 5-16. In this case, for a step size of 100, the errors for the Euler and kriging assisted midpoint methods are 3.5 and 0.2 percent. The increased errors in the approximation compared to the case of a center crack in an infinite plate can most likely be explained by the increased nonlinearity caused by the edge and finite effects in this geometry.

Table 5-5. Accuracy of kriging extrapolation integration for fixed increment ΔN for an edge crack in a finite plate of Al 2024 with $R = 0.5$. The number of function evaluations is denoted as FE.

ΔN	Normalized $a(N = 11,000)$					
	Euler	Euler FE	Midpoint	Midpoint FE	Kriging Midpoint	Kriging FE
1	1.00	11,000	1.00	22,000	1.00	11,000
25	0.994	440	1.00	880	1.00	440
50	0.987	220	1.00	440	1.00	220
100	0.975	110	0.999	220	0.999	110
500	0.947	22	0.996	44	0.995	22
1000	0.877	11	0.984	22	0.978	11

The variable step size algorithm is again tested with a range of fatigue problems. Four different materials were chosen along with initial crack sizes of either 1 or 10 mm and grown to failure at 50 mm. As with the fixed step size approach, three data points are found using the forward Euler approach with $\Delta N = 1$ before the variable step size algorithm begins. The results for the materials and crack sizes are given in Table 5-6. A comparison between the cycle where failure occurs based on the Euler N_{fail}^{euler} and kriging extrapolation N_{fail}^{KRG} methods is given in addition to the number of required function evaluations. Note that the number of cycles to failure does not change the number of kriging function evaluations used by the variable integration algorithm.

Table 5-6. Effect of material and initial crack size on estimated cycles to failure for the variable step size algorithm for an edge crack in a finite plate.

Material	a_i	$N_{fail}^{euler, \Delta N=1}$	N_{fail}^{KRG}	Kriging FunEval	Norm N_{fail}
Aluminum, $R = 0.1$	1	235,374	240,401	42	1.02
Aluminum, $R = 0.1$	10	20,701	21,473	38	1.03
Aluminum, $R = 0.5$	1	119,557	122,705	44	1.03
Aluminum, $R = 0.5$	10	10,516	10,799	38	1.03
Aust. Steel	1	594,634	601,308	49	1.01
Aust. Steel	10	189,225	193,493	41	1.02
Mart. Steel	1	1,415,883	1,459,668	46	1.03
Mart. Steel	10	196,924	200,215	41	1.01

Inclined Center Crack in a Finite Plate Under Tension

The first test problem which also considers the effect of crack growth direction is that of an inclined center crack in a finite plate subjected to uniaxial tension in the y -direction as shown in Figure 5-6. The magnitude of the applied stress σ was material dependent to reduce the number of cycles to failure for the steel samples and therefore, the number of function evaluations for the forward Euler solution with step size $\Delta N = 1$. The plate was chosen to be a 2 m x 2 m plate with an initial half crack size of 0.187 m. The crack was grown by XFEM simulations on a structured mesh of element size $h = 0.05$ to a final half crack size of 0.6 m. The values of the constants in the variable step size algorithm were retained from the previous sections.

For the variable step size algorithm, different applied stresses were considered for different materials in order to reduce the number of XFEM simulations needed for the Euler method. The comparison of the number of cycles to failure and the final crack position for the Euler with constant $\Delta N = 1$ to the variable step size is presented in Table 5-7. Note that the cycle number corresponding to failure in each case is in excellent agreement with the reference Euler solution. For the case of austenitic steel, it should be noted that the larger difference between the number of cycles to failure and the final

coordinates of the crack tip can be explained by the last step simply occurring in a way which passed the true failure cycle.

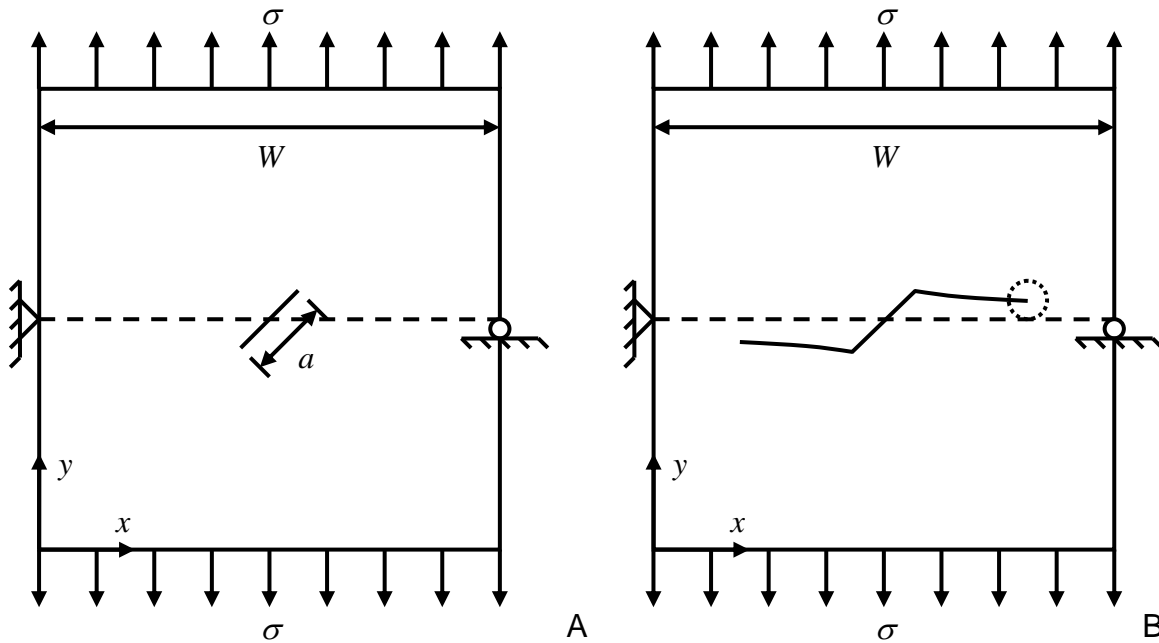


Figure 5-6. An inclined center crack in a square finite plate under uniaxial tension. A) Initial geometry, B) Final geometry.

Table 5-7. Comparison of Euler and variable step size predictions for the coordinates (x_{final} , y_{final}) of the right crack tip marked with a dotted circle in Figure 5-6 and cycle number N_{fail} corresponding to a final crack size of 0.6 m from an initial crack size of 0.187 m for four different materials.

Applied Stress	Material	$R = 0.1$	$R = 0.5$	Austenitic	Martensitic
	MPa	50	50	125	75
x_{fail}	Euler	1.5431	1.5432	1.5431	1.5431
	Variable	1.5432	1.5433	1.5450	1.5431
y_{fail}	Euler	1.0902	1.0902	1.0902	1.0902
	Variable	1.0902	1.0902	1.0900	1.0902
N_{fail}	Euler	29,519	14,996	68,331	80,597
	Variable	29,574	15,025	68,622	80,707
	FunEval ^{VAR}	356	157	52	245

The integration step size and percent errors as a function of cycle for two stress ratios of aluminum 2024 are given in Figure 5-7. It can be observed that for each material the agreement in final crack tip position and number of cycles to failure agrees very well to the Euler solution with small step size. Note that the integration step size

increases in Figure 5-7 until the target error is exceeded, at which point in time, the integration step size decreases to limit the amount of error introduced into the solution. This phenomenon can be noted as occurring for aluminum for $R = 0.1$ around cycle number 11,000 where the integration step size begins to decrease. Also for aluminum at stress ratio $R = 0.5$ the reduction in integration step size occurs twice, first around cycle number 4,000 and second around cycle number 10,000.

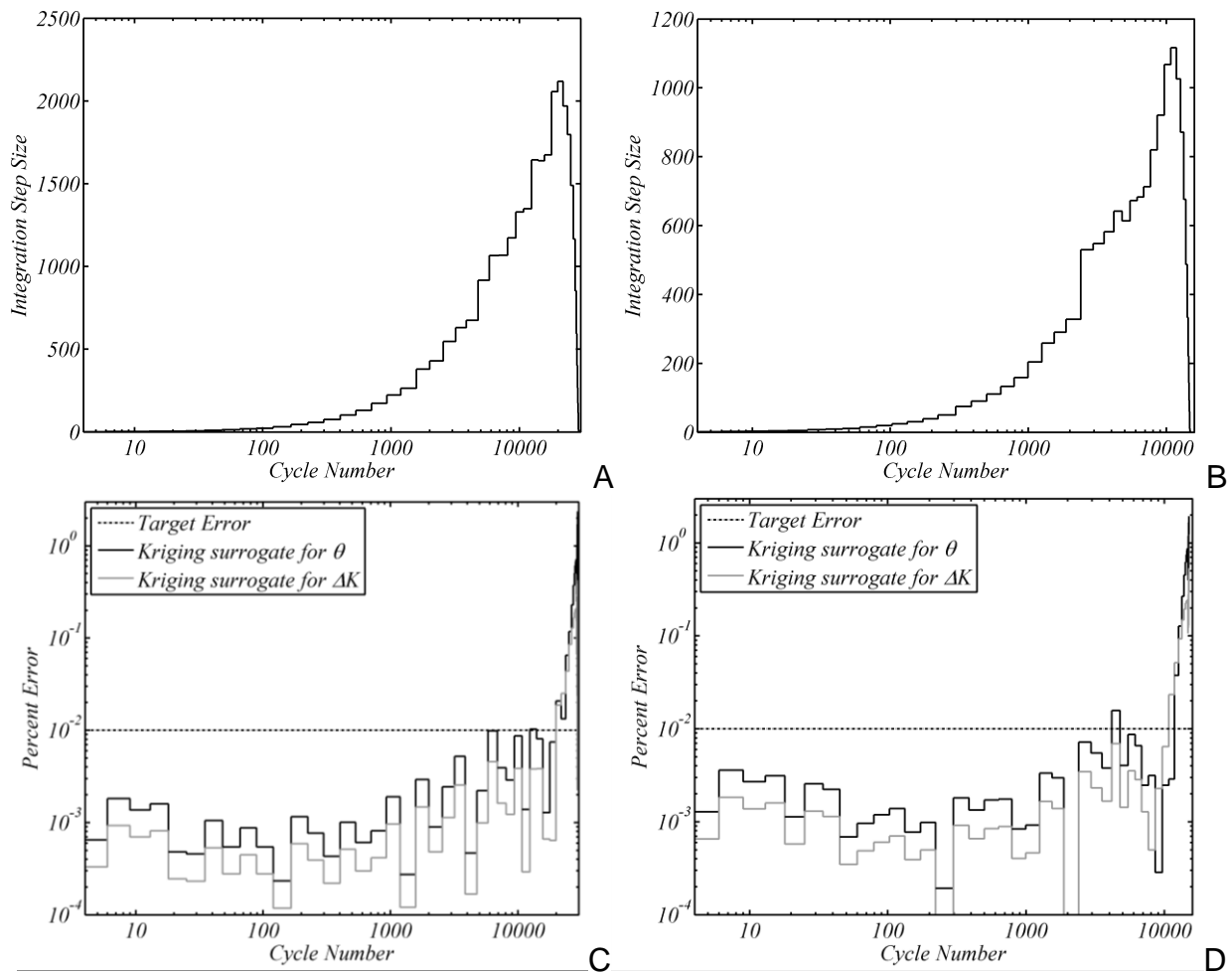


Figure 5-7. Comparison of cycle number and integration step size or percent error for surrogate for $R = 0.1$ and $R = 0.5$ for aluminum 2024. A) Integration step size for aluminum 2024, $R = 0.1$, B) Integration step size for aluminum 2024, $R = 0.5$, C) Percent error for aluminum 2024, $R = 0.1$, D) Percent error for aluminum 2024, $R = 0.5$. (Note when error exceeds target, step size reduces).

Summary

The ordinary differential equation which governs fatigue crack growth cannot easily be solved due to the fact that in general no analytical expression of the stress intensity factor as a function of crack size and crack geometry is available. For a general geometry, the stress intensity factor can only be calculated at the current crack size using the extended finite element method. It is common to take a forward Euler approach to the direct calculation of both the magnitude and direction of crack growth for a given function evaluation or for the back-calculation of the elapsed number of cycles. The forward Euler approach limits the step size and increases the number of function evaluations needed to achieve sufficient accuracy.

A kriging surrogate was used to fit the available history of the stress intensity factor and crack growth direction. The surrogate model allows one to extrapolate ahead of the current data point, enabling the use of the midpoint approximation method for the evaluation of both stress intensity factor and crack growth direction. A variable step size algorithm is also presented to allow for the step size to be adjusted for a given allowable error. This method produces comparable accuracy with a significantly reduced number of function evaluations for a range of initial crack sizes, applied stresses, materials, and crack geometries.

Another area of study is to consider cases of mixed-mode crack growth. In this case the path of crack growth will be curved. Thus, the allowable step size based on the approximation of the solution of the fatigue crack growth law may be limited by the need to have a converged crack path. This is an important interaction which will need to be considered for practical use of the kriging assisted methods for use in a finite element environment.

CHAPTER 6
AN EXACT EXTENDED FINITE ELEMENT METHOD REANALYSIS ALGORITHM

Reanalysis Methods

Crack growth is often modeled as a quasi-static problem. In this methodology, only a small portion of the XFEM stiffness matrix will change as crack growth occurs. Once Heaviside terms are added to the XFEM stiffness matrix in order to model the discontinuity due to a crack, they will remain unchanged in future iterations of crack growth. At each iteration of crack growth, the previous crack tip components will need to be modified to account for the changing crack tip position. The objective of this paper is to maximize recycling computational resources during crack growth simulation by using this property. For the first iteration of the quasi-static solution procedure, the Cholesky factorization of the full XFEM stiffness matrix is calculated. In subsequent iterations, only the changed portion of the XFEM stiffness matrix is calculated (i.e. the new Heaviside and crack tip enrichment components). The existing Cholesky factorization is directly modified using row-add and row-delete operations. This solution procedure significantly reduces the cost of assembling the stiffness matrix and solving the system of matrix equations in the XFEM framework, allowing for increased convergence of crack paths within a computational budget.

For many optimization applications involving XFEM, the same basic algorithm may be used to reduce the computational cost associated with the repeated iterations within the optimization cycle. In the case of damage identification [99, 100, 182], all enriched elements may evolve over time (i.e. the Heaviside enrichment is non-constant). For shape optimization [140], the changes to the elements along the shape boundary being modified can be updated along with any enriched degrees of freedom being considered.

Reanalysis algorithms [183, 184] have been developed primarily for use in the fields of design and optimization to efficiently solve problems where small perturbations to the finite element domain are made. This may take the form of changing the location of elements, adding additional elements, or a combination of both. These methods can be classified as either being exact or approximate [185]. The exact methods are generally based on the Sherman-Morrison [186] inversion formula and consider cases where the modified elements affect a small number of degrees of freedom. The approximate methods are typically iteration based and are used when the modified elements affect a large number of degrees of freedom. Li and Wu [184, 185, 187] have introduced algorithms for the reanalysis of structures with added degrees of freedom through the use of an iterative solver. An exact reanalysis algorithm is introduced here based on the direct modification of an existing Cholesky factorization [188-194]. In this paper Cholesky factorization was chosen instead of a Sherman-Morrison approach due to collaboration with individuals containing extensive knowledge of Cholesky factorizations.

Exact Reanalysis by Modification of an Existing Cholesky Factorization

Recall that the displacement approximation and stiffness matrix for the XFEM with a crack is given as

$$\mathbf{u}^h(\mathbf{x}) = \mathbf{V}(\mathbf{x}) \sum_{I \in \Omega} N_I(\mathbf{x}) \left[\mathbf{u}_I + \sum_{I \in \Omega_H} H_I(\mathbf{x}) \mathbf{a}_I + \sum_{I \in \Omega_T} \sum_{\alpha=1}^4 \Phi_{I,\alpha}(\mathbf{x}) \mathbf{b}_I^\alpha \right] \quad 6-1$$

and

$$\mathbf{K} = \begin{bmatrix} \mathbf{K}_{uu} & \mathbf{K}_{au}^T & \mathbf{K}_{bu}^T \\ \mathbf{K}_{au} & \mathbf{K}_{aa} & \mathbf{K}_{ba}^T \\ \mathbf{K}_{bu} & \mathbf{K}_{ba} & \mathbf{K}_{bb} \end{bmatrix} \quad 6-2$$

It can be noticed from Eqs. 6-1 and 6-2 that the stiffness component associated with the traditional finite element approximation is not a function of the crack location, which implies that the \mathbf{K}_{uu} component of the stiffness matrix will be constant at each iteration of crack growth. This implies that the changing portion of the stiffness matrix is limited to the enriched portion, which will be small compared to the un-enriched portion.

Furthermore, it can also be noticed that while the Heaviside enrichment terms \mathbf{K}_{aa} are functions of the crack location within an element, that once a Heaviside enrichment or coupling to the classical FE approximation is introduced its value will not change in any future iterations. The stiffness components \mathbf{K}_{uu} , \mathbf{K}_{au} , and \mathbf{K}_{aa} will be constant for future iterations of crack growth. An example of the nodes whose corresponding stiffness components need to be updated to account for crack growth is shown in Figure 6-1.

Once the boundary conditions have been applied, the stiffness matrix becomes positive definite and it is possible to compute the Cholesky factorization for the XFEM stiffness matrix. The Cholesky factorization for the XFEM stiffness matrix \mathbf{K} in Eq. 6-2 is given by

$$\mathbf{K} = \begin{bmatrix} \mathbf{K}_{uu} & \mathbf{K}_{au}^T & \mathbf{K}_{bu}^T \\ \mathbf{K}_{au} & \mathbf{K}_{aa} & \mathbf{K}_{ba}^T \\ \mathbf{K}_{bu} & \mathbf{K}_{ba} & \mathbf{K}_{bb} \end{bmatrix} = \begin{bmatrix} \mathbf{L}_{uu} & & \\ \mathbf{L}_{au} & \mathbf{L}_{aa} & \\ \mathbf{L}_{bu} & \mathbf{L}_{ba} & \mathbf{L}_{bb} \end{bmatrix} \begin{bmatrix} \mathbf{D}_{uu} & & \\ & \mathbf{D}_{aa} & \\ & & \mathbf{D}_{bb} \end{bmatrix} \begin{bmatrix} \mathbf{L}_{uu}^T & \mathbf{L}_{au}^T & \mathbf{L}_{bu}^T \\ & \mathbf{L}_{aa}^T & \mathbf{L}_{ba}^T \\ & & \mathbf{L}_{bb}^T \end{bmatrix} = \mathbf{LDL}^T \quad 6-3$$

where the components of \mathbf{L} and \mathbf{D} can be calculated as

$$\mathbf{D}_{jj} = \mathbf{K}_{jj} - \sum_{k=1}^{j-1} \mathbf{L}_{jk}^2 \mathbf{D}_{kk} \quad 6-4$$

and

$$\mathbf{L}_{ij} = \frac{1}{\mathbf{D}_{jj}} \left(\mathbf{K}_{ij} - \sum_{k=1}^{j-1} \mathbf{L}_{ik} \mathbf{L}_{jk} \mathbf{D}_{kk} \right) \quad \text{for } i > j. \quad 6-5$$

In the case of modeling crack growth in a quasi-static manner, there will be many iterations of crack growth. Each iteration will require its own Cholesky factorization and corresponding floating-point operations for factoring \mathbf{K} .

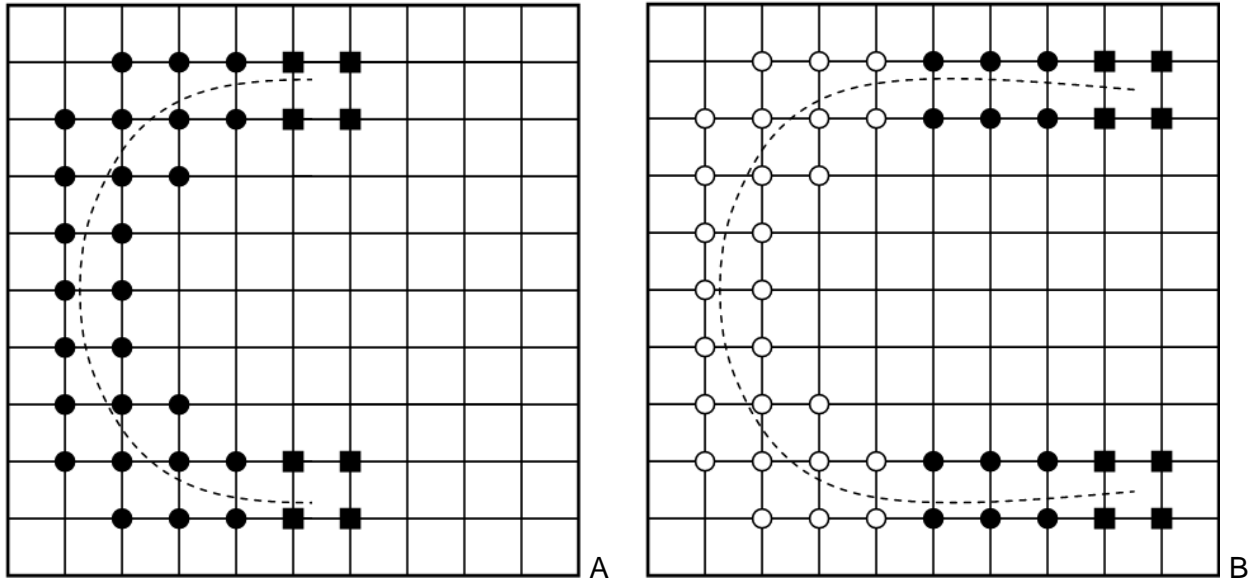


Figure 6-1. Finite element mesh with enriched nodes. A) Initial crack geometry, B) First iteration of crack growth. (Note circles denote nodes enriched with the Heaviside function and squares denote nodes enriched with the crack tip enrichment function, filled circles and squares denote new enriched nodes for the current iteration while open circles and squares denote previously enriched nodes).

As the XFEM stiffness matrix is largely constant and slowly evolving (i.e. additional Heaviside and changing crack tip stiffness components), it would be computationally attractive if the Cholesky factorized matrices, \mathbf{L} and \mathbf{D} , are directly updated. The modification of the initial Cholesky factorization through sparse row-add and row-delete operations [188, 191-194] requires fewer floating-point operations for subsequent iterations of crack growth.

Suppose the i th row and column of \mathbf{K} is equal to the i th row/column of the identity matrix. This i th row has no effect on the Cholesky factorization of the rest of the matrix. We refer to replacing this i th row/column of \mathbf{K} with a nontrivial row/column as a “row

addition.” It can be computed with a triangular solve and rank-1 downdate, as described below. A “row deletion” does the opposite, by replacing a non-trivial row/column of \mathbf{K} with the corresponding row/column of the identity matrix.

An alternative approach would be to append newly enriched degrees of freedom at the bottom/right of the system of equations, and thus the size of \mathbf{K} and correspondingly \mathbf{L} and \mathbf{D} would dynamically grow. One could find the fill-reducing ordering based on the initial \mathbf{K} , and then simply add the new rows and columns of \mathbf{L} and \mathbf{D} to the bottom right corner of the matrices. This will introduce drastic fill-in since the original fill-reducing ordering did not account for the new entries. Another option would be to create a matrix \mathbf{K}_s that assumes that all nodes in \mathbf{K} contain both the Heaviside and crack tip enrichment. The size of this matrix is approximately ten times the size of \mathbf{K} for the case of a two-dimensional structure. Any enriched nodes that are inactive have their corresponding rows and columns set to zero with unity along the diagonal. Therefore, all the inactive enriched nodes do significantly affect the size of the resulting sparse matrix. If the possible crack growth path is known *a priori*, it would be possible to limit the number of initially inactive enriched nodes that are considered.

In order to find the fill-reducing ordering for this matrix, the connectivity of all possible elements is used to create a matrix \mathbf{K}_s with unity in all matrix locations which would contain information if all possible Heaviside and crack tip nodes were active. The nonzero pattern of \mathbf{K}_s is a superset of any \mathbf{K} that would be seen in the subsequent numerical factorizations computed during crack propagation, and thus the nonzero pattern of its Cholesky factor \mathbf{L}_s will also be a superset of any Cholesky factor \mathbf{L} seen later. A fill-reducing ordering is obtained for \mathbf{K}_s from the approximate minimum degree

ordering (AMD) algorithm [189, 195, 196]. Finding an optimal fill-reducing ordering for an arbitrary is computationally impossible, and thus AMD is a heuristic, as are all fill-reducing algorithms. However, since AMD is applied to the entire \mathbf{K}_s matrix, it will limit the fill-in in the matrix \mathbf{L}_s , and thus it will also limit the upper bound of any fill-in in any Cholesky factor \mathbf{L} computed later. If AMD were simply applied to the first \mathbf{L} , then new entries in \mathbf{K} that AMD did not consider could cause catastrophic fill-in in \mathbf{L} . After applying the fill-reducing ordering, the permuted stiffness matrix is referred to as \mathbf{K}_p . The fill-reducing ordering is applied to reduce the fill-in of subsequent iterations of crack growth as the active enriched nodes evolve.

For elements that are initially intersected by the crack, the corresponding enriched degrees of freedom are set active, while all other nodes are defined inactive. Any rows or columns of \mathbf{K} , and subsequently \mathbf{K}_p , corresponding to an inactive enriched degree of freedom have rows and columns which are set to zero, except for their diagonal component which is unity. In order to update the Cholesky factorization, only the modified components of the updated stiffness matrix $\bar{\mathbf{K}}$ (e.g. new Heaviside and crack tip components) are needed. Before updating the previous Cholesky factorization, the fill-reducing ordering is applied to $\bar{\mathbf{K}}$ yielding $\bar{\mathbf{K}}_p$. The initial Cholesky factorization is

$$\mathbf{LDL}^T = \begin{bmatrix} \mathbf{L}_{11} & & \\ 0 & 1 & \\ \mathbf{L}_{31} & 0 & \mathbf{L}_{33} \end{bmatrix} \begin{bmatrix} \mathbf{D}_{11} & & \\ & 1 & \\ & & \mathbf{D}_{33} \end{bmatrix} \begin{bmatrix} \mathbf{L}_{11}^T & 0 & \mathbf{L}_{31}^T \\ 1 & 0 & \\ & & \mathbf{L}_{33}^T \end{bmatrix} = \begin{bmatrix} \mathbf{K}_{11} & 0 & \mathbf{K}_{31}^T \\ 0^T & 1 & 0^T \\ \mathbf{K}_{31} & 0 & \mathbf{K}_{33} \end{bmatrix} = \mathbf{K}_p, \quad 6-6$$

where the identity row denotes an inactive enriched node and \mathbf{K}_p is the XFEM stiffness matrix permuted to a fill-reducing ordering. After crack growth has occurred and the previously inactive node becomes active, the new stiffness matrix $\bar{\mathbf{K}}_p$ is given as

$$\bar{\mathbf{L}}\bar{\mathbf{D}}\bar{\mathbf{L}}^T = \begin{bmatrix} \mathbf{L}_{11} & & \\ \bar{l}_{12}^T & 1 & \\ \mathbf{L}_{31} & \bar{l}_{32} & \mathbf{L}_{33} \end{bmatrix} \begin{bmatrix} \mathbf{D}_{11} & & \\ & \bar{d}_{22} & \\ & & \mathbf{D}_{33} \end{bmatrix} \begin{bmatrix} \mathbf{L}_{11}^T & \bar{l}_{12} & \mathbf{L}_{31}^T \\ & 1 & \bar{l}_{32}^T \\ & & \mathbf{L}_{33}^T \end{bmatrix} = \begin{bmatrix} \mathbf{K}_{11} & \bar{k}_{12} & \mathbf{K}_{31}^T \\ \bar{k}_{12}^T & \bar{k}_{22} & \bar{k}_{32}^T \\ \mathbf{K}_{31} & \bar{k}_{32} & \mathbf{K}_{33} \end{bmatrix} = \bar{\mathbf{K}}_p. \quad 6-7$$

The modification of the initial \mathbf{LDL}^T to add a new enriched degree of freedom to the Cholesky factorization is accomplished as:

1. Solve the lower triangular system $\mathbf{L}_{11}\mathbf{D}_{11}\bar{l}_{12} = \bar{k}_{12}$ for \bar{l}_{12} .
2. $\bar{d}_{22} = \bar{k}_{22} - \bar{l}_{12}^T\mathbf{D}_{11}\bar{l}_{12}$
3. $\bar{l}_{32} = (\bar{k}_{32} - \mathbf{L}_{31}\mathbf{D}_{11}\bar{l}_{12})/\bar{d}_{22}$
4. $w = \bar{l}_{32}\sqrt{\bar{d}_{22}}$
5. Perform the rank-1 downdate $\bar{\mathbf{L}}_{33}\bar{\mathbf{D}}_{33}\bar{\mathbf{L}}_{33}^T = \mathbf{L}_{33}\mathbf{D}_{33}\mathbf{L}_{33}^T - ww^T$

The total time taken for steps 1 to 3 is proportional to the sum of the number of entries in each column j of \mathbf{L} (\mathbf{L}_{11} and \mathbf{L}_{31}) for which the j th entry in $\bar{\mathbf{L}}_{12}$ is nonzero. This is an optimal result. The time taken for step 4 is proportional to the number of entries in each column j in $\bar{\mathbf{L}}_{32}$ for which \bar{d}_{jj} is nonzero. The time taken for this step is exactly proportional to the number of entries in \mathbf{L}_{33} that change. This time includes both the symbolic work of figuring out which entries change, and then doing the numerical work to change them. While this seems like an obvious goal of a rank-1 downdate, it is far from trivial to obtain [188, 191-194].

Crack tip stiffness components will need to be modified after each iteration of crack growth, therefore it is necessary to also consider the case of a row-delete operation to remove old entries into the stiffness matrix associated with the crack tip enrichment function. In this case from the previous iteration the stiffness matrix and corresponding factorization are given as

$$\mathbf{LDL}^T = \begin{bmatrix} \mathbf{L}_{11} & & \\ l_{12}^T & 1 & \\ \mathbf{L}_{31} & l_{32} & \mathbf{L}_{33} \end{bmatrix} \begin{bmatrix} \mathbf{D}_{11} & & \\ & 1 & \\ & & \mathbf{D}_{33} \end{bmatrix} \begin{bmatrix} \mathbf{L}_{11}^T & l_{12} & \mathbf{L}_{31}^T \\ & 1 & l_{32}^T \\ & & \mathbf{L}_{33}^T \end{bmatrix} = \begin{bmatrix} \mathbf{K}_{11} & k_{12} & \mathbf{K}_{31}^T \\ k_{12}^T & 1 & k_{32}^T \\ \mathbf{K}_{31} & k_{32} & \mathbf{K}_{33} \end{bmatrix} = \mathbf{K}_p \quad 6-8$$

where the second row and column correspond to a enriched crack tip entry in the XFEM stiffness matrix. The corresponding stiffness matrix and factorization with the old crack tip component removed is given as

$$\bar{\mathbf{L}}\bar{\mathbf{D}}\bar{\mathbf{L}}^T = \begin{bmatrix} \mathbf{L}_{11} & & \\ 0 & 1 & \\ \mathbf{L}_{31} & 0 & \bar{\mathbf{L}}_{33} \end{bmatrix} \begin{bmatrix} \mathbf{D}_{11} & & \\ & 1 & \\ & & \bar{\mathbf{D}}_{33} \end{bmatrix} \begin{bmatrix} \mathbf{L}_{11}^T & 0 & \mathbf{L}_{31}^T \\ & 1 & 0 \\ & & \bar{\mathbf{L}}_{33}^T \end{bmatrix} = \begin{bmatrix} \mathbf{K}_{11} & 0 & \mathbf{K}_{31}^T \\ 0^T & 1 & 0^T \\ \mathbf{K}_{31} & 0 & \mathbf{K}_{33} \end{bmatrix} = \bar{\mathbf{K}}_p \quad 6-9$$

The modification of the initial \mathbf{LDL}^T to remove a crack tip enriched degree of freedom from the Cholesky factorization is accomplished as:

1. $\bar{l}_{12} = 0$
2. $\bar{d}_{22} = 1$
3. $\bar{l}_{32} = 0$
4. $w = l_{32}\sqrt{d_{22}}$
5. Perform the rank-1 update $\bar{\mathbf{L}}_{33}\bar{\mathbf{D}}_{33}\bar{\mathbf{L}}_{33}^T = \mathbf{L}_{33}\mathbf{D}_{33}\mathbf{L}_{33}^T + ww^T$.

Just as the rank-1 update, above, the total time taken by steps 1 to 5 is proportional to the number of entries in \mathbf{L} that change.

The new stiffness components associated with the crack tip enrichment function are added using the row-add operation previously discussed. For more details on the row-add and row-delete algorithms, readers are referred to the work of Davis [193, 194] including proofs of optimal convergence. Our implementation was accomplished based on the creation of a MEX file which created a link between our MATLAB[®] XFEM code [134] and CHOLMOD [190]. The proposed reanalysis algorithm for crack growth can be summarized as follows:

1. Calculate the superset matrix \mathbf{K}_s for the initial quasi-static iteration.
2. Find the fill-reducing permutation of \mathbf{K}_s with AMD.
3. Calculate \mathbf{L} and \mathbf{D} from the initial \mathbf{K} using the fill-reducing ordering permutation.
4. Solve for the traditional and enriched degrees of freedom.
5. Calculate K_I , K_{II} , and ΔK . Grow the crack.
6. Calculate the new portions of $\bar{\mathbf{K}}$ from prior crack growth
7. Use row-delete to remove prior crack tip \mathbf{K} components from \mathbf{L} and \mathbf{D} .
8. Use row-add to add new Heaviside and crack tip $\bar{\mathbf{K}}$ components to \mathbf{L} and \mathbf{D} .
9. Repeat steps 3-7.

For the optimization example, no crack growth occurs during step 5, and all Heaviside and crack tip components of \mathbf{K} are removed from \mathbf{L} and \mathbf{D} using row-delete operations during step 7. While not shown here, this method could easily be applied to the evolution of a void or inclusion as was considered by Moës and Sukumar [55, 113]. The use of row-add and row-delete operations could also be used to consider cases where boundary conditions are non-constant between iterations of crack growth.

Example Problems

Reanalysis of an Edge Crack in a Finite Plate

The first step in evaluating the proposed reanalysis algorithm is to consider a simple geometry that will allow us to both assess the savings from the proposed algorithm as well as to study the effect that increasing or decreasing the mesh density locally around the crack tip has on the proposed reanalysis algorithm. To perform this study, an edge crack of initial length 0.25 m in a finite plate of size 2 m x 2 m under unit uniaxial tension with thirty increments of 0.05 m crack growth was considered as shown in Figure 6-2. The material properties were elastic modulus $E = 1$ Pa and Poisson's ratio $\nu = 0.3$. In order to study the effect of repeated iterations of crack growth a structured mesh of square plane strain elements with characteristic length 0.05 m was used, which was sufficient to achieve convergence in the Mode I and Mode II stress intensity factors.

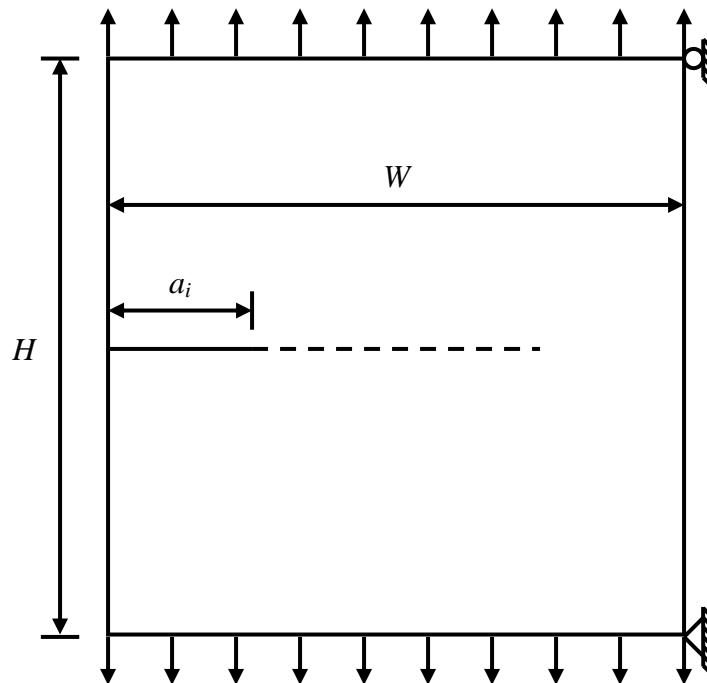


Figure 6-2. Edge crack in a finite plate geometry used to test quasi-static crack growth with the reanalysis algorithm.

The savings is both the stiffness matrix assembly time as well as the time to factoring the global stiffness matrix or updating an existing factorization and then solving the resulting system of equations. The normalized times were calculated as the reanalysis algorithm divided by the traditional approach as a function of crack growth iteration as shown in Figure 6-3. The traditional approach is considered to be calculating or factoring and solving \mathbf{K} at each iteration from scratch. The comparison between the native MATLAB[®] function *backslash* and CHOLMOD for factoring and solving the system of equations is considered reasonable as they both were written by the same author. The times were normalized in order to facilitate easy viewing of the savings that the proposed reanalysis algorithm yields. The proposed reanalysis reduces the assembly time by approximately 80% and factorization time by approximately 70%. It can be noticed from Figure 6-3 that the general trend for assembly is increased savings with additional iterations. This can be explained as having a larger crack increases the bandwidth of \mathbf{K} , while only calculating the new enriched elements is approximately constant for the case of a fixed Δa . The increased fill-in as the number of enriched element increases subtly increases the cost of updating the existing Cholesky factorization as the number of crack growth iterations increases.

The second consideration was the effect that increasing or decreasing mesh density would have on the assembly and factorization/solving savings. Two iterations of the previous problem were repeated for a range of mesh densities. The number of elements per unit length is plotted against the normalized time in Figure 6-4 where the time from the first iteration where the Cholesky update is directly modified is normalized by the time from the iteration where the Cholesky factorization is first performed. Note

that both trends show increased savings with increasing mesh density (i.e. number of degrees of freedom).

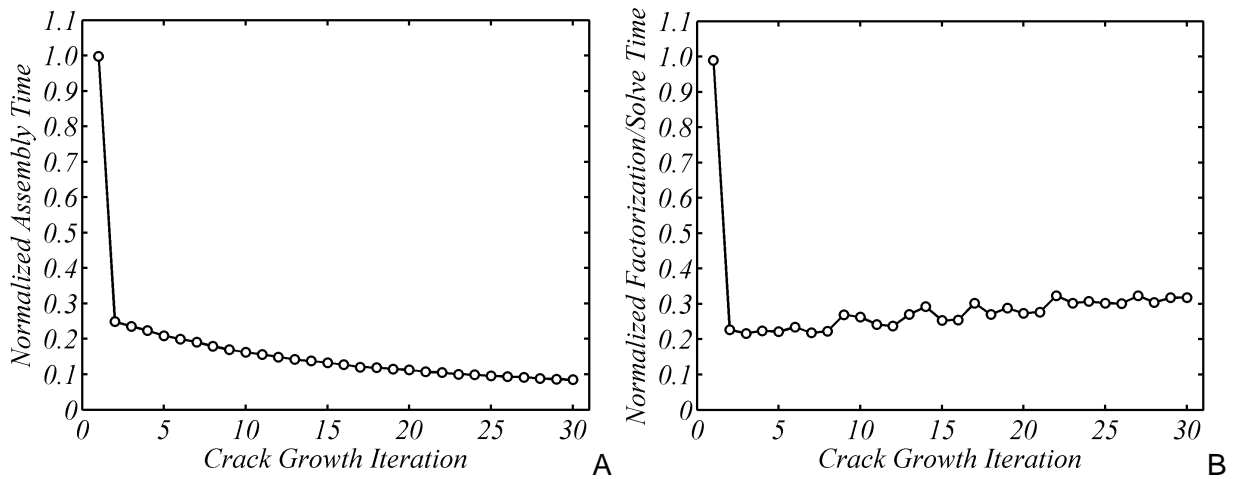


Figure 6-3. Normalized computational time for stiffness matrix assembly as well as factorization and solving of system of linear equations as a function of number of iterations. A) Stiffness matrix assembly, B) Factorization and solving of system of linear equations.

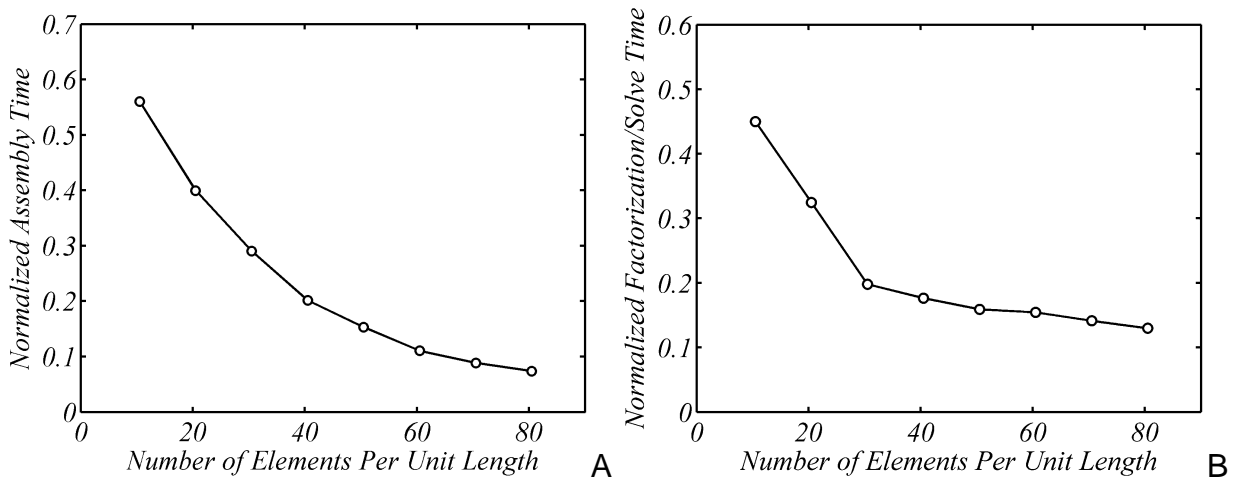


Figure 6-4. Normalized computational time for stiffness matrix assembly as well as factorization and solving of system of linear equations as a function of number of mesh density. A) Stiffness matrix assembly, B) Factorization and solving of system of linear equations.

Optimization for Finding Crack Initiation in a Plate with a Hole

To assess the applicability of the proposed reanalysis algorithm in an optimization framework, a simple optimization problem is considered as a second example. A finite plate of size 4 m x 4 m with a hole of radius 0.5 m centered at the middle of the plate is

considered. The material properties were repeated from the previous example of $E = 1$ Pa and $\nu = 0.3$. The mesh was a structured mesh of square elements with characteristic length of 0.05 m. The plate is subjected to uniaxial tension. The objective is to find the crack initiation point on the edge of a hole. A crack of length 0.15 m emanates from the hole at an angle θ as shown in Figure 6-5.

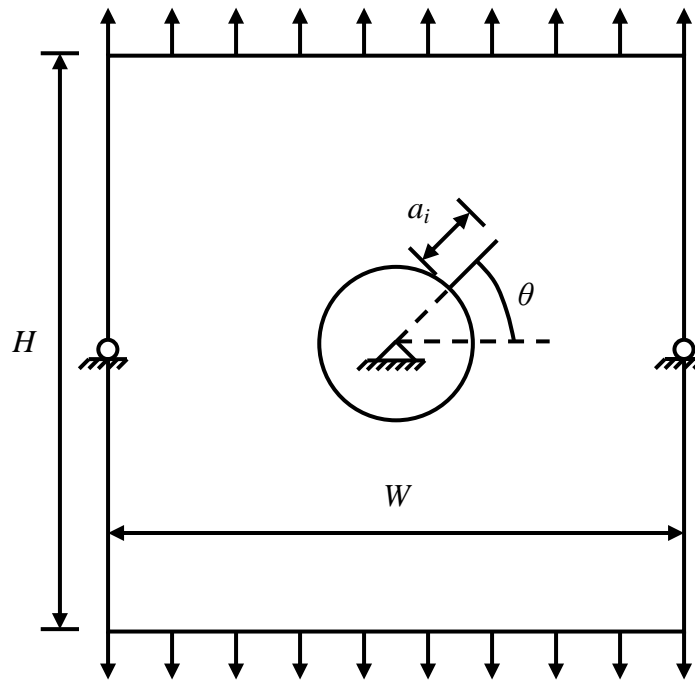


Figure 6-5. Edge crack in a finite plate geometry used to test optimization with the reanalysis algorithm.

The optimization problem is solved using the *fminbnd* function native to MATLAB[®] for

$$\begin{aligned} \min \quad & -G(\theta) = -\frac{K_I^2 + K_{II}^2}{E'} \\ \text{s.t.} \quad & -\frac{\pi}{2} \leq \theta \leq \frac{\pi}{2} \end{aligned} \tag{6-10}$$

where $E' = E$ for plane stress and $E' = E/(1-\nu^2)$ for plane strain. As the optimization algorithm changes the angle theta, the factorized stiffness matrix is modified by deleting

the crack in the previous iteration and adding a crack corresponding to the new angle. The solution converges after 25 iterations to an angle of $\theta = -9.92 \cdot 10^{-8}$ radians as the angle yielding the maximum energy release rate, which is in good agreement with the expected solution of $\theta = 0$ radians given the tolerances on the function and θ were 10^{-9} and 10^{-6} .

Figure 6-6 shows that for the optimization problem both the assembly and factorization/solving trends are comparable to the results from the quasi-static problem. The assembly time no longer decreases as the iteration increases as no additional degrees of freedom are being introduced into the system of equations. The factorization and solving time is also largely constant as the matrix size is not changing as no crack growth is occurring.

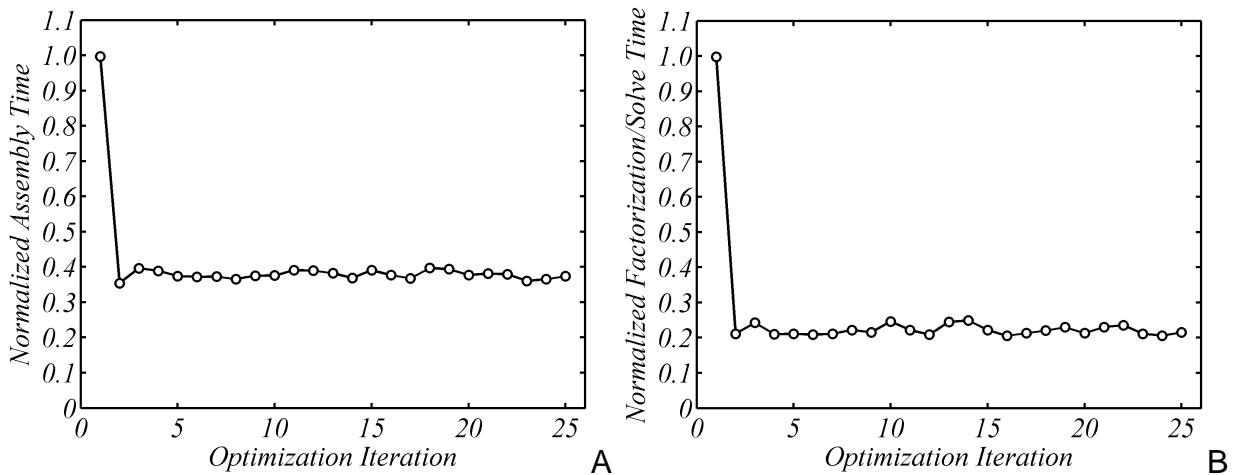


Figure 6-6. Normalized computational time for stiffness matrix assembly as well as factorization and solving of system of linear equations as a function of number of iterations. A) Stiffness matrix assembly, B) Factorization and solving of system of linear equations.

Summary

An exact reanalysis algorithm is presented based on the direct modification of a sparse Cholesky factorization through the use of row modification operations. It has been shown that there is a significantly reduced computational cost for each iteration of

crack growth based on locally updating a Cholesky factorization instead of simply factoring and solving the resulting system of linear equations. A study of the effect on mesh density was performed and it was found that while savings can be achieved over the full range of mesh densities; the largest savings were achieved when the mesh had an increased level of refinement. The reanalysis algorithm allows for one to consider a smaller crack growth increment, which should lead to a better prediction of the crack growth path within a comparable computational budget. The use of the reanalysis algorithm in an optimization framework was also introduced and shown to reduce the cost of solving optimization problems involving cracks.

CHAPTER 7
VARIABLE AMPLITUDE MULTI-AXIAL FATIGUE ANALYSIS OF WING PANEL
Scaling of Normalized Flight Data from the Air Force Research Laboratory

The Air Force Research Laboratory (AFRL) at Wright-Patterson Air Force Base in Ohio has provided normalized flight data for 19 different aircraft flights. The normalized flight data includes: normal acceleration, lateral acceleration, longitudinal acceleration, roll acceleration, pitch acceleration, yaw acceleration, roll rate, pitch rate, yaw rate, airspeed, altitude, angle of attack, flap angle, fuel quantity, and Mach number. The orientations related to the various acceleration and rate variables are given in Figure 7-1. For the finite element model, the x -axis is located at the root of the wing at the midpoint of the chord length. The combined flight histories from the 19 flights was chosen to be the data set for this example problem. The flight data is used in conjunction with an Abaqus[®] finite element model of an airplane wing box in order to calculate the stress history for a wing panel. At this point, the stress is calculated assuming there is no crack in the panel (nominal stress). This nominal stress history is then used to calculate stress intensity factors at the crack tip of the plate using the MXFEM code where the advantages of the exact reanalysis algorithm are used to solve the problem of an airplane wing panel subjected to variable amplitude multi-axial loading.

In order to simplify the analysis of a wing model, only a subset of the available normalized flight data have been used as a part of this work. The parameters which were identified for use in the predictive model are: normal acceleration, roll acceleration, airspeed, Mach number, angle of attack, and fuel quantity. As the values provided by the AFRL are normalized, they must be scaled according to our estimation of the

expected range of values that the chosen parameters would take if they were not normalized. The parameters were scaled based on the assumption that the data corresponded to a commercial aircraft flight instead of that of a military aircraft. The conversion the data from normalized to scaled values is summarized in Table 7-1 for Flight ID 152. The conversion for all flights is presented in Appendix C.

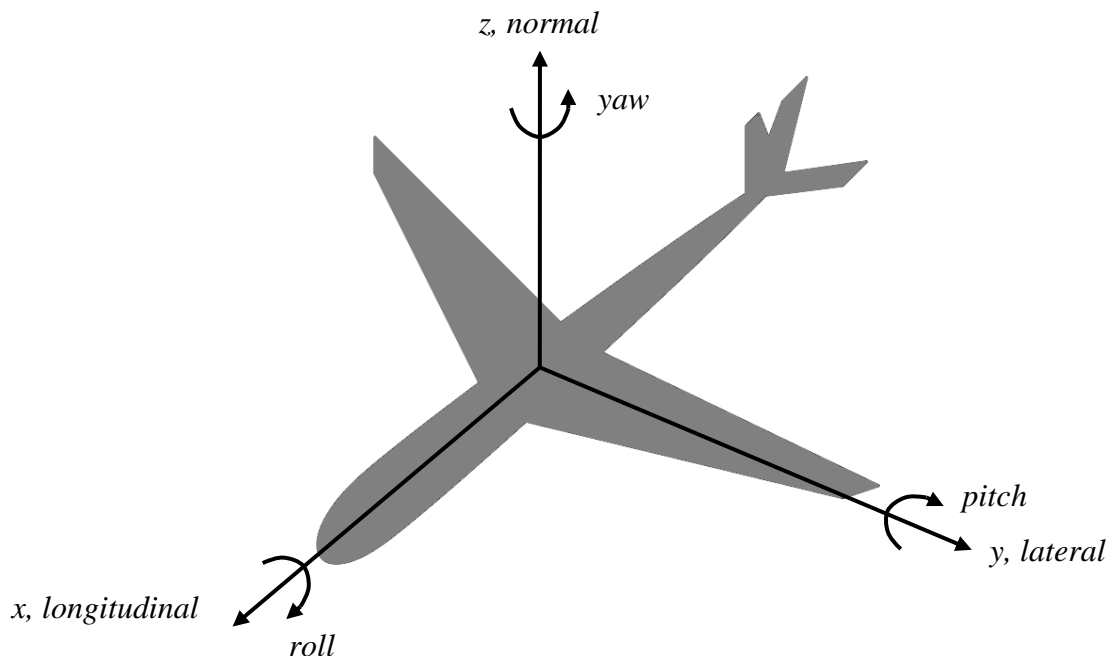


Figure 7-1. Coordinate system (x,y,z) and directional names for an airplane.

The normal acceleration is related to the gravity forces (g-force) acting upon the aircraft. Aerobatic and military aircraft can experience maximum g-force of 9-12 g [197]. Level flight would expect to experience forces equal to about 1 g. A typical banked turn with bank angle of 30° may cause forces of about 1.5 g [198]. It is assumed that the range of g-force experienced during a commercial aircraft flight is from a lower value of 0.75 g and a maximum value of 1.5 g.

The normalized roll acceleration a_{norm} is used to approximate the bank angle θ_B associated with a banked turn. From a simple physics model it can be noticed that the

roll acceleration is directly related to the bank radius [199]. For a larger roll acceleration the bank radius will decrease, while for a smaller roll acceleration the bank radius will increase. The banking radius is also inversely proportional to the bank angle. Therefore, the general trend can be established that the roll acceleration and bank angle are proportional. It is assumed that a commercial aircraft will not exceed the bank angle of 30° , with a minimum bank angle of 0° during level flight.

The normalized fuel capacity f_{norm} is related to the mass of fuel m_{fuel} by considering the fuel capacity and mass of fuel of an aircraft. The Boeing 767 has a maximum fuel capacity of 63,000 L [200]. There are two main types of commercial aircraft fuel in use in the world [201]. In the United States, the aircraft fuel is commonly known as Jet A. In the remainder of the world a different specification is used which is known as Jet A-1. Additional additives are commonly used to convert commercial aircraft fuel into military fuel. The density of Jet A and Jet A-1 are very similar and depending upon the particular mixture will have density between 0.775 to 0.840 kg/L. Therefore, the expected fuel mass for an aircraft would range between 48,825 and 52,920 kg for a fully fueled aircraft. The assumed mass of a fully fueled aircraft is chosen here to be 50,000 kg. Furthermore, it is assumed that upon landing an aircraft will have at least 1000 L of fuel in reserve, which corresponds to a minimum fuel mass of 800 kg. The fuel mass is combined with the empty mass of the aircraft, 86,070 kg for a Boeing 767, to yield the total mass of the aircraft and fuel at each AFRL data point.

The normalized Mach number M_{norm} is related to the true mach number M by scaling the maximum and minimum values to 0 and 0.8 Mach [169]. The normalized airspeed v_{norm} is related to the true airspeed v of the aircraft by simply scaling the

minimum values of normalized airspeed to be equal to 0 m/s and the maximum value to 236 m/s [169]. Similarly, the normalized angle of attack α_{norm} is scaled to α such that the maximum and minimum normalized values correspond to 0° and 10° [202].

Table 7-1. Maximum and minimum values of normalized and scaled flight data with conversion relationship for Flight ID 152.

Variable	Norm Min	Norm Max	Scaled Min	Scaled Max	Conversion
g	-0.208	0.957	0.75	1.5	$g = 0.644g_{norm} + 0.884$
θ_B	-1.00	0.624	0	30	$\theta_B = 18.5 a_{roll} + 18.48$
m_{fuel}	0.169	0.975	800	50,000	$m_{fuel} = 51300f_{norm}$
M	0.0191	0.977	0	0.80	$M = 0.835M_{norm} - 0.0159$
v	0.0222	0.839	0	851	$v = 289v_{norm} - 6.42$
α	0.00	0.853	0	10	$\alpha = 11.7\alpha_{norm}$

Finite Element Wing Model

For the stress analysis of an airplane wing a finite element model of a wing box is modeled. A wing box is the main structural support for a wing and supports most of the loading that occurs on an airplane wing. An airfoil is then attached to the wing box in order to produce the desired aerodynamic force. In this work, a finite element model of the wing box geometry originally used as part of a probabilistic optimization problem was used. In this previous work, an elliptical distribution was used to determine the span-wise pressure distribution, but the chord-wise pressure distribution was neglected. A figure of a wing geometry showing the chord and span lengths is given in Figure 7-2 and a figure of the wing in the chosen coordinate system is given in Figure 7-3. The chord-wise pressure distribution caused by the lift force is introduced along with the lift-induced drag and the magnitude of the resulting pressures applied to the wing are given in terms of the chosen scaled variables from the normalized AFRL data. For the purposes of the finite element simulation the effects of lift and drag on the wing are considered to act independently and are separated into unique analysis.

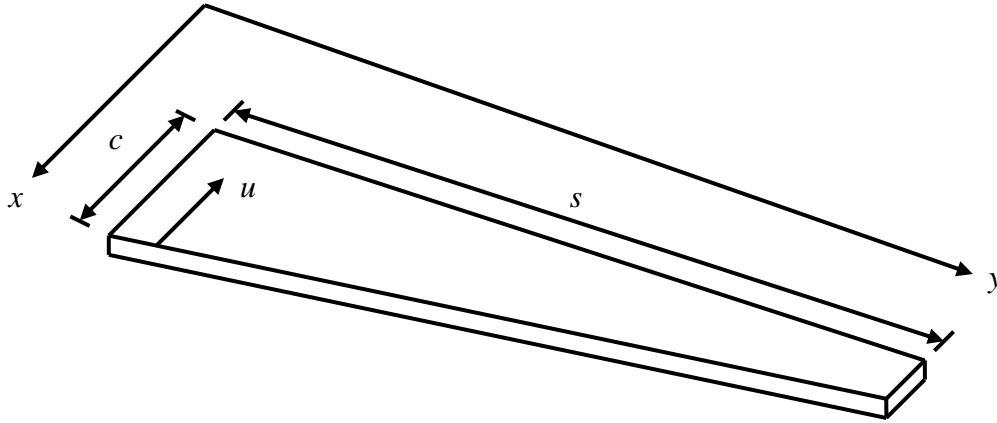


Figure 7-2. Example of a wing box with span s , chord length c which is a function of y , and normalized x -coordinate u .

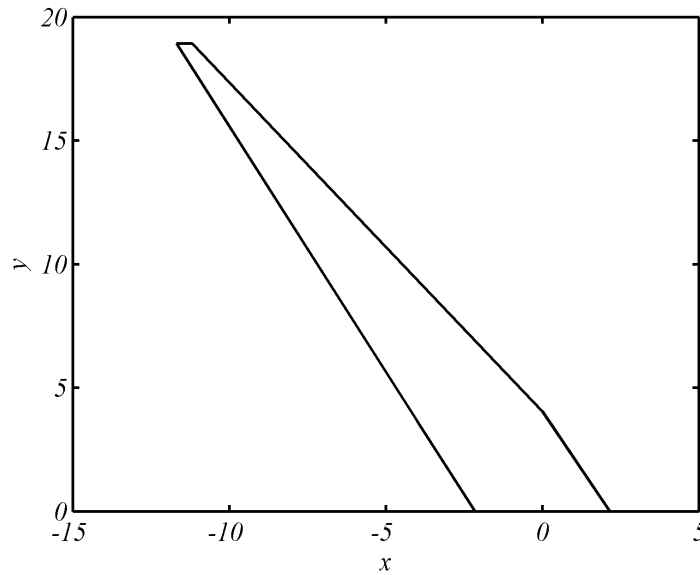


Figure 7-3. Wing box model in the coordinate system that was used for this analysis.

Wing Pressure Distribution

Pippy [203] presented a simplified analysis of the normal pressure load caused by normal acceleration through the use of an elliptical loading model based upon the work of Chklovshi [204] and Lobert [205]. It has been shown that an elliptical loading model approximates the span-wise lift distribution for many taper ratios as shown in Figure 7-4.

The elliptical loading distribution gives the lift w on a wing span s as

$$\frac{y^2}{s^2} + \frac{w^2}{w_0^2} = 1 \quad 7-1$$

where y is the lateral coordinate and w_0 is the maximum pressure applied to the wing.

Note that the wing span s here is the length of a single wing and not the total wing span of a given airplane. The wing span s is assumed to take a value equal to 18.9 m, which corresponds to an aircraft similar to a Boeing 767. Equation 7-1 can be rewritten in terms of the lift w for any span-wise coordinate y as

$$w = \frac{w_0}{s} \sqrt{s^2 - y^2}. \quad 7-2$$

The maximum pressure w_0 applied to the wing can be found from the lift force L which is acting upon the wing. The normalized span-wise pressure distribution with range from 0 to 1 over the chosen airplane wing model is given by

$$p(y) = \frac{1}{s} \sqrt{s^2 - y^2}. \quad 7-3$$

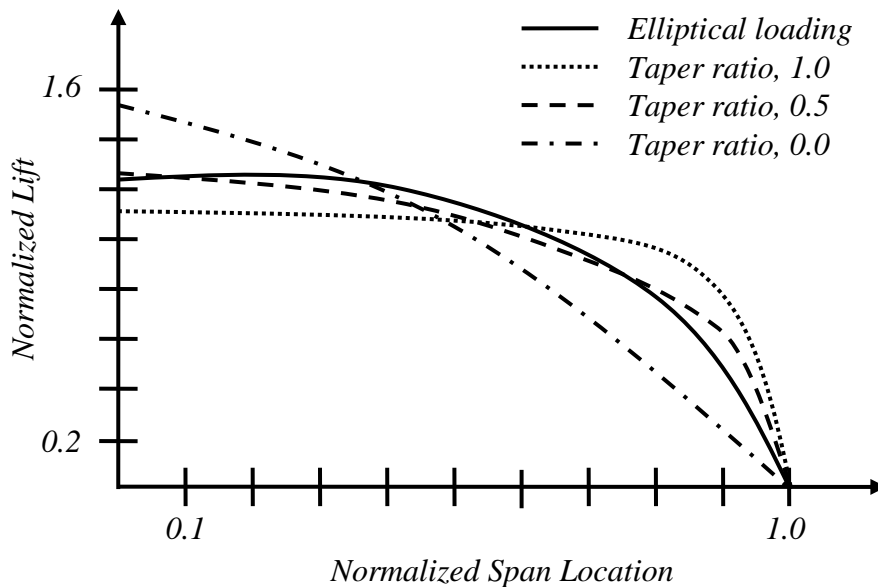


Figure 7-4. Comparison of elliptical loading model for various wing taper ratios.

An estimate of the chord-wise pressure distribution is created based on some theoretical models as shown in Figure 7-5 is made as shown in Figure 7-6. A sixth-order polynomial is used to represent the normalized chord-wise pressure distribution with range from 0 to 1 based upon the normalized coordinate u which has range from 0 to 1. An illustration of a the resulting polynomials is given in Figure 7-7 for several angles of attack, which modifies the point of maximum pressure u_o . The approach taken here will be to do finite element analysis for several angles of attack, and then to fit a surrogate model relating angle of attack to stress components at a point of interest. An expression for the normalized sixth-order polynomial is given as

$$p(u) = a_6u^6 + a_5u^5 + a_4u^4 + a_3u^3 + a_2u^2 + a_1u + a_0 \quad 7-4$$

where the coefficients for various angles of attack are given in Table 7-2. The normalized coordinate u is found as

$$u = \frac{x_L(y) - x}{x_L(y) - x_T(y)} \quad 7-5$$

where x_L and x_T are the coordinates of the leading and trailing edge of the airplane wing as a function of the chord-wise coordinate y . For the coordinate system which was chosen for the finite element model the leading edge follows the relationship

$$x_L(y) = \begin{cases} \frac{y-4.06}{-1.88}, & 0.00 < y < 4.06 \text{ m} \\ \frac{y-4.06}{-1.33}, & 4.06 < y < 18.9 \text{ m} \end{cases} \quad 7-6$$

and the trailing edge is given as

$$x_T(y) = \frac{y+4.3}{-2}. \quad 7-7$$

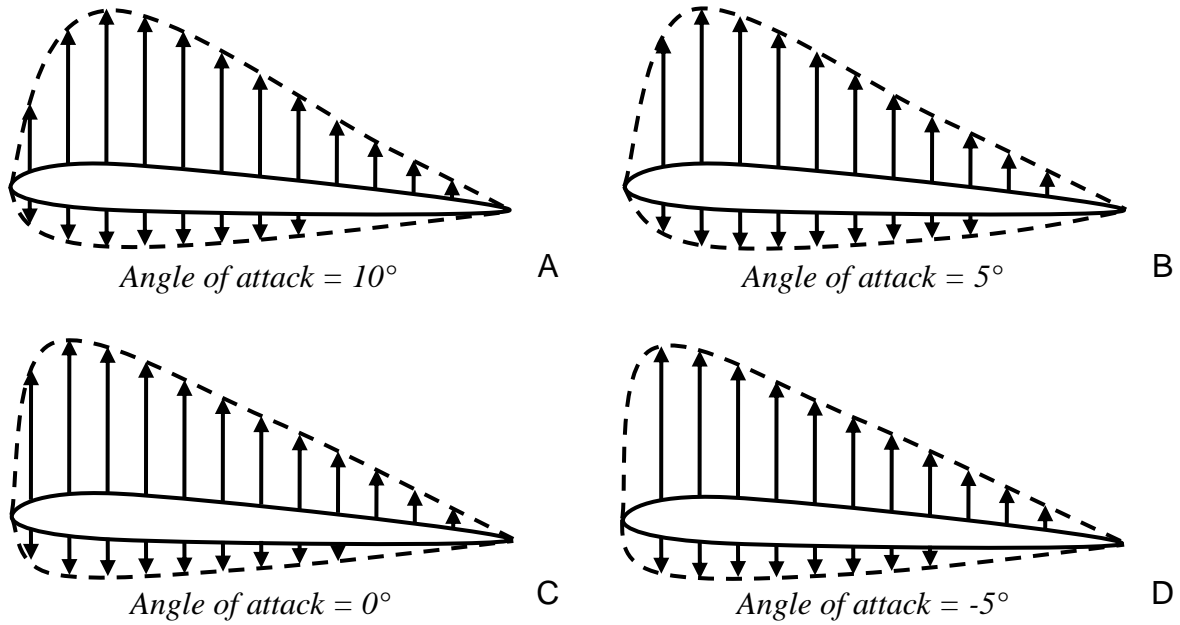


Figure 7-5. Examples of the changing pressure distribution over an airfoil as a function of the angle of attack. A) 10°, B) 5°, C) 0°, D) -5°

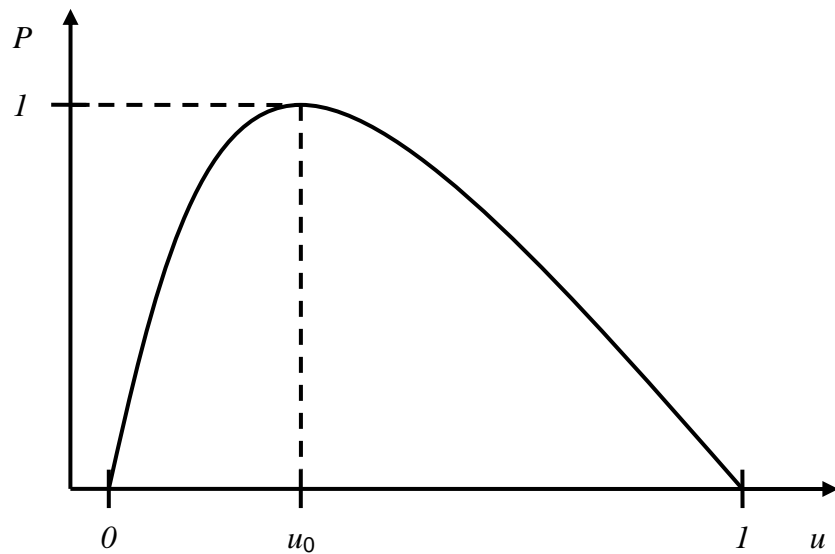


Figure 7-6. Normalized chord-wise coordinates u with maximum pressure coordinate u_0 pressure distribution P .

Table 7-2. The polynomial coefficients for the chord-wise pressure distribution.

Angle of Attack	a_0	a_1	a_2	a_3	a_4	a_5	a_6
-5°	-0.0258	7.73	-20.0	22.0	-11.5	1.83	0.00
0°	-0.0329	9.60	-32.0	49.0	-37.6	11.1	0.00
5°	-0.0253	11.7	-47.0	58.7	-75.4	25.1	0.00
10°	-0.0307	16.0	-90.1	245	-351	252	-71.7

The total pressure distribution for some point (x, y) along the airplane wing is

$$P(x, y) = w_0 p(u) p(y) \quad 7-8$$

where w_0 is the maximum value of the pressure distribution, $p(u)$ is the chord-wise pressure distribution given by Eq. 7-4, and $p(y)$ is the span-wise pressure distribution given by Eq. 7-3. The pressure distribution for $w_0 = 1 \text{ N/m}^2$ is given in Figure 7-8.

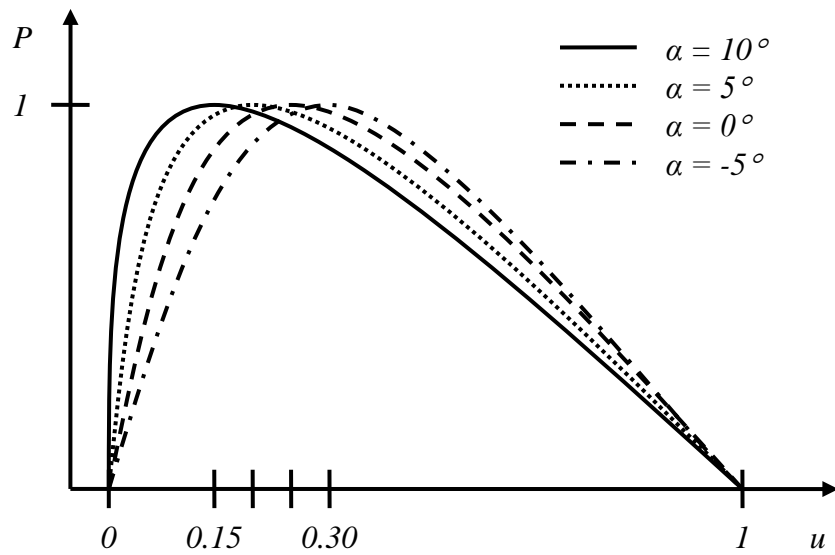


Figure 7-7. Comparison of the changes in the maximum pressure location u_0 and subsequently the resulting pressure profile for some angles of attack α .

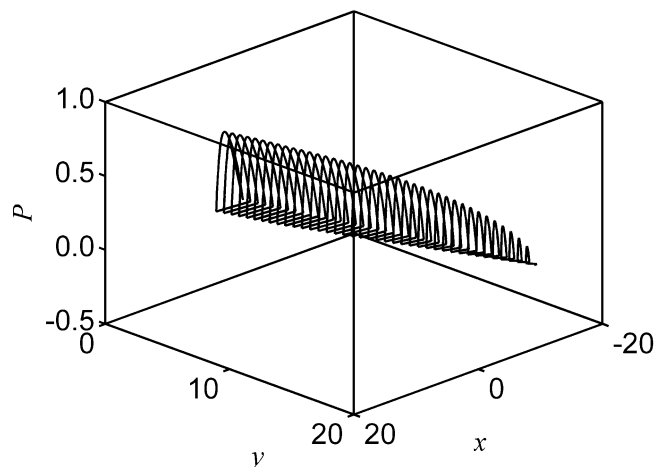


Figure 7-8. The total normalized distribution along the airplane wing for $\alpha = 5^\circ$.

The maximum value of the pressure distribution is found based upon a simple model of the lift force L . From the previous conversion of the roll acceleration to a bank angle θ_B it is possible to find a corresponding bank radius r_B which is given as

$$r_B = \frac{v^2}{g \tan \theta_B} \quad 7-9$$

where v is the scaled airspeed and g is the scaled normal acceleration from the AFRL data. The current mass of the airplane is calculated as

$$m = m_{empty} + m_{fuel} \quad 7-10$$

where m_{empty} is the empty mass of the aircraft and m_{fuel} is the current fuel mass of the aircraft. The lift force L [206] is now given as

$$L = \frac{mv^2}{r_B \sin \theta_B} \quad 7-11$$

The angle of attack of the wing has a direct effect on the lift coefficient C_L as shown in Figure 7-9 [201]. Instead of directly calculating the lift from the lift coefficient, here it was decided to scale the lift L to account for the changing angle of attack α is given by

$$L = \frac{C_L mv^2}{r_B \sin \theta_B} \quad 7-12$$

where C_L for a given angle of attack is found from Figure 7-9. The lift calculated as

$$L = w_0 A_l \quad 7-13$$

where A_l is the total area under the normalized pressure distribution specified in Eq. 7-8. The area of the normalized pressure distribution was found using exact integration for the chord-wise pressure distribution and the rectangle method of integration was used

in the span-wise direction. The span-wise step size Δy was reduced until convergence had been achieved. Using the rectangle method

$$A_i = \int_0^s \int_0^c p(y) p(x) dx dy \approx \sum_{i=1}^n p(y = (i\Delta y - \Delta y)) \Delta y \int_0^c p(x) dx . \quad 7-14$$

where $\Delta y = s/n$. The corresponding area for the normalized pressure distribution as a function of angle of attack are summarized in Table 7-3 where convergence is shown.

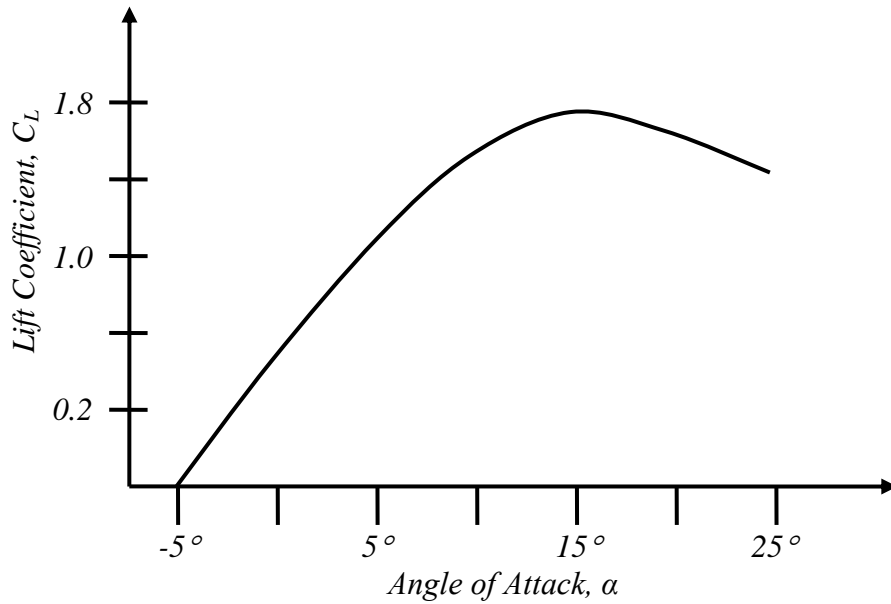


Figure 7-9. Comparison between the angle of attack and the lift coefficient.

Drag acts perpendicular to the span of the aircraft wing as shown in Figure 7-10. The drag on the airplane wing is calculated through the use of the drag coefficient which is approximated as a linear function of the Mach number from 0 to 0.9 Mach [207] as

$$C_D = \frac{M}{4} + 0.13. \quad 7-15$$

This allows for the drag for a given wing to be calculated from the lift as

$$D = L \frac{C_D}{C_L} \quad 7-16$$

and subsequently converted into a uniform pressure with magnitude q_o by dividing by the surface area of the edge where the drag acts A_d as

$$D = q_o A_d . \quad 7-17$$

Equation 7-16 is used as the lift and drag can be calculated from the same equation by interchanging the lift and drag coefficient [208].

Table 7-3. Area under the normalized pressure distribution for some angles of attack.

Angle of Attack	Number of Integration Steps, N	Pressure Distribution Area, A_l
10°	1000	37.08 m ²
	2000	37.06 m ²
	5000	37.05 m ²
	10000	37.05 m ²
5°	1000	39.24 m ²
	2000	39.22 m ²
	5000	39.21 m ²
	10000	39.21 m ²
0°	1000	41.28 m ²
	2000	41.26 m ²
	5000	41.25 m ²
	10000	41.25 m ²
-5°	1000	43.14 m ²
	2000	43.12 m ²
	5000	43.11 m ²
	10000	43.11 m ²

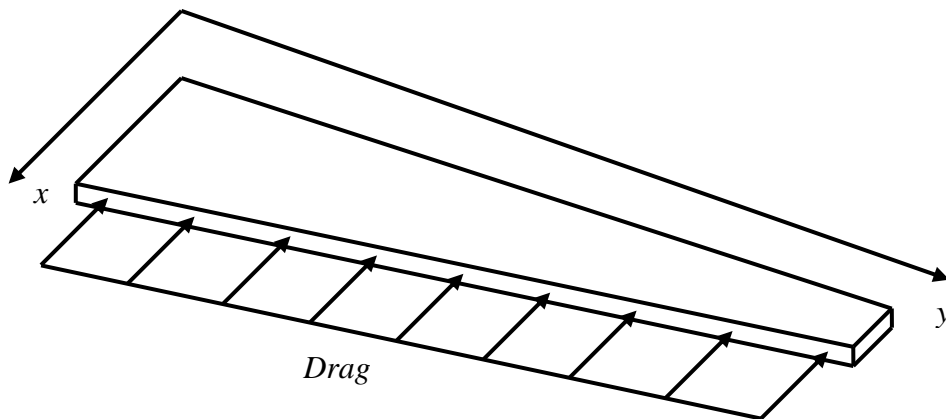


Figure 7-10. The direction of the uniform pressure distribution defined by the drag. (Note that the drag is independent of the angle of attack, unlike the lift model).

Finite Element Stress Analysis of Airplane Wing

Linear elastic finite element analysis was performed on the airplane wing box geometry which was originally created by Pippy [197] within Abaqus[®]. The boundary conditions were created by connecting the edge of the wing box at $x = 0$ to the center of gravity of the wing (0.43, -0.86, 0) by rigid elements and fixing all degrees of freedom at the reference point at the center of gravity. Five loading conditions were considered here, the chord-wise lift distribution with angles of attack of -5° , 0° , 5° , and 10° as well as the drag distribution. All cases were considered with unit magnitude pressure. The two-dimensional stresses were taken from each analysis at the point (-4.32, 7.42, 0) where the crack is located in the panel. These values are given in Table 7-4 and were used for the stress calculation for each of the 19 unique flight profiles provided by the normalized data from the AFRL.

Table 7-4. The stress components for various angles of attack used in the lift and drag pressure distributions.

Analysis	σ_{xx}	σ_{yy}	σ_{xy}
Drag	22.3	-33.4	32.2
Lift, $\alpha = -5^\circ$	135	481	300
Lift, $\alpha = 0^\circ$	134	483	398
Lift, $\alpha = 5^\circ$	133	484	296
Lift, $\alpha = 10^\circ$	131	480	291

Surrogate Models for Lift Coefficient, Stress Components, and Surface Area of Pressure Distribution

Several surrogate models are used in the stress analysis of the airplane wing box. A surrogate model is used to allow for the lift coefficient to be evaluated as a function of the angle of attack α which follows Figure 7-9. Another surrogate model is used to fit the surface area of the pressure distribution given by Table 7-3 as a function of the angle of attack α . For each case, a kriging surrogate as described in Chapter 5 is used.

A kriging surrogate model is fit to each stress component as a function of angle of attack for the chord-wise lift distribution in order to allow for the stress to be evaluated for any value of the angle of attack α from the values in Table 7-4. The magnitude of the lift and drag distributions are given by w_o in Eq. 7-13 and q_o in Eq. 7-17. Therefore, the stress for a given set of scaled flight data can be calculated as

$$\begin{aligned}\sigma_{xx} &= w_0 \sigma_{xx}^L(\alpha) + q_0 \sigma_{xx}^D \\ \sigma_{yy} &= w_0 \sigma_{yy}^L(\alpha) + q_0 \sigma_{yy}^D \\ \sigma_{xy} &= w_0 \sigma_{xy}^L(\alpha) + q_0 \sigma_{xy}^D\end{aligned}\tag{7-18}$$

where $\sigma_{xx}^L(\alpha)$, $\sigma_{yy}^L(\alpha)$, and $\sigma_{xy}^L(\alpha)$ are the stress components from the kriging surrogate model for the lift pressure distribution and σ_{xx}^D , σ_{yy}^D , and σ_{xy}^D are the stress components from the drag pressure distribution. The resulting stresses at the crack location and the stresses normalized by σ_{yy} are given in Figure 7-11 for Flight ID 152. Note that the normalized stresses are not constant in Figure 7-11. This presents a challenge in the fatigue analysis of this structure as the crack growth direction will change with each data point. This means no increment of crack growth across many cycles can be used. The stresses and normalized stresses for all 19 flights are given in Appendix D. A flowchart of the method for the conversion of the normalized flight data into biaxial stress history is summarized as:

1. Perform 5 finite element analysis; four for the chord-wise pressure distribution as a function of angle of attack as shown in Figure 7-7 and Figure 7-8 ,and one for the drag pressure distribution as shown in Figure 7-10 to find the biaxial stresses at a point of interest of the wing box.
2. For each normalized variable, find the conversion of the maximum and minimum normalized data point to the maximum and minimum scaled value as given in Table 7-1. Then find and use the conversion to create scaled data points from the normalized data points.

3. Create surrogate models for the lift coefficient, area under the chord-wise pressure distribution, and the biaxial stresses as a function of the angle of attack.
4. Follow Eq. 7-9 to Eq. 7-13 for the calculation of w_o and Eq. 7-15 to Eq. 7-17 for the calculation of q_o . This will use the surrogate models for the lift coefficient and area under the chord-wise pressure distribution.
5. Calculate the biaxial stresses from the values of w_o , q_o , and the surrogate models for the biaxial stresses as a function of the angle of attack.

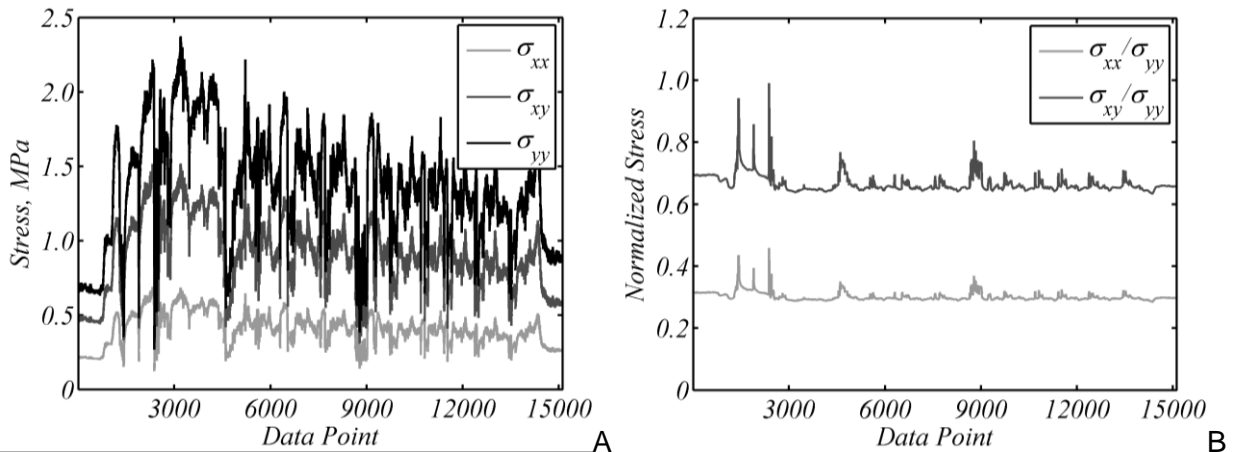


Figure 7-11. The stress histories for the two-dimensional stress components for Flight ID 152. A) Bi-axial stress components, B) Normalized stress components.

Analysis of Cracked Plate Subjected to Variable Amplitude Multi-axial Load History

Due to the fact that the stresses in this problem are non-proportional as seen in Figure 7-11 as a function of the history (e.g. stress ratios are non-constant) this problem creates challenges for approximating the fatigue crack growth of the problem. As the stress history is non-proportional, the ratio of K_I to K_{II} is non-constant, which implies that the angle of crack growth will change as a function of the loading history. As the path of crack growth is unknown, it is unclear how to select an analytical relationship between the crack size and stress intensity factor which will correctly consider the unknown crack path. Therefore, it is not possible to use a finite crack growth increment Δa , as the crack growth direction cannot be assumed to be constant over a range of

elapsed cycles ΔN . Therefore, the only choice is to choose the case where the cyclic history is followed.

Before the fatigue analysis can be started, first the biaxial stresses for each of the 19 flights must be converted into equivalent cyclic stresses. This is done according to the method outlined in Chapter 4 where an equivalent stress is calculated from the biaxial stress components. The rainflow counting algorithm is used to find the cycles from the equivalent stress history. The identified stress history is then superimposed back onto the biaxial stress data, resulting in cyclic biaxial stresses which can be applied to a plate and be used with a fatigue crack growth model. An example of the equivalent stress for Flight ID 152 and the identified equivalent cyclic loading history is shown in Figure 7-12. The results of the conversion from normalized data points to stress cycles for each of the 19 flights is given in Table 7-5.

There is an uneven number of data points can be explained as the rainflow counting method being interested in the extrema for the given data points. Not all data points which were provided by the AFRL correspond to an extrema. The conversion from biaxial stress components to an equivalent single stress can also result a suppression of the number of extrema present in the resulting rainflow counting algorithm. Two function evaluations are required for each identified cycle as the ratio of the biaxial stresses changes between the maximum and minimum data point for each cycle, and the calculation of the mixed-mode stress intensity factors without two function evaluations is not possible with sufficient accuracy.

The initial geometry was that of an edge crack of initial crack size of 5 mm in a square finite plate with sides of length 0.1 m as shown in Figure 7-13. Note that a

geometry with does not necessarily agree with that of an actual wingbox panel at the specified location is used here for demonstration purposes.. The material was assumed to be aluminum 7075-T6 where the material properties and model constants are: Young's modulus of 70 GPa, Poisson's ratio of 0.3, yield stress of 520 MPa, Mode I threshold stress intensity factor of $2.2 \text{ MPa}\sqrt{\text{m}}$, Mode II threshold stress intensity factor of $1.0 \text{ MPa}\sqrt{\text{m}}$, Paris model constant of $6.85 \cdot 10^{-11}$, Paris model exponent of 3.21, shaping parameters n , β , and β_1 of 0.30, 0.70, and 0.84 respectively [27, 133]. To encourage consistent, small scale crack growth the stresses calculated from the analysis of the wing box were scaled linearly by a factor of 10, which resulted in crack growth between 10^{-9} and 10^{-5} cycles for most of the cycles. In order to make the solution of this problem more affordable, the proposed exact reanalysis algorithm of Chapter 6 is used for the 74,014 required function evaluations.

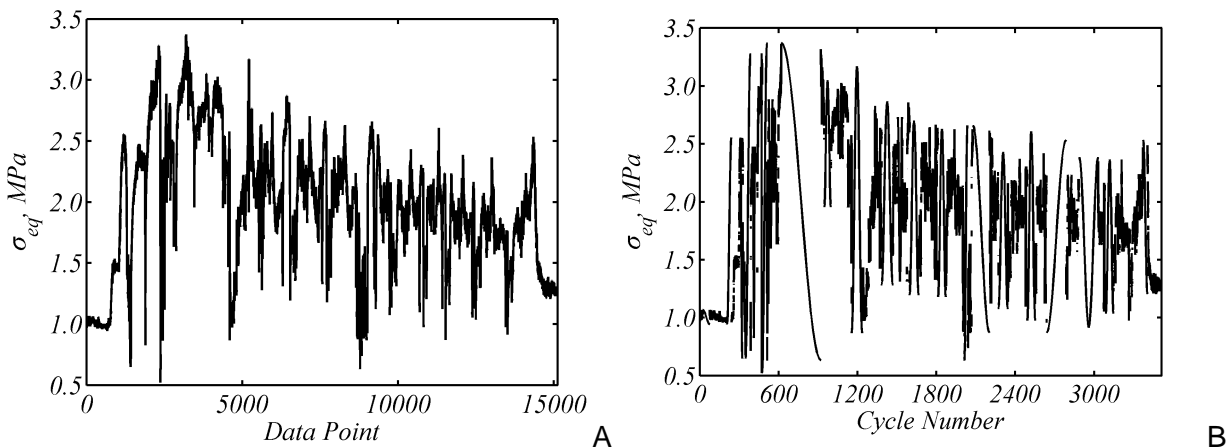


Figure 7-12. Equivalent stress and identified cycles from equivalent stress for Flight ID 152. A) Equivalent stress, B) Identified cycles.

A study was performed on the initial edge crack geometry to ensure that the mixed-mode stress intensity factors converged according the mesh density. This mesh was found to be that of a structured mesh of square elements with sides of length 1/200 m. The average computer time for each function evaluation was approximately 2.3

seconds with the proposed exact reanalysis algorithm, which corresponds to about 2 days for a single analysis. As the computational cost without reanalysis is too high for a complete analysis, 100 iterations without the reanalysis algorithm were performed such that an estimate of the total computer time without the reanalysis algorithm could be approximated for the purposes of comparison. It was found that the mean computer time for a cycle for these 100 iterations without reanalysis was about 20 seconds, which would correspond to about 17 days for a proposed fatigue analysis. Note that as crack growth occurs and more degrees of freedom are added to the system of equations, the cost of assembly, factorization, and solving will increase. Due to this, it is very possible that the true computer time required would be in excess of the predicted time of 17 days.

Table 7-5. Summary of the AFRL data, the number of cycles identified, and the number of function evaluations for each Flight ID.

Flight ID	Number of Data Point	Number of Identified Cycles	Function Evaluations
2	11,158	1,780	3,560
8	12,893	2,207	4,414
10	6,050	1,409	2,818
12	9,628	1,838	3,676
16	7,544	1,311	2,622
18	7,422	1,126	2,252
22	4,057	797	1,594
26	10,124	1,895	3,790
138	6,038	1,270	2,540
140	10,427	2,275	4,550
146	10,431	2,266	4,532
148	9,766	2,290	4,580
150	16,038	3,415	6,830
152	15,120	3,470	6,940
154	11,044	2,754	5,508
156	5,631	1,025	2,050
159	7,616	1,669	3,338
161	9,623	2,180	4,360
163	9,978	2,030	4,060
Total	180,588	37,007	74,014

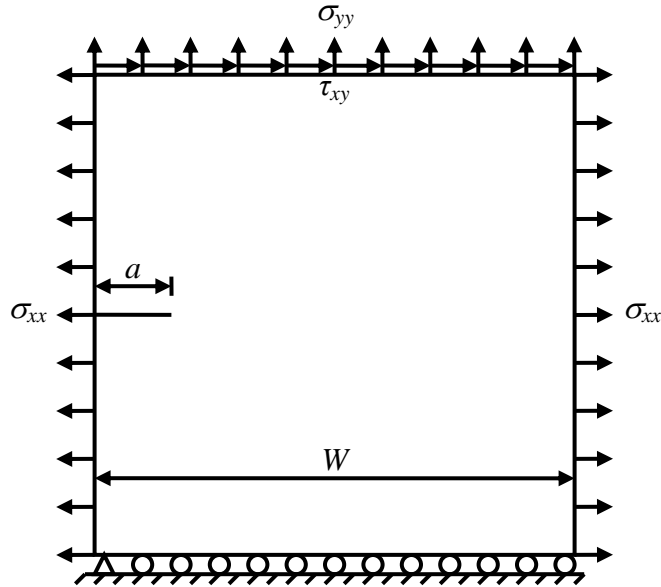


Figure 7-13. The boundary conditions and applied bi-axial stresses for the analysis of a panel on an airplane wing box subjected to variable amplitude fatigue.

The initial and final crack paths from the analysis are given in Figure 7-14. For a more detailed view of the crack propagation path, refer to Figure 7-15. Note that initially, the crack tip begins to move down and to the right. This agrees with the observation that the largest stress component is σ_{yy} , followed by σ_{xy} . With the loading specified in Figure 7-13, the resultant stress would be approximately perpendicular to the initial direction of crack growth. For the initial crack σ_{xx} has no effect on either the stress intensity factors or the crack propagation path. The subsequent crack propagation path represents a more difficult challenge to analyze in detail as the changing orientation of the crack tip represents a changing crack tip coordinate system and resultant stress acting at the crack tip in the Mode I and II. The general trend is to move in a horizontal motion, which is consistent with σ_{yy} being the largest applied stress.

The crack length as a function of the cycle number is given in Figure 7-16 where the grey lines denote the bounds associated with each unique flight. One of the

observations from these plots is that most of the crack growth occurs early in the life of the wing panel. In fact, of the 37,007 loading cycles, crack growth occurs in only about 2,500 of these cycles. This can be explained partially with the assistance of Figure 7-17, which gives the Mode I and II stress intensity factor ranges as a function of cycle number. Recall, that the threshold Mode I and II stress intensity factor ranges for aluminum were identified as taking values of $2.2 \text{ MPa}\sqrt{\text{m}}$ and $1.0 \text{ MPa}\sqrt{\text{m}}$. From Figure 7-17 it is clear that rarely does the Mode I stress intensity factor range exceed this value. Furthermore, it can be noticed that early in the panel's life, the Mode I stress intensity factor range tends to take larger values than later in the panels life. Later in the lift of the panel, when the Mode II stress intensity range takes larger values, the Mode I values are at a minimum, reducing the net effect of increased ΔK_{II} . It should also be recalled that the predicted stresses at the crack location were increased by a factor of 10 to encourage an increased amount of crack growth throughout the panel's life. In a real application it is unlikely that this level of crack growth would occur at such an accelerated rate.

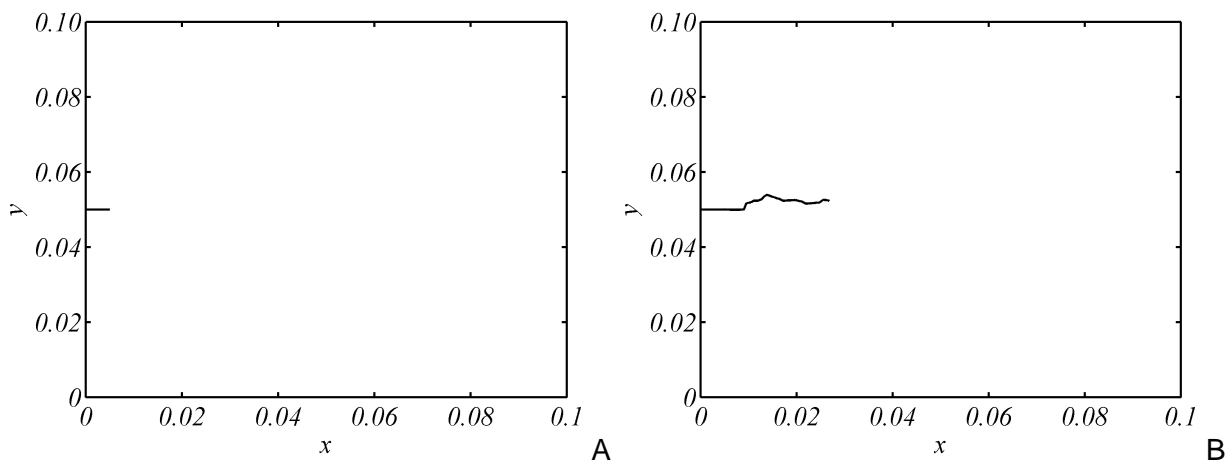


Figure 7-14. The initial and final crack geometries from the stresses identified through the normalized flight data from the AFRL. A) Initial crack, B) final crack

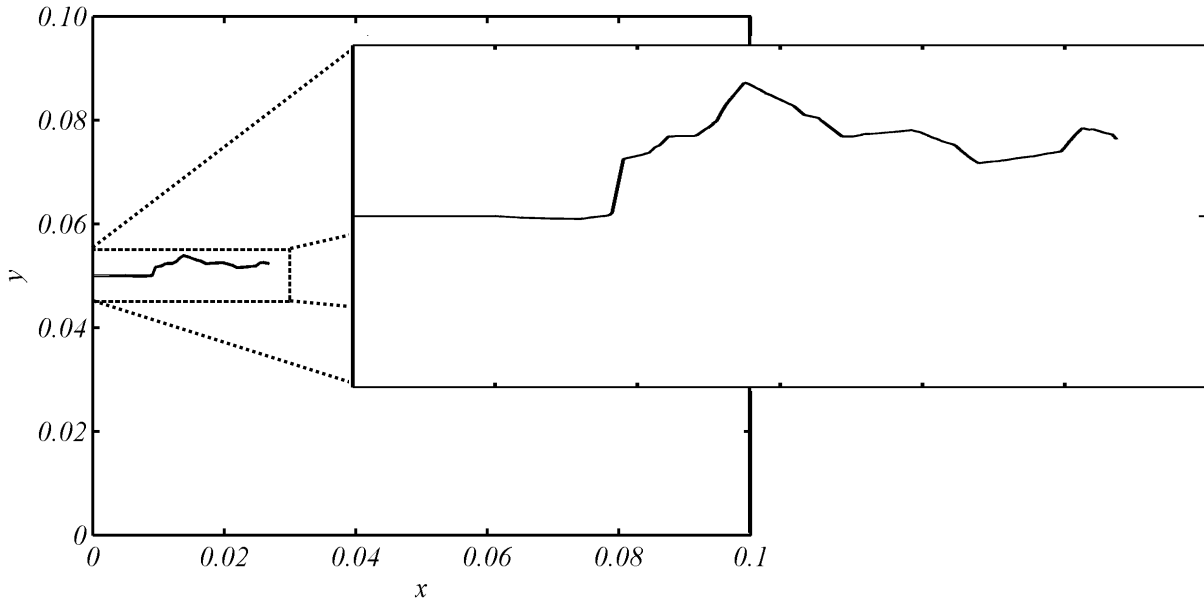


Figure 7-15. Close-up view of the final crack geometry from the stresses identified through the normalized flight data from the AFRL.

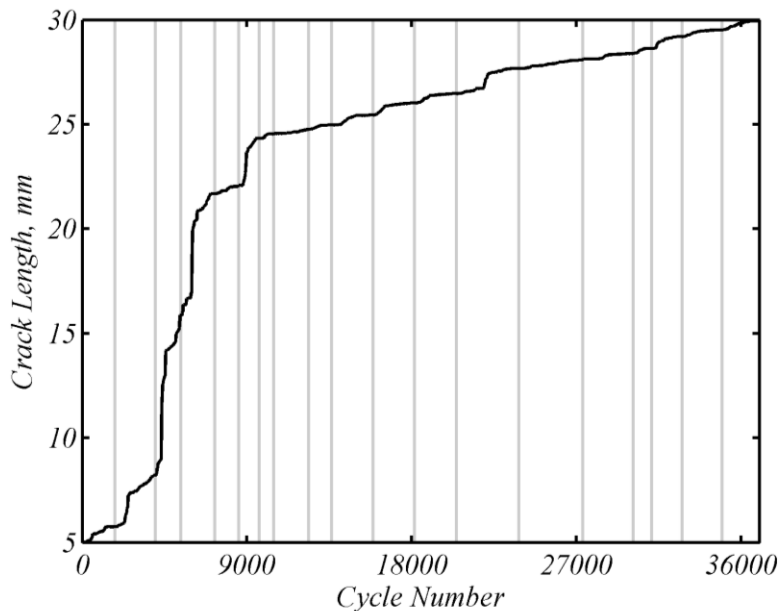


Figure 7-16. Comparison of the crack length as a function of the cycle number for the 19 flights from the normalized AFRL data.

Another cause for the reduced amount of crack growth later in the panels life may be considered as a function of the M_R and M_P terms in the modified Paris model used in the analysis. The stress ratio R will increase the value of M_R , and therefore, accelerate crack growth. It can easily be seen in Figure 7-17 that the value of R will be

take a maximum value early in the life of the panel. An observation about what may be perceived as jumps in the crack length around cycle numbers 3500, 4000, 6000, and 9000. Each of these instances has a corresponding peak in the ΔK_I curve. This peak will act as an overload, increasing the plasticity at the crack tip and slowing crack growth until the point in time when a load is applied which results in the creation of a larger plastic zone. As most of the peaks in the ΔK_I curve exist early in the life of the panel, the crack growth later in the panel's life is retarded as there are few instances where the applied load to exceed the previously developed crack tip plasticity.

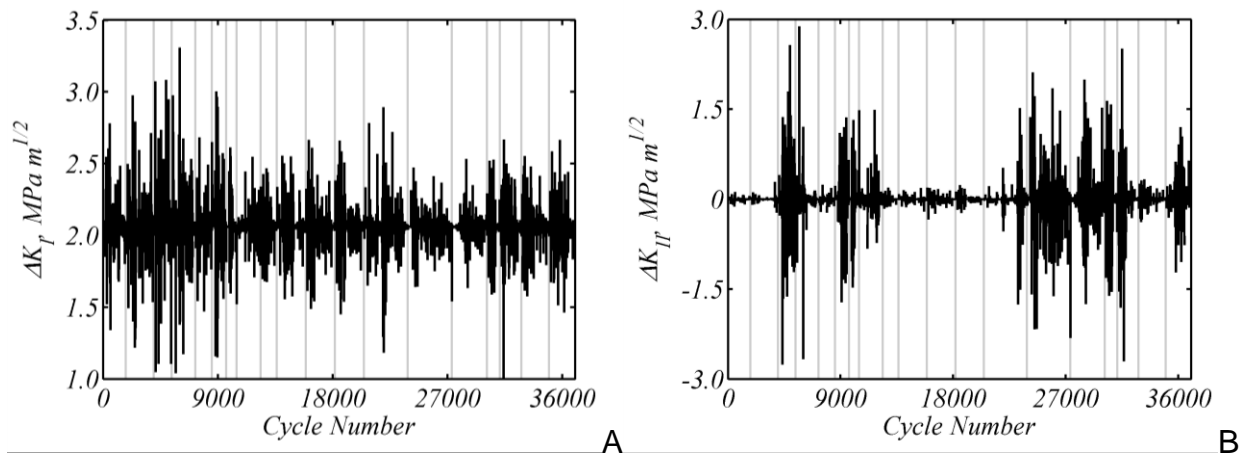


Figure 7-17. The Mode I and Mode II stress intensity factor ranges for the 37,007 cycles. A) Mode I stress intensity factor range, B) Mode II stress intensity factor range.

Summary

The fatigue analysis of an airplane wing subjected to mixed-mode variable amplitude loading was conducted through the use of a simple stress model of an airplane wing box in coordination with normalized flight data provided by the AFRL. First, the normalized flight data was scaled to approximate values related to a commercial aircraft flight and a Boeing 767 in particular. Then, the two-dimensional stress history from the 180,588 normalized data points was calculated at a particular

point of interest along an airplane wing. Next, an equivalent stress was calculated and the rainflow counting algorithm was used in order to convert the stress data into cyclic loading data consisting of 37,007 cycles which could be used in a fatigue crack growth model. These cycles were then superimposed onto the σ_{xx} , σ_{yy} , and σ_{xy} stress histories.

Due to the non-proportional loading represented by the stress histories, fatigue modeling techniques which assume multiple elapsed cycles for each simulation cannot be used to solve this problem. Instead, each loading cycle was modeled using the exact XFEM reanalysis method based upon the direct modification of an existing Cholesky factorization. It was estimated that the combination of savings in assembly and factorization time for this problem resulted in the problem being solved in about 86% of the time that would be needed for the traditional solution procedure. At each cycle, the crack growth direction was calculated according to the maximum circumferential stress criterion. The fatigue crack growth model which was used was a modified version of the classical Paris model which also considers the effects of the threshold stress intensity factor, stress ratio R , and load interactions as a function of the changes in plasticity as a result of overloads and underloads. The mixed-mode stress intensity factors are converted into a single equivalent stress intensity factor for use in the modified Paris model through the use of the methods introduced by Liu.

Over the life of the panel, crack growth occurred in about 2,500 of the 37,000 modeled cycles. However, this is not information which would have been available before the analysis was run as no information about the amount or direction of crack growth was known before modeling the response of the panel to the biaxial stresses.

Crack growth in a limited number of cycles was caused by a combination of the stress intensity factor ranges rarely exceeding the threshold values and the crack tip plasticity model in the modified Paris model which retarded crack growth. It was observed that the stress intensity factor history for the crack showed that early in the panel's life, greater maximum values of ΔK_I and ΔK_{II} were often realized. This resulted in an increased amount of crack growth early in the life of the panel. Later in the panels life, crack growth occurred more slowly and in a more controlled fashion, most likely due to both the lower peak values of the stress intensity factor ranges as well as the crack tip plasticity which had been developed earlier in the panels life.

CHAPTER 8 CONCLUSIONS AND FUTURE WORK

Conclusions

Fatigue is the process by which materials fail due to repeated loading well below the levels that they would fail under static loading conditions. It is not uncommon for 10^4 to 10^8 cycles to be needed for failure to occur. This presents a challenge for computational simulation as this number of cycles is not feasible for modeling in a finite element environment. With classical finite element methods, the mesh corresponds to the domain of interest, which means that the mesh must be recreated locally around the crack tip each time crack growth occurs. Fatigue crack growth has been one of the leading causes of aircraft accidents throughout history and still causes incidents today. Better computational tools for the modeling of fatigue crack growth will help to reduce the risk of accidents from the initiation and propagation of a crack. The goal of this work is to create strategies such that fatigue crack growth can be numerically modeled with greatly reduced computational requirements.

The challenges associated with mesh generation in the classical finite element method are addressed through the use of the extended finite element method (XFEM). In the XFEM, discontinuities are represented independent of the finite element mesh. Even when the challenges associated with mesh generation can be avoided; there is still a large number of function evaluations required in modeling fatigue crack growth. The fundamental structure of XFEM can be exploited to further reduce the cost of the repeated function evaluations necessary for modeling fatigue crack growth. When crack growth occurs in the XFEM, only a small portion of the finite element stiffness matrix changes as crack growth occurs. These small changes in the finite element stiffness

matrix are exploited through the direct modification of an existing Cholesky factorization through the use of row add and row delete operations. The approximate fill-reducing ordering for this matrix which has changing, but unknown connectivity is found through the use of a dummy stiffness matrix.

Surrogate models enable the use of higher-order numerical methods in the integration of a fatigue crack growth model for both the magnitude and direction of crack growth with the use of a single expensive finite element simulation. Test cases show that the use of kriging to replace expensive function evaluations offers comparable accuracy to classical numerical techniques with significantly fewer expensive function evaluations. A variable integration step size algorithm is also introduced which uses the difference between the surrogate prediction and the finite element simulations to dynamically change the integration step size to attempt to achieve some target accuracy for each simulation. In the case that the particular iteration has accuracy less than the target error, then the integration step size is increased. Similarly, for an iteration where the accuracy is greater than the target error, the integration step size is decreased.

Finally, the XFEM exact reanalysis algorithm is used to predict fatigue crack growth due to variable amplitude biaxial loading in an airplane wing box. Normalized data from the Air Force research laboratory was scaled and then used to create a stress history for the airplane wing in terms of the scaled data. The rainflow counting algorithm was used to convert the discrete stress history into a cyclic stress history which was used as the input for the fatigue analysis. This is a first step towards realizing fatigue

crack growth from service load histories for variable amplitude multi-axial stress histories.

Future Work

Future Development of MXFEM

Additional enrichment functions could be implemented for cracks or inclusions, giving the user more options for learning about the XFEM, of particular interest may be allowing only the Heaviside enrichment for a crack and neglecting the crack tip terms, as this comparison is often made in the literature. Contact between crack faces could be implemented to prevent for the crack surfaces from entering the materials as would currently occur for compressive loading. Modifying the definition of where boundary conditions and loading are applied instead of requiring the direct modification of files other than the input file for the given loading conditions may facilitate the ease of use for simulations. Removing the limitation for square elements and a rectangular domain, perhaps with the option to import the nodal coordinates and element connectivity information from a text file which would allow for complex geometries to be considered.

Possible Application for the Exact XFEM Reanalysis Algorithm

An example of a crack growth problem which could benefit from an application of the proposed exact XFEM reanalysis algorithm is that of elastic crack growth between dissimilar materials. Consider the case of a crack which is propagating towards a material interface as shown in Figure 8-1. Upon reaching the interface the crack may either be arrested, penetrate into the interface, propagate along the interface or branch and propagate along the interface [209]. The challenge in modeling this problem is that the crack propagation behavior is a function of the two materials which are considered as well as the angle at which the crack approaches the interface. There is no closed

form solution for how the crack will behave upon reaching the interface, and one possible solution procedure would involve the solution of an optimization problem to find the path with the greatest energy release rate from the available possible propagation paths.

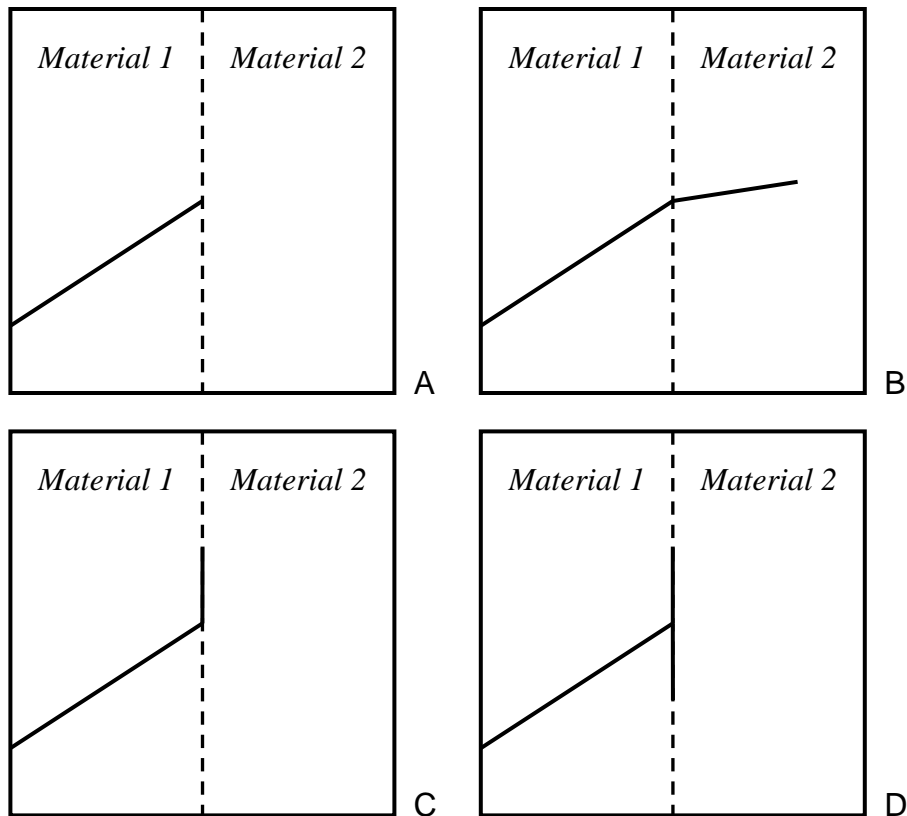


Figure 8-1. Possible crack propagation paths between dissimilar materials. A) Arrest, B) Penetration, C) Propagate along interface, D) Branch along interface.

The proposed exact XFEM reanalysis algorithm could be used to create an optimization problem where the penetration or growth patterns along the material interface are considered. The angle of penetration which maximizes the energy release rate could be compared to the energy release rates for growth along the interface or crack branching at the interface with the maximum energy release rate among these options being the most likely crack growth path. This energy release rate can then be converted to a stress intensity value and compared with the fracture toughness of the

material interface or material into which the crack is penetrating. If the stress intensity is not sufficiently large to cause fracture, then the case of a crack arresting at the interface may be observed. The major modifications which need to be considered for this problem with the MXFEM code include: implementation and verification of bi-material [85] and branching [89] crack enrichment functions, the implementation of the auxiliary stress and displacement states for the bi-material crack [85], and the formulation of the optimization problem to determine the direction of maximum energy release rate. The analysis may be verified against the work of He [209, 210] and Zhang [211]. If this implementation was completed it would be possible to further extend this approach to interface layers [212] and laminates [213].

Possible Applications for Surrogate Integration

An example of a problem which may benefit from the use of the proposed surrogate integration method is that of wear occurring in the joint of multibody systems due to contact. The Archard wear model [214] is commonly used to predict the amount of wear such that

$$\frac{dh}{ds} = kp(s) \quad 8-1$$

where h is the wear depth, k is a wear constant, p is the contact pressure between the two bodies in contact, and s is the sliding distance between the two bodies. Note that this problem is quite similar in form to the classical Paris model where a correlation could be made where $C = k$, $\Delta K = p(s)$, and $m = 1$. Finite element simulations with a contact model are commonly used to calculate the contact pressure and sliding distance [215], while the wear constant k usually is determined from experimental data.

Wear is a slow process which occurs over a large number of iterations, similar to fatigue. In this way, it would be too expensive to perform a finite element simulation during each loading cycle to find p and s , calculate the wear depth, update the mesh, and then perform the next analysis. Instead, a forward Euler approach [215] is often used to approximate the wear over a number of elapsed cycles ΔN according to a single finite element simulation for p and s as

$$\Delta h = kp(s)\Delta N . \quad 8-2$$

This is the same basic problem which was considered in the case of modeling fatigue crack growth and it is possible that the use of kriging extrapolation and/or the variable step size approach could be applied to a wear analysis and result in a better approximation of the amount of total wear Δh over a number of elapsed cycles ΔN with some modifications to account for the differences between the two problems.

APPENDIX A
MXFEM BENCHMARK PROBLEMS

XFEM Enrichments

Center Crack in a Finite Plate

The first problem considered in the verification of the MATLAB[®] XFEM code is that of a center crack in a finite plate. The geometry and specifications for the values of a and W is shown in Figure A-1. The material properties used in the analysis were chosen to be Young's modulus of 10 MPa and Poisson's ratio of 0.3. The full domain was a plate with height 10 m and width 6 m with a center crack of length 2 m. The applied stress was 1 Pa. Square plane strain quadrilateral elements with a structured mesh were used. Both a full and half model were considered based on the symmetry in the problem.

The theoretical stress intensity factor for a center crack in a finite plate [20] is

$$K_I^t = \sqrt{\sec\left(\frac{\pi\lambda}{2}\right)\left(1 - \frac{\lambda^2}{40} + \frac{3\lambda^4}{50}\right)}\sigma\sqrt{\pi a} \quad \text{A-1}$$

where $\lambda = a/W$, σ is the applied stress, and a is the half crack length. A comparison of the convergence as a function of the average element size h is given in Table A-1 where the normalized stress intensity factors are given as

$$K_I^n = \frac{K_I^{XFEM}}{K_I^t} \quad \text{A-2}$$

where K_I^t is given by Eq. A-1 and K_I^{XFEM} is the value calculated by the XFEM analysis using the domain form of the contour integral. The results for the analysis of the full and half model are given in Table A-1. From this table it can be noticed that an accurate solution is achieved for a mesh with characteristic element size of 1/20. There is limited

improvement with increased mesh density in the vicinity of the crack tip. It can be noticed that there is a difference between the full and half model created by symmetry. These changes are most likely due to the slightly different boundary conditions used for the two cases. In the case of a full center crack, the midplane where the crack is located is restricted from moving the vertical direction and the midpoint of the plate is fixed. For the half model, the left edge are given rollers in the y -direction and the bottom left hand corner is fixed. The XFEM model shows good accuracy without any of the cumbersome challenges associated with solving a similar problem in the traditional FEM framework.

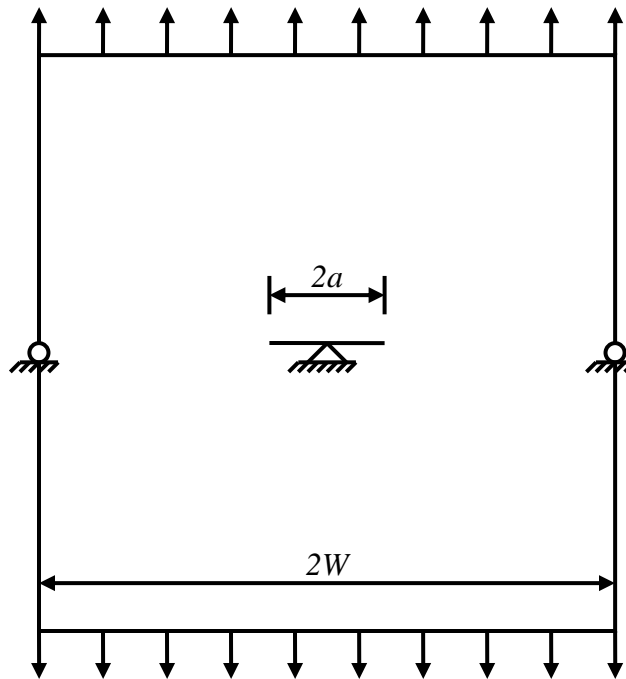


Figure A-1. Representative geometry for a center crack in a finite plate.

Table A-1. Convergence of normalized stress intensity factors for a full and half model for a center crack in a finite plate.

h	K_I^n Full, Right Tip	K_I^n Full, Left Tip	K_I^n Half, Right Tip
1/5	0.954	0.952	0.962
1/10	0.977	0.977	0.967
1/20	0.989	0.989	0.980
1/40	0.996	0.996	0.990
1/80	0.999	0.999	0.996

Edge Crack in a Finite Plate

The next problem considered in the verification of the MATLAB[®] XFEM code is that of an edge crack in a finite plate. The geometry and specifications for the values of a and W is shown in Figure A-2. The material properties used in the analysis were chosen to be Young's modulus of 10 MPa and Poisson's ratio of 0.3. The full domain was a plate with height 6 m and width 3 m with a center crack of length 1 m. The applied stress was 1 Pa. Square plane strain quadrilateral elements with a structured mesh were used.

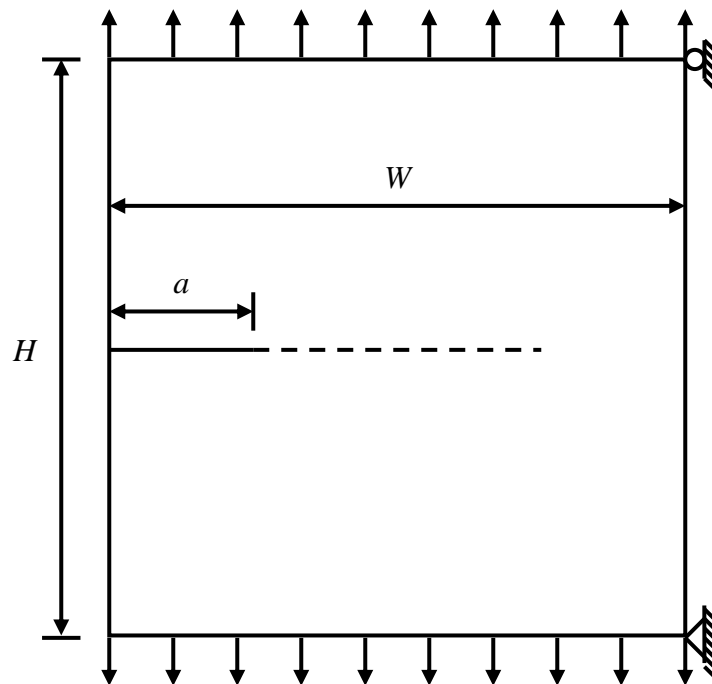


Figure A-2. Representative geometry for an edge crack in a finite plate

The theoretical stress intensity factor for an edge crack in a finite plate [20] is

$$K_I^t = (1.12 - 0.231\lambda + 10.55\lambda^2 - 21.72\lambda^3 + 30.39\lambda^4) \sigma \sqrt{\pi a} \quad \text{A-3}$$

where $\lambda = a/W$, σ is the applied stress, and a is the characteristic crack length. A comparison of the convergence as a function of the average element size h is given in Table A-2 where the normalized stress intensity factors are given by Eq. A-2. From this

table it can be noticed that an accurate solution is achieved for a mesh with characteristic element size of 1/10. There is limited improvement with increased mesh density in the vicinity of the crack tip. This represents a decreased mesh density to be needed for a solution of comparable accuracy to the case of a center crack in a finite plate. This can be explained by the value of the Mode I stress intensity factor in this case taking a larger value than in the previous example, which makes the normalization less sensitive to small differences between the theoretical and calculated values.

Table A-2. Convergence of normalized stress intensity factors for an edge crack in a finite plate.

h	K_I^n
1/5	0.884
1/10	0.991
1/20	1.001
1/40	1.002
1/80	1.002

Inclined Edge Crack in a Finite Plate

The case of an inclined edge crack in a finite plate benchmark problem is used to show accuracy in mixed-mode problems. A figure of the geometry is given in Figure A-3. The material properties used in the analysis were chosen to be Young's modulus of 10 MPa and Poisson's ratio of 0.3. The full domain was a plate with height 2 m and width 1 m with an edge crack from (0,1) to (0.4,1.4). The applied stress was 1 Pa. Square plane strain quadrilateral elements with a structured mesh were used.

A comparison of the convergence as a function of the average element size h is given in Figure A-3 where the normalized stress intensity factors are given by Eq. A-2. The reference solution [216] which was used for comparison is $K_I' = 1.927$ and $K_{II}' = 0.819$. This reference solution is commonly used in the XFEM literature [96] and is a solution with accepted accuracy. convergence of the Mode I and Mode II stress intensity

factors for this problem are comparable to that for the center crack in a finite plate problem.

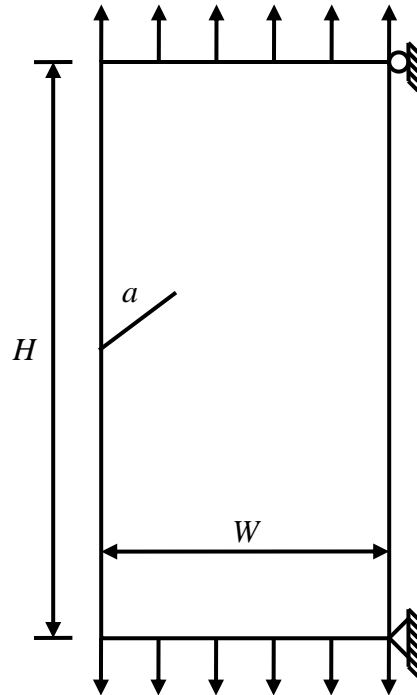


Figure A-3. Representative geometry for an inclined edge crack in a finite plate.

Table A-3. Convergence of normalized stress intensity factors for an inclined edge crack in a finite plate.

h	K_I^n	K_{II}^n
1/10	0.958	1.028
1/20	0.980	1.022
1/40	0.987	1.018
1/80	0.990	1.016

Hard Inclusion in a Finite Plate

The inclusion enrichment shown in Figure A-4 is calibrated based on results from the commercial finite element code Abaqus[®]. The material properties used in the analysis were chosen to be Young's modulus of 50 GPa and Poisson's ratio of 0.3 for the plate and Young's modulus of 70 GPa and Poisson's ratio of 0.3 for the inclusion. The full domain was a plate with height 10 m and width 6 m with a center inclusion of

radius 0.5 m. Through symmetry only the top right hand quarter of the plate was modeled. The applied stress was 1 Pa. Square plane strain quadrilateral elements with a structured mesh with average element size h of 1/30 m were used for comparison against Abaqus®.

The stress contours for the Abaqus® and MXFEM solutions are presented in Figure A-5 ,Figure A-6 , and Figure A-7. All contours have color bars with matching ranges. Abaqus® plots from black to grey, while MATLAB® plots from black to white, which results is some slight differences between figures. Note that there is also a difference in how the interface is represented as Abaqus® plots a black line, while the MXFEM code denotes all inclusions with a white line. Some of the differences in contour shape may be attributed to a different number of contours being plotted in the two programs.

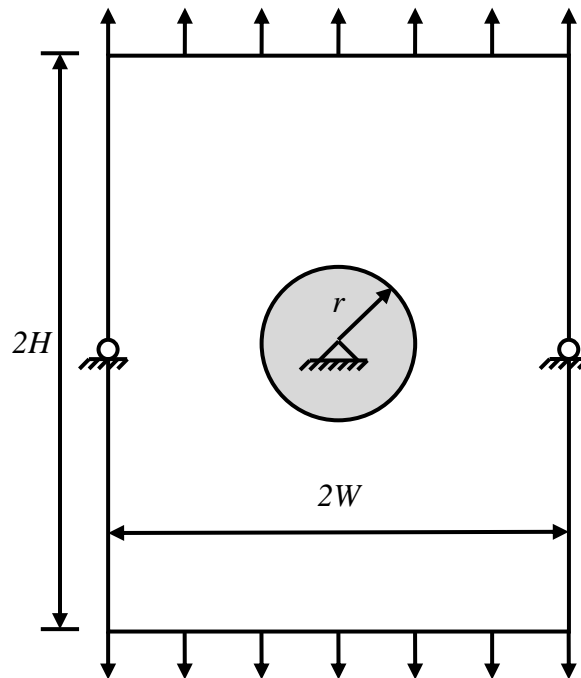


Figure A-4. Representative geometry for a hard inclusion in a finite plate.

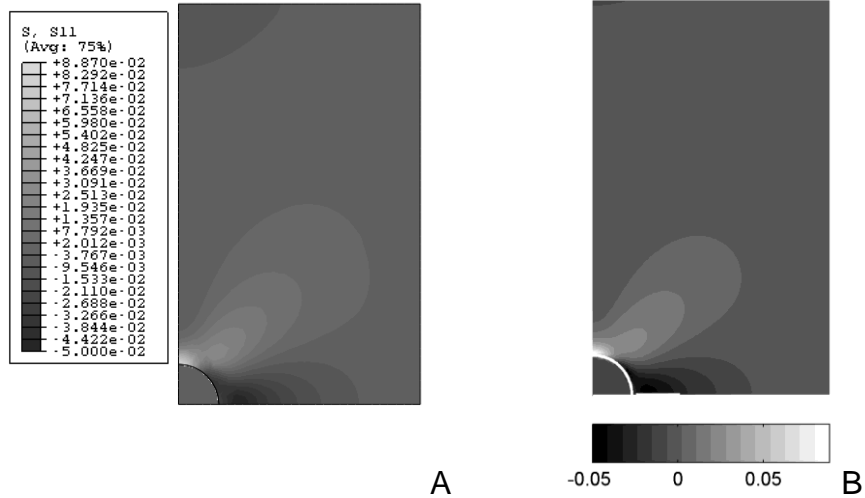


Figure A-5. The σ_{xx} contours for a hard inclusion. A) Abaqus®, B) MXFEM.

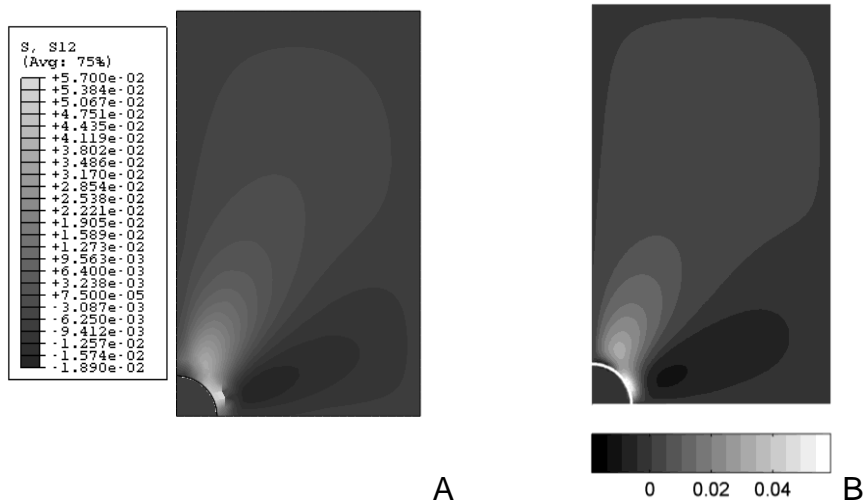


Figure A-6. The σ_{xy} contours for a hard inclusion. A) Abaqus®, B) MXFEM.

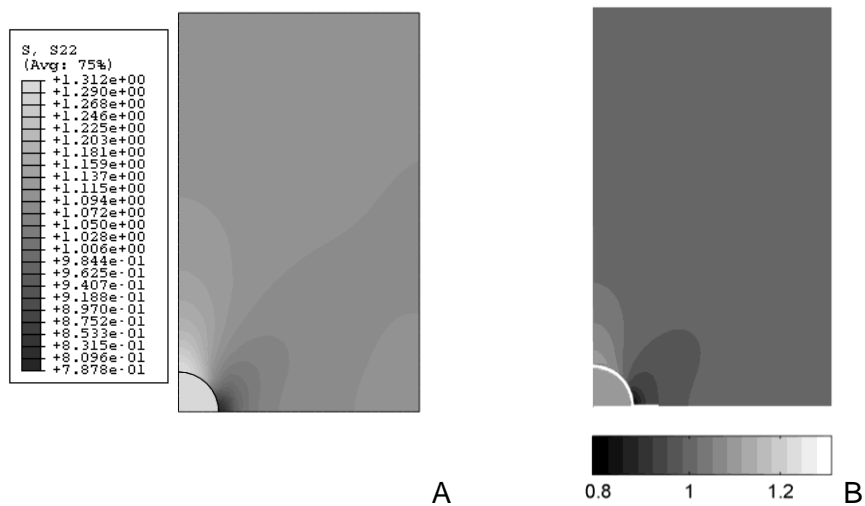


Figure A-7. The σ_{yy} contours for a hard inclusion. A) Abaqus®, B) MXFEM.

Void in an Infinite Plate

The void enrichment function is verified against the Abaqus[®] solution for the traditional FEM solution of a plate containing a hole. The material properties used in the analysis were chosen to be Young's modulus of 10 MPa and Poisson's ratio of 0.3. The full domain was a plate with height 3 m and width 3 m with a center hole of radius 0.3 m. The applied stress was 1 Pa. Square plane strain quadrilateral elements with a structured mesh with average element size h of 1/20 m was used.

The stress contours based on the Abaqus[®] solution are compared to the XFEM stress contours in Figure A-9, Figure A-10, and Figure A-11. All stress components show excellent agreement with the Abaqus[®] values. Any differences can be attributed to either having a structured mesh for the XFEM solution compared to a conforming mesh for the Abaqus[®] solution or the color scale in Abaqus[®] going from black to grey, while it goes from black to white within MATLAB[®].

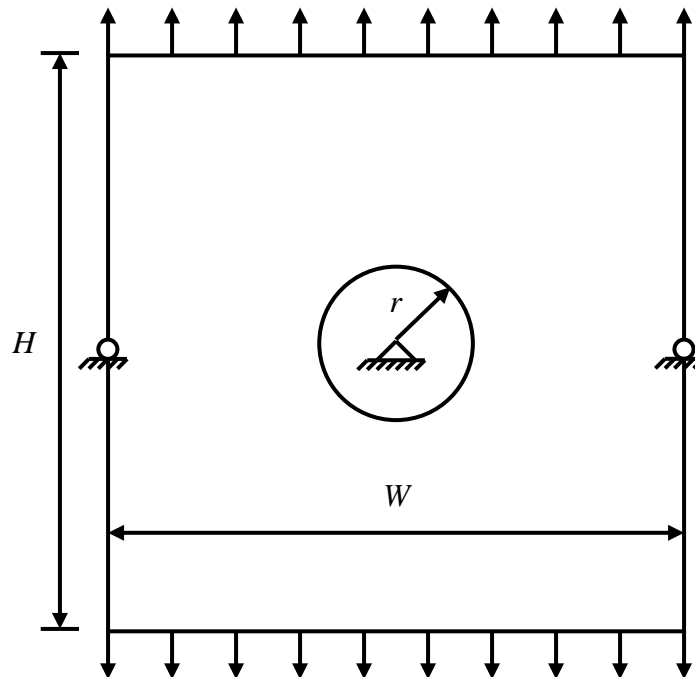


Figure A-8. Representative geometry for a void in an infinite plate.

Other Benchmarks

Angle of Crack Initiation from Optimization

An optimization algorithm is introduced using *fminbnd* in MATLAB[®] to determine the angle of crack initiation which results in the maximum energy release rate. The example of a 8 m x 8 m plate with a hole with 1 m radius subjected to uniaxial tension as shown in Figure A-12 is used to show that the optimization implementation has been completed with accuracy. Square plane strain quadrilateral elements with a structured mesh with an average element size of h equal to 1/20 m was used. For this problem the location of maximum stress corresponds to the angle of crack initiation for a 0.15 m crack which will result in the maximum energy release rate. For a plate under uniaxial tension this angle is 0 or π radians.

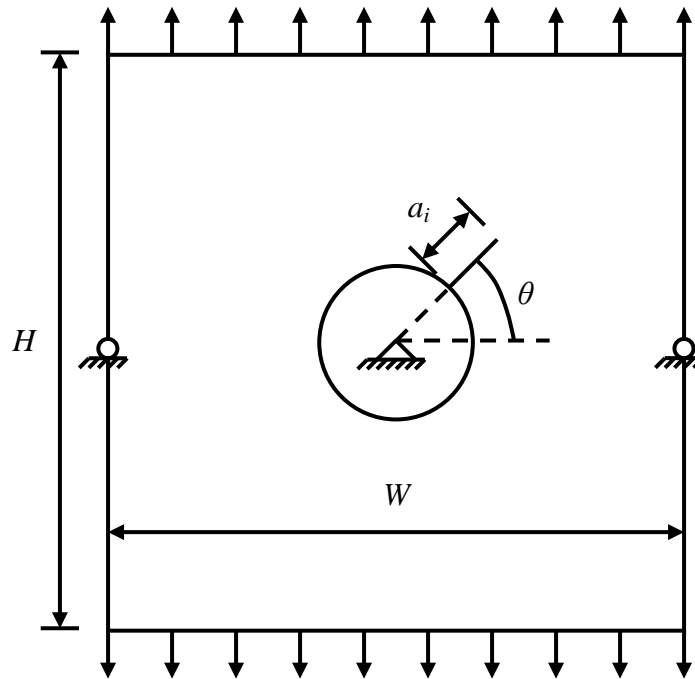


Figure A-12. Representative geometry for a crack initiating at an angle θ for a plate with a hole.

The optimization problem used to benchmark the implementation of the XFEM optimization subroutine is given as

$$\begin{aligned} \min \quad & -G(\theta) = \frac{K_I^2}{E_{eff}} + \frac{K_{II}^2}{E_{eff}} \\ \text{s.t.} \quad & \theta_L \leq \theta \leq \theta_U \end{aligned} \quad \text{A-4}$$

where G is the energy release rate, K_I and K_{II} are the Mode I and II stress intensity factors, θ_L and θ_U are the lower and upper bounds on the angle and E_{eff} is given as

$$E_{eff} = \begin{cases} E & \text{plane stress} \\ \frac{E}{1-\nu^2} & \text{plane strain} \end{cases} \quad \text{A-5}$$

The results are presented in Table A-4 for two sets of bounds $-\pi/2 \leq \theta \leq \pi/2$ and $\pi/2 \leq \theta \leq 3\pi/2$. Results are presented as the optimum angle identified θ_{opt} by *fminbnd* with the function tolerance set to 1E-9 and the angle tolerance set to 1E-6. The normalized energy release rate is

$$G^n = \frac{G^{XFEM}}{G^t} \quad \text{A-6}$$

where G^t is the energy release rate corresponding to an initiation angle of 0 or π radians and G^{XFEM} is the energy release rate from the optimization with the XFEM. For this example the theoretical maximum energy release rate is given as $G^t = 3.5166\text{E-}7$ J/m². Based upon the function and angle tolerances, the solutions represent an excellent agreement between the known solution and the MXFEM optimization result.

Table A-4. Comparison of the theoretical and MXFEM value for maximum energy release angle as a function of average element size.

h	$-\pi/2 \leq \theta \leq \pi/2$		$\pi/2 \leq \theta \leq 3\pi/2$	
	θ_{opt}	G^n	θ_{opt}	G^n
1/20	-1.715E-5	1.001	3.142	1.000

Crack Growth in Presence of an Inclusion

Bordas [69] presented the case of edge crack growth under mixed-mode loading in a plate with either a hard or soft inclusion. This problem acts to verify the implementation of mixed-mode crack problems, the inclusion enrichment function, and the use of both the crack and inclusion enrichment functions in a single framework. The material properties used in the analysis were chosen to be Young's modulus of 1 GPa and Poisson's ratio of 0.3 for material 1 and Young's modulus of 10 GPa and Poisson's ratio of 0.3 for material 2. For the case of a hard inclusion, material 2 is for the inclusion and material 1 is for the plate. For the case of a soft inclusion, material 1 is for the inclusion and material 2 is for the plate. The full domain was a plate with height 8 m and width 4 m with an edge crack of length 0.5 m centered on the left edge. The circular inclusion of radius 1 is placed at the horizontal midpoint and the vertical quarter point.

There were 34 iterations of growth where at each iteration the amount of growth was equal to $\Delta a = 0.1$ m and in the direction given by the maximum circumferential stress predicted by a unit tensile load which was applied to the top edge of the domain in the y -direction. Square plain strain quadrilateral elements with a structured mesh with average element size h of 1/20 m were used. It is important to note that no boundary conditions were given by Bordas so here it is assumed that edge crack boundary conditions are to be used. This may explain the slight differences between the results of Bordas and those presented in Figure A-13. Note that the scales of the x and y axis are different, which result in the circular soft inclusion appearing to take a shape more similar to that of an ellipse. Also, what appears to be a large initial crack growth increment corresponds to the two data points corresponding to the initial crack geometry.

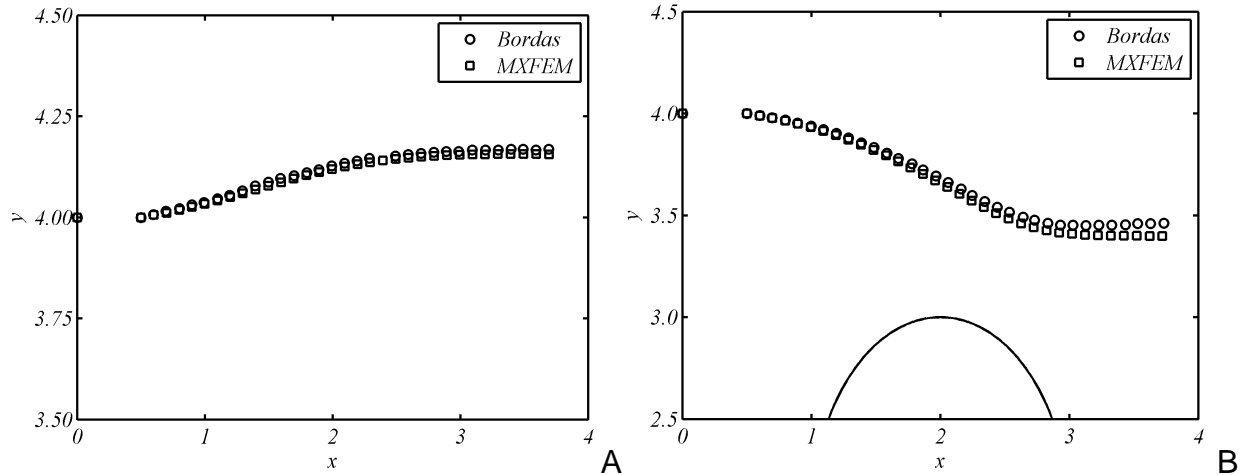


Figure A-13. Comparison of crack paths to those predicted by Bordas for a hard and soft inclusion. A) Hard inclusion, B) Soft inclusion.

Fatigue Crack Growth

The implementation of the Paris model [34] for fatigue crack growth was verified within the XFEM framework. The Paris model predicts that crack growth occurs according to the differential equation

$$\frac{da}{dN} = C(\Delta K)^m \quad \text{A-7}$$

where da/dN is the crack growth rate, C is the Paris model constant, m is the Paris model exponent, and ΔK is the stress intensity factor range under cyclic loading. Here the geometry is chosen to mimic a center crack in an infinite plate where ΔK is

$$\Delta K = \Delta\sigma\sqrt{\pi a} \quad \text{A-8}$$

where $\Delta\sigma$ is the applied stress range and a is the half crack length.

The material properties used in the analysis were chosen to be Young's modulus of 71.7 GPa, Poisson's ratio of 0.33, Paris model constant of 1.5E-10, and Paris model exponent of 3.8. The full domain was a plate with height 0.4 m and width 0.6 m with a center crack of length 0.02 m. The applied stress was 78.6 MPa. Square plane strain quadrilateral elements with a structured mesh with average element size h of 1/500 m

was used. Through symmetry, only the right half of the geometry was modeled. Fatigue crack growth was measured to 2450 cycles with step sizes of ΔN equal to 50 at each simulation. A comparison of the theoretical and simulated crack growth is given in Figure A-14. From this analysis it is apparent that the XFEM and Paris model solutions are in good agreement. As the crack size increases, there begins to be a difference between the two solutions. It is likely that the choice of a smaller number of elapsed cycles at each iteration would reduce the differences between the two predictions for large crack sizes.

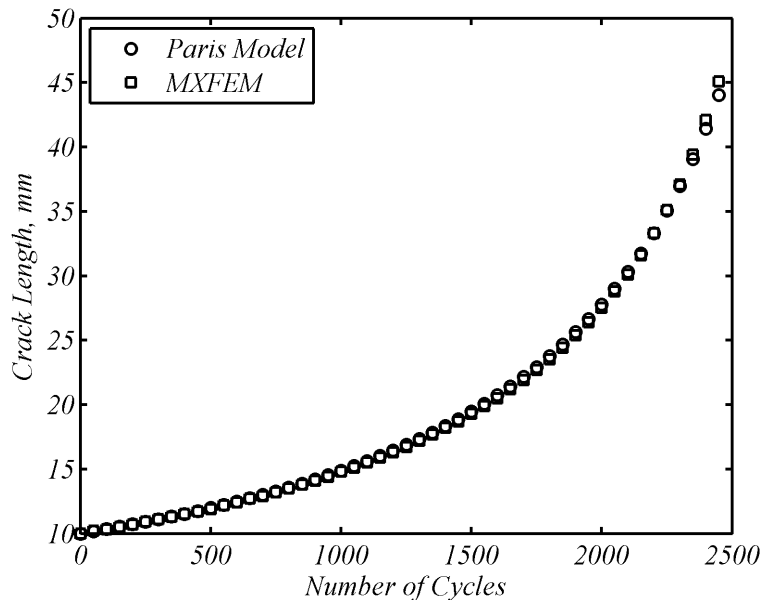


Figure A-14. Comparison between Paris model and XFEM simulation for fatigue crack growth for a center crack in an infinite plate.

APPENDIX B
AUXILIARY DISPLACEMENT AND STRESS STATES

The auxiliary displacement and stress states given by Westergaard [145] and Williams [146] for that are used in the interaction integrals [16, 18, 19] to calculate the stress intensity factors are given in terms of polar coordinates from crack tip r and θ , shear modulus μ , Poisson's ratio ν , and Kosolov constant κ as

$$u_1 = \frac{1}{2\mu} \sqrt{\frac{r}{2\pi}} \left[K_I \cos \frac{\theta}{2} (\kappa - \cos \theta) + K_{II} \sin \frac{\theta}{2} (\kappa + 2 + \cos \theta) \right] \quad 10-1$$

$$u_2 = \frac{1}{2\mu} \sqrt{\frac{r}{2\pi}} \left[K_I \sin \frac{\theta}{2} (\kappa - \sin \theta) + K_{II} \cos \frac{\theta}{2} (\kappa - 2 + \cos \theta) \right] \quad 10-2$$

$$u_3 = \frac{2}{\mu} \sqrt{\frac{r}{2\pi}} K_{III} \sin \frac{\theta}{2} \quad 10-3$$

$$\sigma_{11} = \frac{1}{\sqrt{2\pi r}} \left[K_I \cos \frac{\theta}{2} \left(1 - \sin \frac{\theta}{2} \sin \frac{3\theta}{2} \right) - K_{II} \sin \frac{\theta}{2} \left(2 + \cos \frac{\theta}{2} \cos \frac{3\theta}{2} \right) \right] \quad 10-4$$

$$\sigma_{22} = \frac{1}{\sqrt{2\pi r}} \left[K_I \cos \frac{\theta}{2} \left(1 + \sin \frac{\theta}{2} \sin \frac{3\theta}{2} \right) + K_{II} \sin \frac{\theta}{2} \cos \frac{\theta}{2} \cos \frac{3\theta}{2} \right] \quad 10-5$$

$$\sigma_{33} = \nu (\sigma_{11} + \sigma_{22}) \quad 10-6$$

$$\sigma_{23} = \frac{1}{\sqrt{2\pi r}} K_{III} \cos \frac{\theta}{2} \quad 10-7$$

$$\sigma_{31} = \frac{-1}{\sqrt{2\pi r}} \sin \frac{\theta}{2} \quad 10-8$$

$$\sigma_{12} = \frac{1}{\sqrt{2\pi r}} \left[K_I \sin \frac{\theta}{2} \cos \frac{\theta}{2} \cos \frac{3\theta}{2} + K_{II} \cos \frac{\theta}{2} \left(1 - \sin \frac{\theta}{2} \sin \frac{3\theta}{2} \right) \right] \quad 10-9$$

$$\kappa = \begin{cases} \frac{3-\nu}{1+\nu} & \text{plane stress} \\ 3-4\nu & \text{plane strain} \end{cases} \quad 10-10$$

APPENDIX C
CONVERSION OF NORMALIZED FLIGHT DATA TO SCALED FLIGHT DATA

Table C-1. Normalized and scaled flight data with conversion for Flight ID 2.

Variable	Norm Min	Norm Max	Scaled Min	Scaled Max	Conversion
g	0.0186	0.908	0.75	1.5	$g = 0.843g_{norm} + 0.734$
θ_B	-0.711	0.574	0	30	$\theta_B = 23.2a_{roll} + 16.5$
m_{fuel}	0.00	0.971	800	50,000	$m_{fuel} = 51500f_{norm}$
M	0.0191	0.921	0	0.80	$M = 0.887M_{norm} - 0.0170$
v	0.0222	0.822	0	236	$v = 295v_{norm} - 6.56$
α	0.0178	0.853	0.001	10	$\alpha = 12.0\alpha_{norm} - 0.212$

Table C-2. Normalized and scaled flight data with conversion for Flight ID 8.

Variable	Norm Min	Norm Max	Scaled Min	Scaled Max	Conversion
g	-0.0609	0.914	0.75	1.5	$g = 0.769g_{norm} + 0.797$
θ_B	-0.485	0.490	0	30	$\theta_B = 30.8a_{roll} + 14.9$
m_{fuel}	0.00	0.990	800	50,000	$m_{fuel} = 50500f_{norm}$
M	0.0191	0.954	0	0.80	$M = 0.856M_{norm} - 0.0163$
v	0.0222	0.962	0	236	$v = 252v_{norm} - 5.59$
α	0.00	0.833	0.001	10	$\alpha = 12.0\alpha_{norm} + 0.001$

Table C-3. Normalized and scaled flight data with conversion for Flight ID 10.

Variable	Norm Min	Norm Max	Scaled Min	Scaled Max	Conversion
g	0.0793	0.337	0.75	1.5	$g = 2.91g_{norm} + 0.519$
θ_B	-0.196	0.195	0	30	$\theta_B = 76.7a_{roll} + 15.0$
m_{fuel}	0.00	0.986	800	50,000	$m_{fuel} = 50700f_{norm}$
M	0.191	0.579	0	0.80	$M = 1.43M_{norm} - 0.0273$
v	0.0222	0.663	0	236	$v = 369v_{norm} - 8.19$
α	0.00	0.844	0.001	10	$\alpha = 11.9\alpha_{norm} + 0.001$

Table C-4. Normalized and scaled flight data with conversion for Flight ID 12.

Variable	Norm Min	Norm Max	Scaled Min	Scaled Max	Conversion
g	0.0599	0.847	0.75	1.5	$g = 0.952g_{norm} + 0.693$
θ_B	-0.324	0.312	0	30	$\theta_B = 47.2a_{roll} + 15.3$
m_{fuel}	0.00	0.993	800	50,000	$m_{fuel} = 50400f_{norm}$
M	0.0191	0.867	0	0.80	$M = 0.944M_{norm} - 0.0180$
v	0.0222	0.828	0	236	$v = 293v_{norm} - 6.51$
α	0.00	0.723	0.001	10	$\alpha = 13.8\alpha_{norm} + 0.001$

Table C-5. Normalized and scaled flight data with conversion for Flight ID 16.

Variable	Norm Min	Norm Max	Scaled Min	Scaled Max	Conversion
g	0.0248	0.965	0.75	1.5	$g = 0.797g_{norm} + 0.730$
θ_B	-0.639	0.634	0	30	$\theta_B = 31.2a_{roll} + 19.9$
m_{fuel}	0.00	0.996	800	50,000	$m_{fuel} = 50200f_{norm}$
M	0.0191	0.987	0	0.80	$M = 0.827M_{norm} - 0.0158$
v	0.0222	0.919	0	236	$v = 264v_{norm} - 5.85$
α	0.00	0.794	0.001	10	$\alpha = 12.6\alpha_{norm} + 0.001$

Table C-6. Normalized and scaled flight data with conversion for Flight ID 18.

Variable	Norm Min	Norm Max	Scaled Min	Scaled Max	Conversion
g	-0.145	0.880	0.75	1.5	$g = 0.732g_{norm} + 0.856$
θ_B	-0.817	0.759	0	30	$\theta_B = 19.0a_{roll} + 15.5$
m_{fuel}	0.00	0.941	800	50,000	$m_{fuel} = 53100f_{norm}$
M	0.0191	0.941	0	0.80	$M = 0.868M_{norm} - 0.0166$
v	0.0222	0.825	0	236	$v = 295v_{norm} - 6.54$
α	0.00	0.721	0.001	10	$\alpha = 13.9\alpha_{norm} + 0.001$

Table C-7. Normalized and scaled flight data with conversion for Flight ID 22.

Variable	Norm Min	Norm Max	Scaled Min	Scaled Max	Conversion
g	0.0838	0.848	0.75	1.5	$g = 0.981g_{norm} + 0.668$
θ_B	-0.488	0.505	0	30	$\theta_B = 30.2a_{roll} + 14.7$
m_{fuel}	0.00	0.998	800	50,000	$m_{fuel} = 50100f_{norm}$
M	0.0191	0.947	0	0.80	$M = 0.862M_{norm} - 0.0165$
v	0.0222	0.821	0	236	$v = 296v_{norm} - 6.57$
α	0.00	0.819	0.001	10	$\alpha = 12.2\alpha_{norm} + 0.001$

Table C-8. Normalized and scaled flight data with conversion for Flight ID 26.

Variable	Norm Min	Norm Max	Scaled Min	Scaled Max	Conversion
g	6.88E-4	0.586	0.75	1.5	$g = 1.28g_{norm} + 0.749$
θ_B	-0.463	0.291	0	30	$\theta_B = 39.8a_{roll} + 18.4$
m_{fuel}	0.00	0.992	800	50,000	$m_{fuel} = 50400f_{norm}$
M	0.0191	0.617	0	0.80	$M = 1.34M_{norm} - 0.0256$
v	0.0222	0.709	0	236	$v = 344v_{norm} - 7.65$
α	0.0178	0.858	0.001	10	$\alpha = 11.9\alpha_{norm} + 0.001$

Table C-9. Normalized and scaled flight data with conversion for Flight ID 138.

Variable	Norm Min	Norm Max	Scaled Min	Scaled Max	Conversion
g	-0.0269	0.882	0.75	1.5	$g = 0.825g_{norm} + 0.772$
θ_B	-0.569	0.651	0	30	$\theta_B = 24.6a_{roll} + 14.0$
m_{fuel}	0.00	0.913	800	50,000	$m_{fuel} = 54700f_{norm}$
M	0.0191	0.961	0	0.80	$M = 0.849M_{norm} - 0.0162$
v	0.0222	0.836	0	236	$v = 290v_{norm} - 6.45$
α	0.00890	0.869	0.001	10	$\alpha = 11.6\alpha_{norm} + 0.001$

Table C-10. Normalized and scaled flight data with conversion for Flight ID 140.

Variable	Norm Min	Norm Max	Scaled Min	Scaled Max	Conversion
g	0.00730	1.00	0.75	1.5	$g = 0.756g_{norm} + 0.744$
θ_B	-0.607	0.756	0	30	$\theta_B = 22.0a_{roll} + 13.4$
m_{fuel}	0.00	0.934	800	50,000	$m_{fuel} = 53500f_{norm}$
M	0.0191	0.951	0	0.80	$M = 0.886M_{norm} - 0.0163$
v	0.0222	0.838	0	236	$v = 290v_{norm} - 6.43$
α	0.0124	0.799	0.001	10	$\alpha = 12.7\alpha_{norm} - 0.157$

Table C-11. Normalized and scaled flight data with conversion for Flight ID 146.

Variable	Norm Min	Norm Max	Scaled Min	Scaled Max	Conversion
g	-0.0775	0.913	0.75	1.5	$g = 0.757g_{norm} + 0.809$
θ_B	-0.709	0.727	0	30	$\theta_B = 20.9a_{roll} + 14.8$
m_{fuel}	0.00	0.914	800	50,000	$m_{fuel} = 54700f_{norm}$
M	0.0190	0.991	0	0.80	$M = 0.823M_{norm} - 0.0156$
v	0.0222	1.00	0	236	$v = 242v_{norm} - 5.37$
α	0.00	0.879	0.001	10	$\alpha = 11.3\alpha_{norm} + 0.001$

Table C-12. Normalized and scaled flight data with conversion for Flight ID 148.

Variable	Norm Min	Norm Max	Scaled Min	Scaled Max	Conversion
g	-0.0136	0.954	0.75	1.5	$g = 0.775g_{norm} + 0.761$
θ_B	-0.775	0.611	0	30	$\theta_B = 21.6a_{roll} + 16.8$
m_{fuel}	0.00	0.961	800	50,000	$m_{fuel} = 52000f_{norm}$
M	0.019	1.00	0	0.80	$M = 0.815M_{norm} - 0.0155$
v	0.0222	0.983	0	236	$v = 246v_{norm} - 5.46$
α	0.00	0.908	0.001	10	$\alpha = 11.0\alpha_{norm} + 0.001$

Table C-13. Normalized and scaled flight data with conversion for Flight ID 150.

Variable	Norm Min	Norm Max	Scaled Min	Scaled Max	Conversion
g	-0.169	0.919	0.75	1.5	$g = 0.689g_{norm} + 0.866$
θ_B	-0.920	0.745	0	30	$\theta_B = 18.0a_{roll} + 16.6$
m_{fuel}	0.00	0.956	800	50,000	$m_{fuel} = 52300f_{norm}$
M	0.0190	0.954	0	0.80	$M = 0.856M_{norm} - 0.0163$
v	0.0222	0.837	0	236	$v = 290v_{norm} - 6.44$
α	0.00	1.00	0.001	10	$\alpha = 10.0\alpha_{norm} + 0.001$

Table C-14. Normalized and scaled flight data with conversion for Flight ID 152.

Variable	Norm Min	Norm Max	Scaled Min	Scaled Max	Conversion
g	-0.208	0.957	0.75	1.5	$g = 0.644g_{norm} + 0.884$
θ_B	-1.00	0.624	0	30	$\theta_B = 18.5a_{roll} + 18.5$
m_{fuel}	0.00	0.975	800	50,000	$m_{fuel} = 51300f_{norm}$
M	0.0191	0.977	0	0.80	$M = 0.835M_{norm} - 0.0159$
v	0.0222	0.839	0	236	$v = 289v_{norm} - 6.42$
α	0.00	0.853	0.001	10	$\alpha = 11.7\alpha_{norm} + 0.001$

Table C-15. Normalized and scaled flight data with conversion for Flight ID 154.

Variable	Norm Min	Norm Max	Scaled Min	Scaled Max	Conversion
g	-0.011	0.922	0.75	1.5	$g = 0.804g_{norm} + 0.759$
θ_B	-0.696	0.513	0	30	$\theta_B = 24.8a_{roll} + 17.3$
m_{fuel}	0.00	0.993	800	50,000	$m_{fuel} = 50400f_{norm}$
M	0.0191	0.979	0	0.80	$M = 0.834M_{norm} - 0.0159$
v	0.0222	0.978	0	236	$v = 247v_{norm} - 5.49$
α	0.00	0.931	0.001	10	$\alpha = 10.7\alpha_{norm} + 0.001$

Table C-16. Normalized and scaled flight data with conversion for Flight ID 156.

Variable	Norm Min	Norm Max	Scaled Min	Scaled Max	Conversion
g	-4.20E-4	0.900	0.75	1.5	$g = 0.833g_{norm} + 0.750$
θ_B	-0.652	0.697	0	30	$\theta_B = 22.2a_{roll} + 14.5$
m_{fuel}	0.00	0.927	800	50,000	$m_{fuel} = 53900f_{norm}$
M	0.0219	0.928	0	0.80	$M = 0.883M_{norm} - 0.0193$
v	0.0256	0.821	0	236	$v = 297v_{norm} - 7.61$
α	0.0373	0.831	0.001	10	$\alpha = 12.6\alpha_{norm} - 0.469$

Table C-17. Normalized and scaled flight data with conversion for Flight ID 159.

Variable	Norm Min	Norm Max	Scaled Min	Scaled Max	Conversion
g	-0.0765	0.917	0.75	1.5	$g = 0.755g_{norm} + 0.808$
θ_B	-0.530	0.492	0	30	$\theta_B = 29.3a_{roll} + 15.6$
m_{fuel}	0.00	0.946	800	50,000	$m_{fuel} = 52800f_{norm}$
M	0.0192	0.993	0	0.80	$M = 0.821M_{norm} - 0.0158$
v	0.0225	0.985	0	236	$v = 246v_{norm} - 5.53$
α	0.00	0.734	0.001	10	$\alpha = 13.6\alpha_{norm} + 0.001$

Table C-18. Normalized and scaled flight data with conversion for Flight ID 161.

Variable	Norm Min	Norm Max	Scaled Min	Scaled Max	Conversion
g	0.0182	0.878	0.75	1.5	$g = 0.872g_{norm} + 0.734$
θ_B	-0.492	0.471	0	30	$\theta_B = 31.2a_{roll} + 15.3$
m_{fuel}	0.00	0.936	800	50,000	$m_{fuel} = 53400f_{norm}$
M	0.0201	0.9808	0	0.80	$M = 0.832M_{norm} - 0.0167$
v	0.0236	0.966	0	236	$v = 251v_{norm} - 5.92$
α	0.00	0.826	0.001	10	$\alpha = 12.1\alpha_{norm} + 0.001$

Table C-19. Normalized and scaled flight data with conversion for Flight ID 163.

Variable	Norm Min	Norm Max	Scaled Min	Scaled Max	Conversion
g	0.00360	0.900	0.75	1.5	$g = 0.837g_{norm} + 0.747$
θ_B	-0.518	0.725	0	30	$\theta_B = 24.1a_{roll} + 12.5$
m_{fuel}	0.00	0.946	800	50,000	$m_{fuel} = 52900f_{norm}$
M	0.0209	0.946	0	0.80	$M = 0.865M_{norm} - 0.0181$
v	0.0244	0.843	0	236	$v = 289v_{norm} - 7.05$
α	0.00890	0.879	0.001	10	$\alpha = 11.5\alpha_{norm} - 0.101$

APPENDIX D
STRESS HISTORIES FOR FLIGHT DATA FROM AFRL

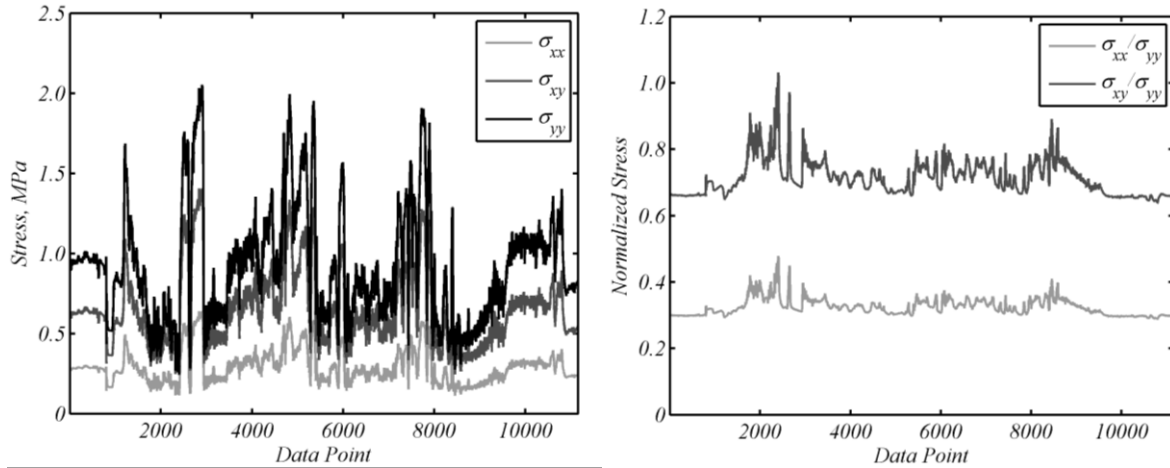


Figure D-1. Stress history for Flight ID 2. A) Bi-axial stress, B) Normalized stress.

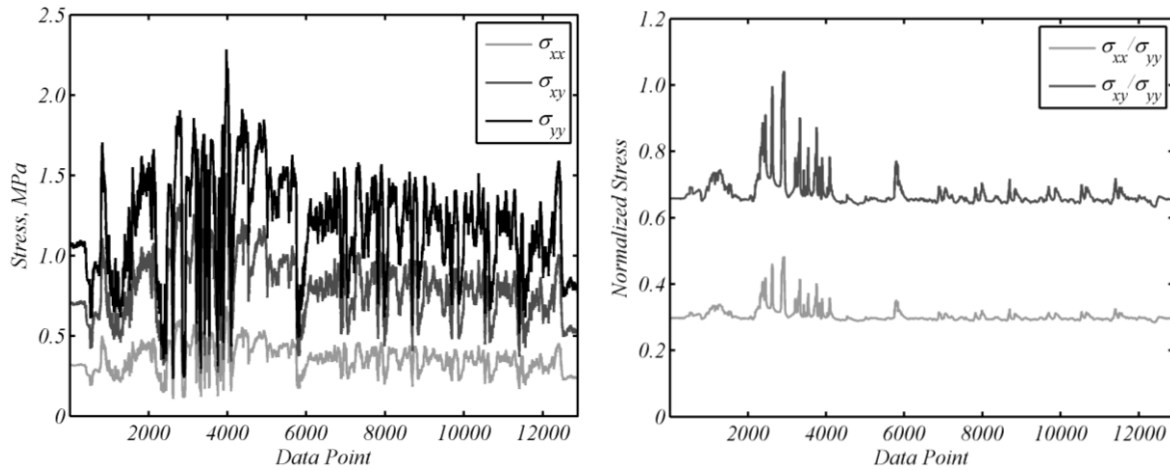


Figure D-2. Stress history for Flight ID 8. A) Bi-axial stress, B) Normalized stress.

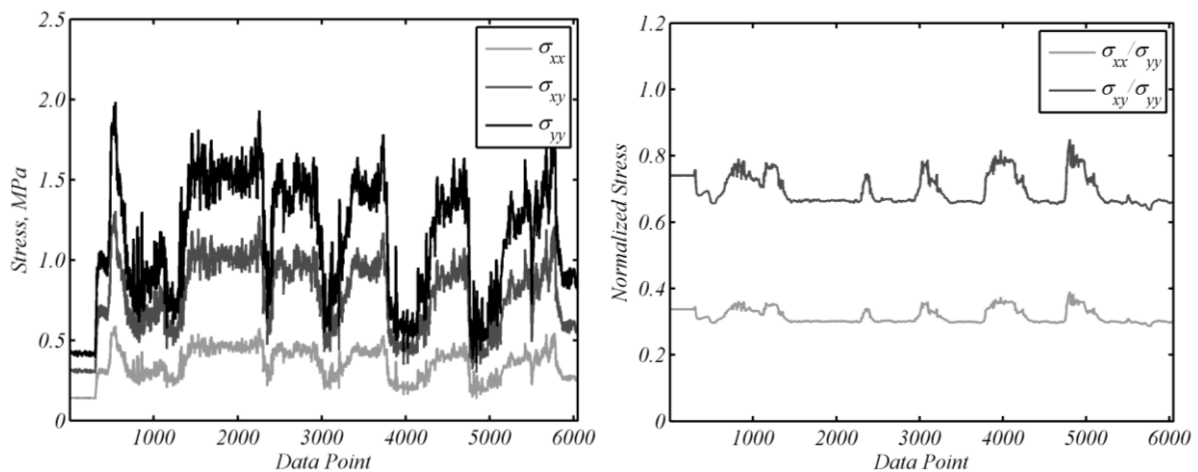


Figure D-3. Stress history for Flight ID 10. A) Bi-axial stress, B) Normalized stress.

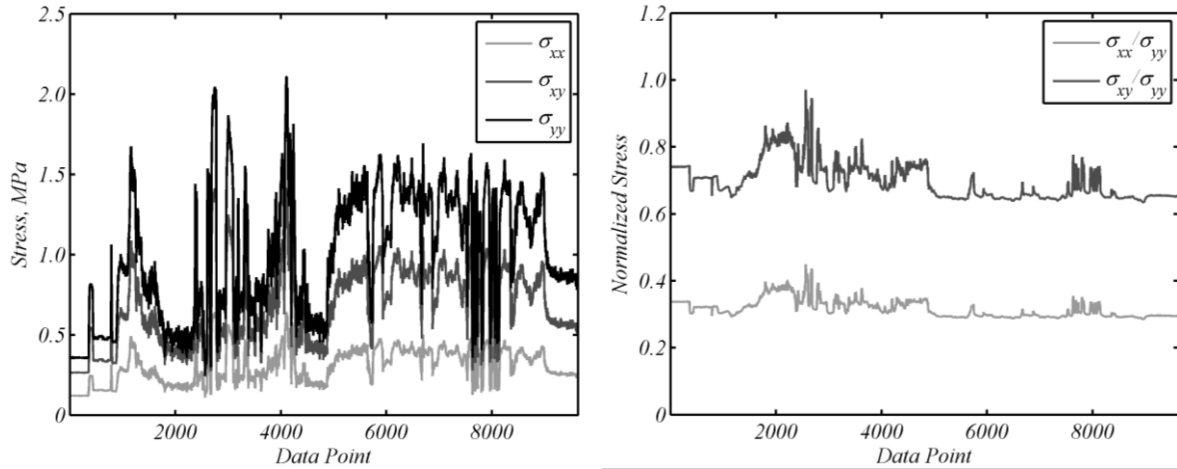


Figure D-4. Stress history for Flight ID 12. A) Bi-axial stress, B) Normalized stress.

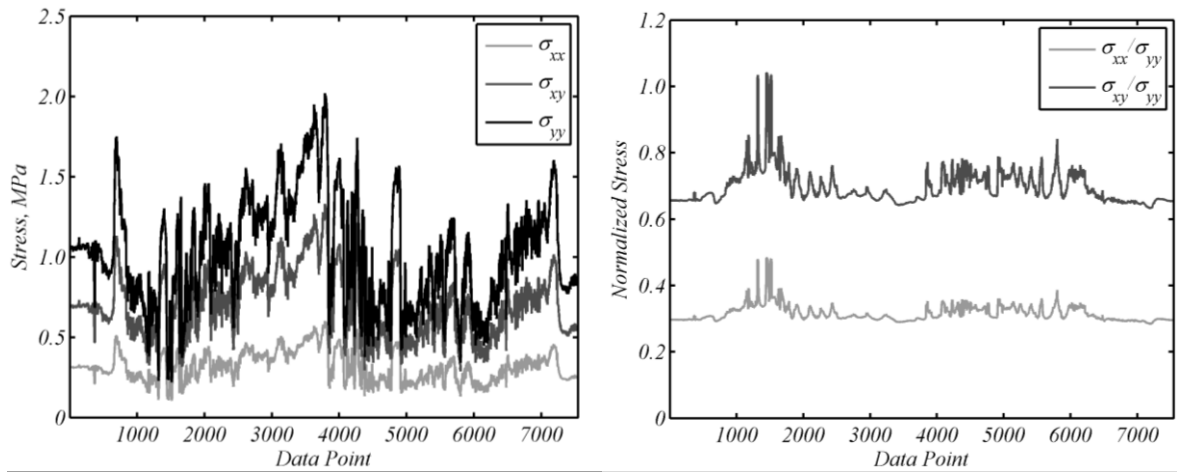


Figure D-5. Stress history for Flight ID 16. A) Bi-axial stress, B) Normalized stress.

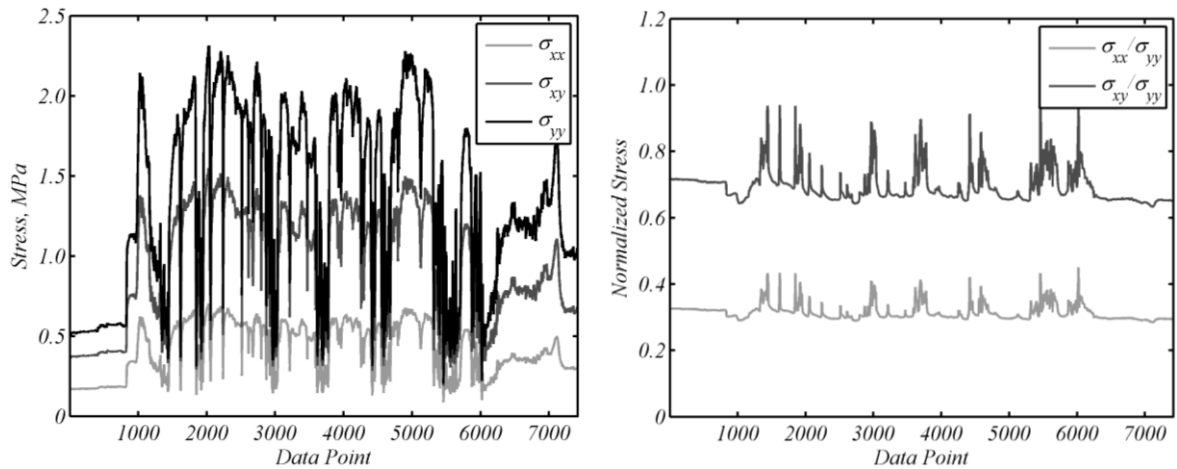


Figure D-6. Stress history for Flight ID 18. A) Bi-axial stress, B) Normalized stress.

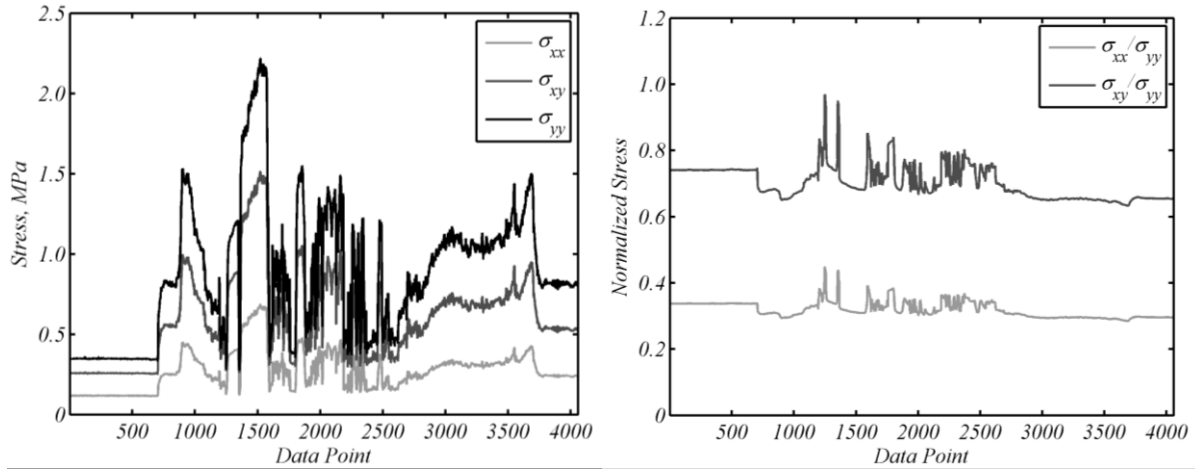


Figure D-7. Stress history for Flight ID 22. A) Bi-axial stress, B) Normalized stress.

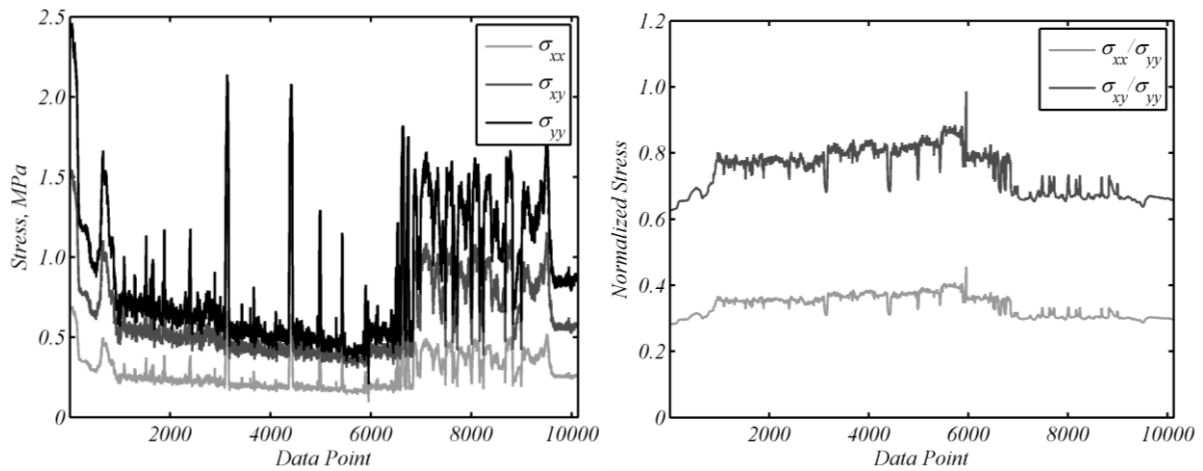


Figure D-8. Stress history for Flight ID 26. A) Bi-axial stress, B) Normalized stress.

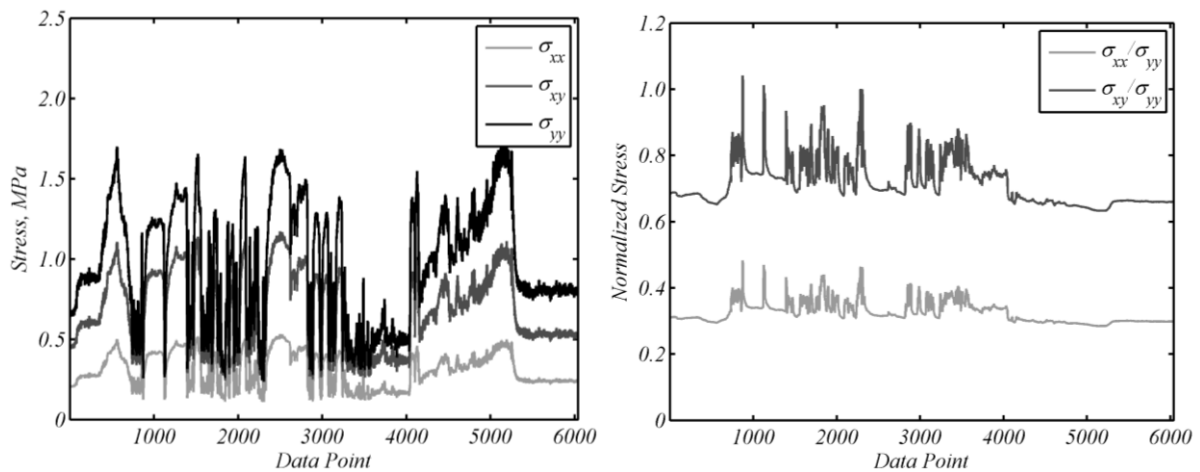


Figure D-9. Stress history for Flight ID 138. A) Bi-axial stress, B) Normalized stress.

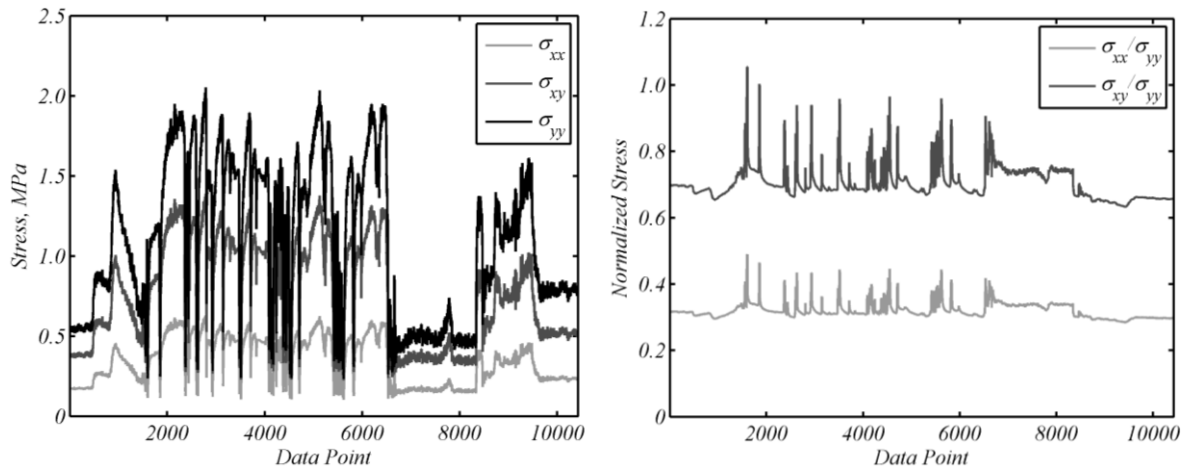


Figure D-10. Stress history for Flight ID 140. A) Bi-axial stress, B) Normalized stress.

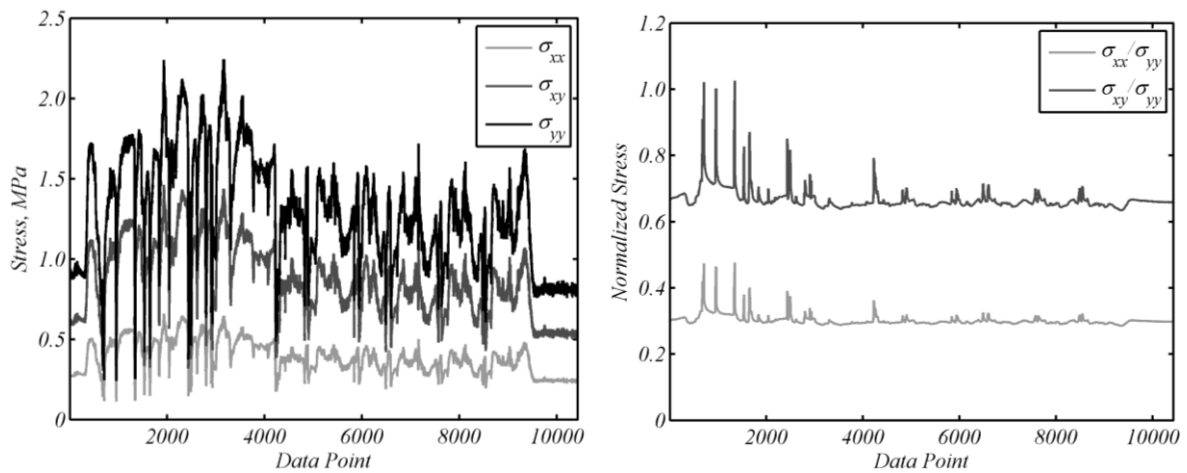


Figure D-11. Stress history for Flight ID 146. A) Bi-axial stress, B) Normalized stress.

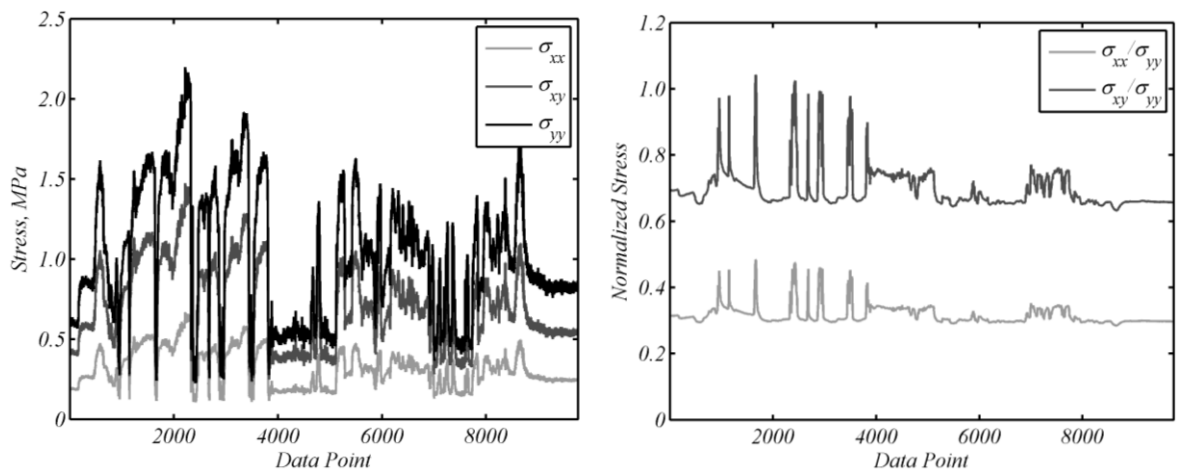


Figure D-12. Stress history for Flight ID 148. A) Bi-axial stress, B) Normalized stress.

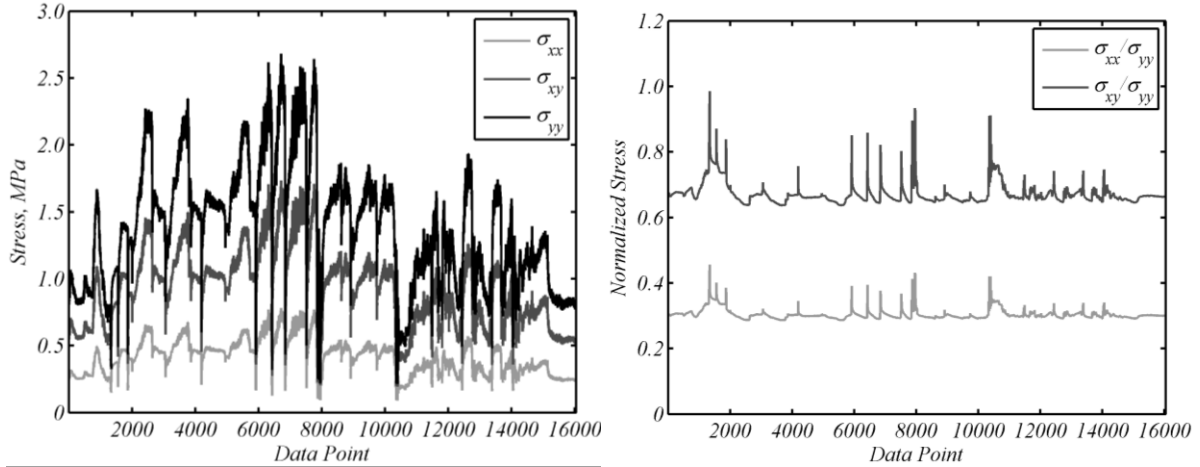


Figure D-13. Stress history for Flight ID 150. A) Bi-axial stress, B) Normalized stress.

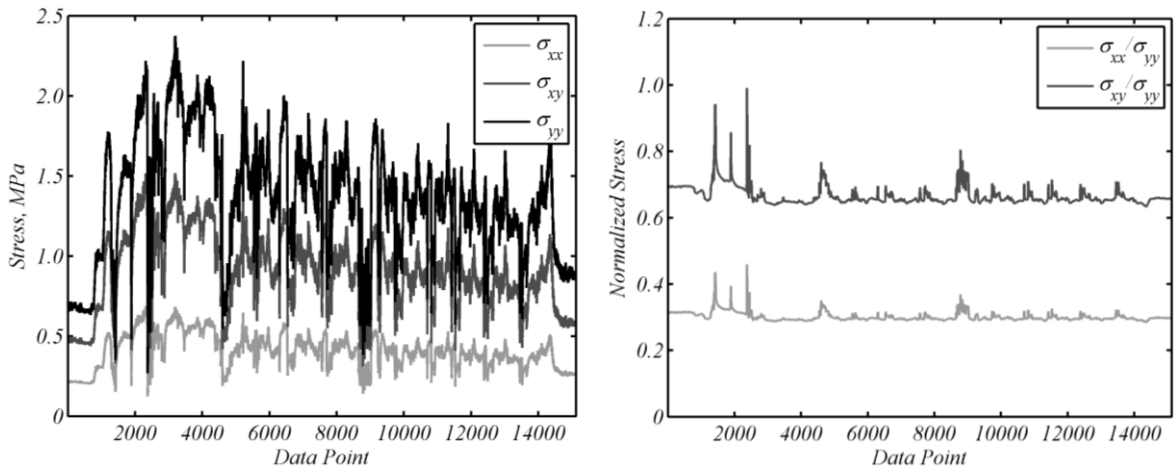


Figure D-14. Stress history for Flight ID 152. A) Bi-axial stress, B) Normalized stress.

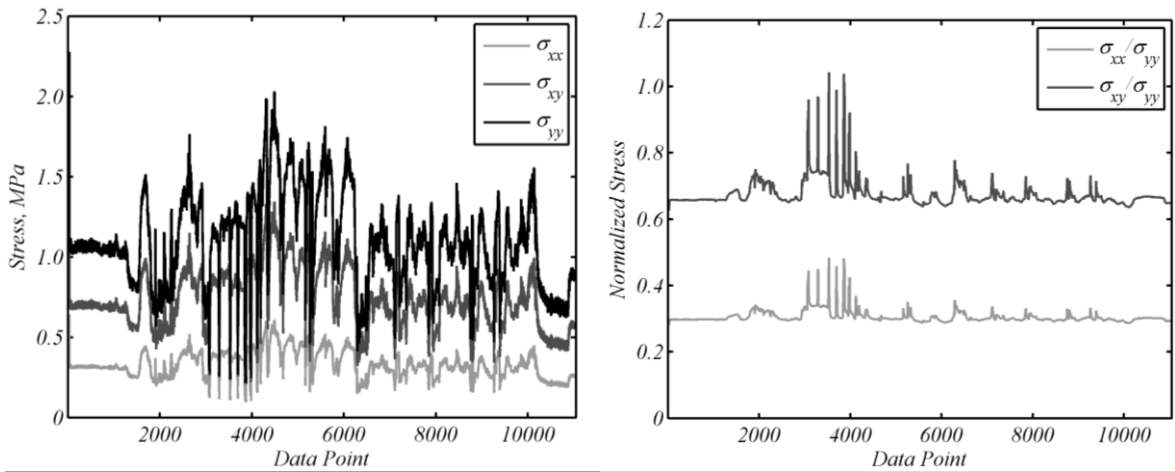


Figure D-15. Stress history for Flight ID 154. A) Bi-axial stress, B) Normalized stress.

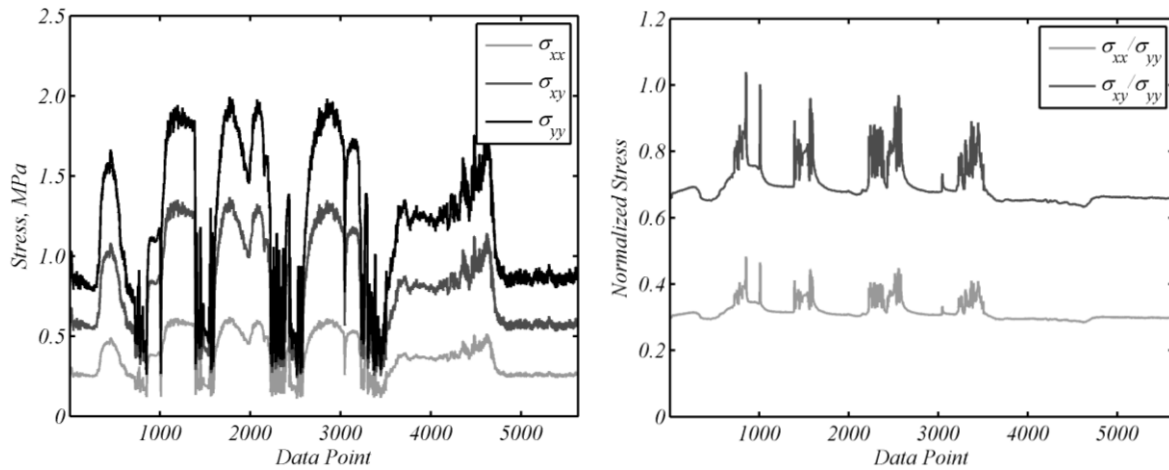


Figure D-16. Stress history for Flight ID 156. A) Bi-axial stress, B) Normalized stress.

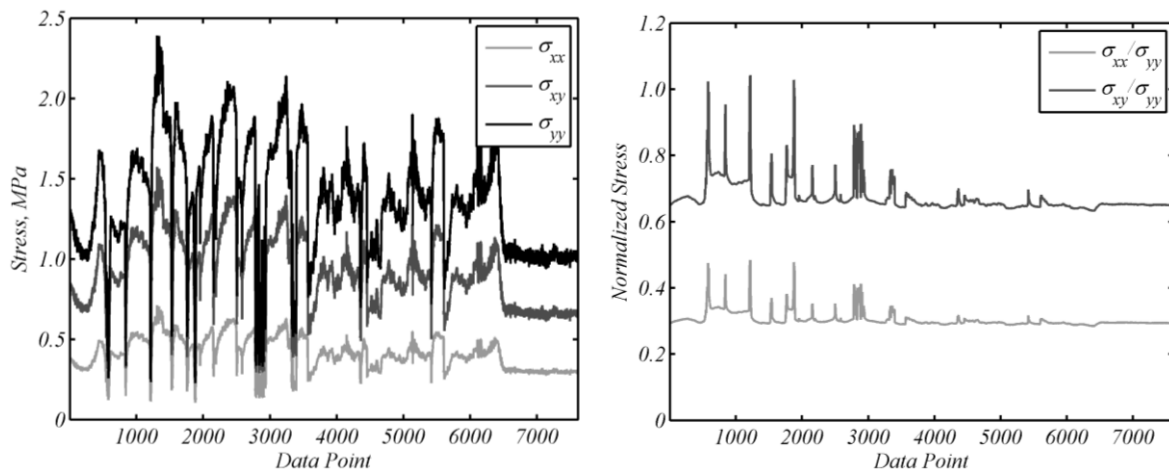


Figure D-17. Stress history for Flight ID 159. A) Bi-axial stress, B) Normalized stress.

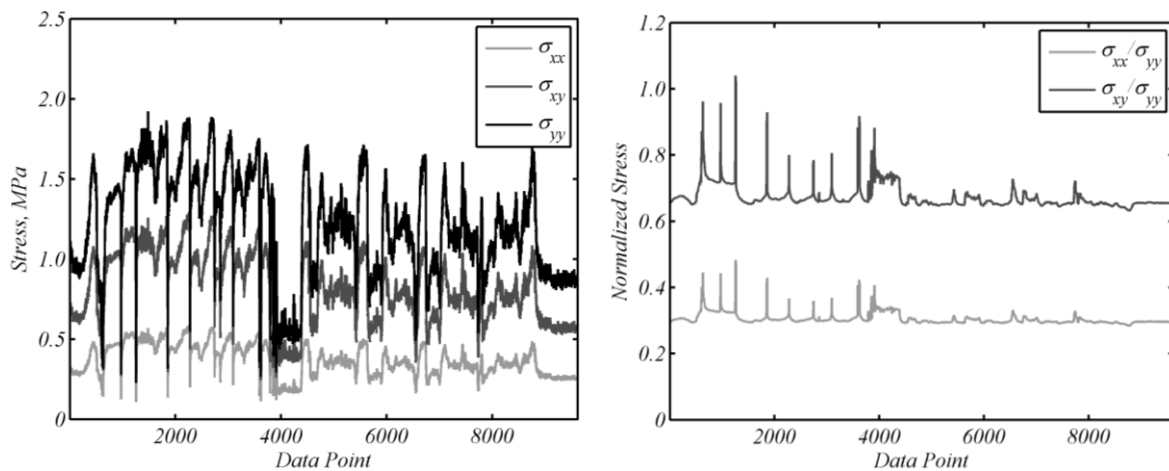


Figure D-18. Stress history for Flight ID 161. A) Bi-axial stress, B) Normalized stress.

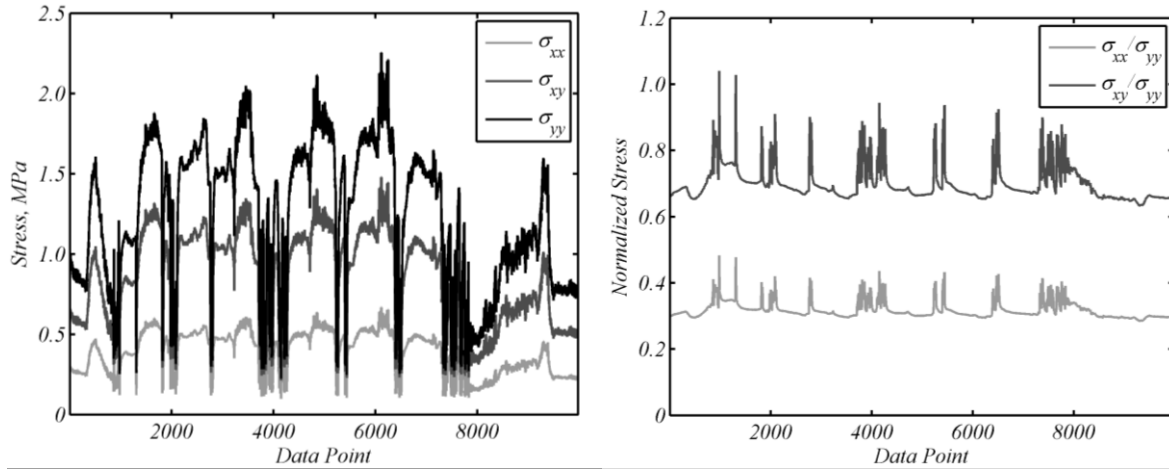


Figure D-19. Stress history for Flight ID 163. A) Bi-axial stress, B) Normalized stress.

LIST OF REFERENCES

1. "de Havilland Comet." *Wikipedia: The Free Encyclopedia*. Wikimedia Foundation, Inc. 25 Oct. 2011. Web. 25 Oct. 2011.
2. "1957 Cebu Douglas C-47 Crash." *Wikipedia: The Free Encyclopedia*. Wikimedia Foundation, Inc. 17 Mar. 2011. Web. 25 Oct. 2011.
3. "Los Angeles Airways Flight 417." *Wikipedia: The Free Encyclopedia*. Wikimedia Foundation, Inc. 8 Oct. 2011. Web. 25 Oct. 2011.
4. "Alexander L. Kielland (platform)." *Wikipedia: The Free Encyclopedia*. Wikimedia Foundation, Inc. 25 Aug. 2011. Web. 25 Oct. 2011.
5. "Japan Airlines Flight 123." *Wikipedia: The Free Encyclopedia*. Wikimedia Foundation, Inc. 22 Oct. 2011. Web. 25 Oct. 2011.
6. "Aloha Airlines Flight 243." *Wikipedia: The Free Encyclopedia*. Wikimedia Foundation, Inc. 3 Oct. 2011. Web. 25 Oct. 2011.
7. "United Airlines Flight 232." *Wikipedia: The Free Encyclopedia*. Wikimedia Foundation, Inc. 8 Oct. 2011. Web. 25 Oct. 2011.
8. "El Al Flight 1862." *Wikipedia: The Free Encyclopedia*. Wikimedia Foundation, Inc. 23 Sep. 2011. Web. 25 Oct. 2011.
9. "Eschede Train Disaster." *Wikipedia: The Free Encyclopedia*. Wikimedia Foundation, Inc. 1 Oct. 2011. Web. 25 Oct. 2011.
10. "China Airlines Flight 611." *Wikipedia: The Free Encyclopedia*. Wikimedia Foundation, Inc. 14 Oct. 2011. Web. 25 Oct. 2011.
11. "Chalk's Ocean Airways Flight 101." *Wikipedia: The Free Encyclopedia*. Wikimedia Foundation, Inc. Web.
12. ACC Public Affairs. *F-15 Eagle Accident Report Released*, 2008, available at <http://www.af.mil/news/story.asp?storyID=123081718>.
13. "Southwest Airlines Flight 2294." *Wikipedia: The Free Encyclopedia*. Wikimedia Foundation, Inc. 18 Apr. 2011. Web. 25 Oct. 2011.
14. Beden S, Abdullah S, Ariffin A. Review of fatigue crack propagation models in metallic components. *European Journal of Scientific Research* 2009; **28**(3):364-397.
15. Anderson TL. *Fracture Mechanics: Fundamentals and Applications*. CRC Press: Boca Raton, FL, 2004.

16. Nikishkov GP, Atluri SN. Calculation of fracture mechanics parameters for an arbitrary three-dimensional crack by the 'equivalent domain integral method'. *International Journal for Numerical Methods in Engineering* 1987; **24**(9):1801-1821.
17. Rice JR. A path independent integral and the approximate analysis of strain concentration by notches and cracks. *Journal of Applied Mechanics* 1968; **35**(2):379-386.
18. Shih C, Asaro R. Elastic-plastic analysis of crack on bimaterial interface: Part I - small scale yielding. *Journal of Applied Mechanics* 1988; **55**(2):299-316.
19. Yau J, Wang S, Corten H. A mixed-mode crack analysis of isotropic solids using conservation laws of elasticity. *Journal of Applied Mechanics* 1980; **47**(2):335-341.
20. Murakami Y, editor. *Stress Intensity Factors Handbook*. Pergamon Press: New York, 1987.
21. Sih GC. Strain-energy-density factor applied to mixed mode crack problems. *International Journal of Fracture* 1974; **10**(3):305-321.
22. Pais M, Kim NH, Davis TA. Reanalysis of the extended finite element method for crack initiation and propagation. *51st AIAA/ASME/ASCE/AHS/ASC Structures, Structural Dynamics, and Materials Conference*, Orlando, FL, 2010.
23. Chapra S, Canale R. *Numerical Methods for Engineers*. McGraw-Hill: New York, 2002.
24. Lu Z, Liu Y. Small time scale fatigue crack growth analysis. *International Journal of Fatigue* 2010; **32**(8):1306-1321.
25. Moës N, Dolbow JE, Belytschko T. A finite element method for crack growth without remeshing. *International Journal for Numerical Methods in Engineering* 1999; **46**(1):131-150.
26. Edke MS, Chang KH. Shape design sensitivity analysis (DSA) for structural fracture using extended FEM (XFEM). *International Journal of Pure and Applied Mathematics* 2008; **49**(3):365-372.
27. Xiaoping H, Moan T, Weicheng C. An engineering model of fatigue crack growth under variable amplitude loading. *International Journal of Fatigue* 2008; **30**(1):2-10.
28. Dabayeh AA, Topper TH. Changes in crack-opening stress after underload and overloads in aluminum alloy. *International Journal of Fatigue* 1995; **17**(4):261-269.

29. Ray A, Patankar R. Fatigue crack growth under variable amplitude loading: Part I - model formulation in state-space setting. *Applied Mathematical Modelling* 2001; **25**(11):979-994.
30. Ray A, Patankar R. Fatigue crack growth under variable-amplitude loading: Part II - code development and model validation. *Applied Mathematical Modelling* 2001; **25**(11):995-1013.
31. Huang XP, Moan T. Improved modeling of the effect of R-ratio on crack growth rate. *International Journal of Fatigue* 2007; **29**(4):591-602.
32. Ibrahim FK, Thompson JC, Topper TH. A study of effect of mechanical variables on fatigue crack closure and propagation. *International Journal of Fatigue* 1986; **8**(3):135-142.
33. Kujawski D. A fatigue crack driving force parameter with load ratio effects. *International Journal of Fatigue* 2001; **23**(S1):S239-S246.
34. Paris P, Gomez M, Anderson W. A rational analytic theory of fatigue. *The Trend in Engineering* 1961; **13**:9-14.
35. Shatil G, Ellison EG, Smith DJ. Elastic-plastic behavior and uniaxial low cycle fatigue life of notched specimens. *Fatigue and Fracture of Engineering Materials and Structures* 1995; **18**(2):235-245.
36. Zhang JZ, Halliday MD, Bowen P, Poole P. Three dimensional elastic-plastic finite element modelling of small fatigue crack growth under a single tensile overload. *Engineering Fracture Mechanics* 1999; **63**(3):229-251.
37. Elguedj T, Gravouil A, Combescure A. Appropriate extended function for X-FEM simulation of plastic fracture mechanics. *Computer Methods in Applied Mechanics and Engineering* 2006; **195**(7-8):501-515.
38. Elguedj T, Gravouil A, Combescure A. A mixed augmented Lagrangian-extended finite element method for modelling elastic-plastic fatigue crack growth with unilateral contact. *International Journal for Numerical Methods in Engineering* 2007; **71**(13):1569-1597.
39. Maligno AR, Rajaratnam S, Leen SB, Williams EJ. A three-dimensional (3D) numerical study of fatigue crack growth using remeshing techniques. *Engineering Fracture Mechanics* 2010; **77**(1):94-111.
40. Elices M, Guinea GB, Gomez J, Planas J. The cohesive model: Advantages, limitations and challenges. *Engineering Fracture Mechanics* 2002; **69**(2):137-163.
41. Moody NR, Reedy ED, Kent MS. *Physical basis for interfacial traction-separation laws*. Sandia Report SAND2002-8567, Sandia National Laboratories, 2002.

42. Scheider I. Derivation of separation laws for cohesive models in the course of ductile fracture. *Engineering Fracture Mechanics* 2009; **76**(10):1450-1459.
43. Babuska I, Melenk JM. The partition of unity method. *International Journal for Numerical Methods in Engineering* 1998; **40**(4):727-758.
44. Osher S, Sethian J. Fronts propagating with curvature-dependent speed: Algorithms based on Hamilton-Jacobian formulations. *Journal of Computational Physics* 1988; **79**(1):12-49.
45. Mulder W, Osher S, Sethian J. Computing interface motion in compressible gas dynamics. *Journal of Computational Physics* 1992; **100**(2):209-228.
46. Sussman M, Smereka P, Osher S. A level set approach for computing solutions to incompressible two-phase flow. *Journal of Computational Physics* 1994; **114**(1):146-159.
47. Osher S, Fedkiw R. *Level Set Methods and Dynamic Implicit Surfaces*. Springer-Verlag: New York, 2002.
48. Osher S, Paragios N. *Geometric Level Set Methods in Imaging, Vision, and Graphics*. Springer-Verlag: New York, 1993.
49. Adalsteinsson D, Sethian J. A level set approach to a unified model for etching, deposition, and lithography I: Algorithms and two-dimensional simulations. *Journal of Computational Physics* 1995; **120**(1):128-144.
50. Adalsteinsson D, Sethian J. A level set approach to a unified model for etching, deposition, and lithography II: Three-dimensional simulations. *Journal of Computational Physics* 1995; **122**(1):348-366.
51. Adalsteinsson D, Sethian J. A level set approach to a unified model for etching, deposition, and lithography III: Redeposition, reemission, surface diffusion, and complex simulations. *Journal of Computational Physics* 1997; **138**(1):193-223.
52. Wang S, Wang M. Radial basis functions and level set method for structural topology optimization. *International Journal for Numerical Methods in Engineering* 2006; **65**(12):2060-2090.
53. Wang S, Lim K, Khoo B, Wang M. An extended level set method for shape and topology optimization. *Journal of Computational Physics* 2007; **221**(1):395-421.
54. Sukumar N, Chopp DL, Bèchet E, Moës N. Three-dimensional non-planar crack growth by a coupled extended finite element and fast marching method. *International Journal for Numerical Methods in Engineering* 2008; **76**(5):727-748.

55. Moës N, Cloirec M, Cartraud P, Remacle J-F. A computational approach to handle complex microstructure geometries. *Computer Methods in Applied Mechanics and Engineering* 2003; **192**(28-30):3163-3177.
56. Courant R, Friedrichs K, Lewy H. Über die partiellen differenzengleichungen der mathematischen physik. *Mathematische Annalen* 1928; **100**(1):32-74.
57. Stolarska M, Chopp DL, Moës N, Belytschko T. Modelling crack growth by level sets in the extended finite element method. *International Journal for Numerical Methods in Engineering* 2001; **51**(8):943-960.
58. Gravouil A, Moës N, Belytschko T. Non-planar 3D crack growth by the extended finite element and level sets - Part II: Level set update. *International Journal for Numerical Methods in Engineering* 2002; **53**(11):2569-2586.
59. Moës N, Gravouil A, Belytschko T. Non-planar 3D crack growth by the extended finite element and level sets - Part I: Mechanical model. *International Journal for Numerical Methods in Engineering* 2002; **53**(11):2549-2568.
60. Sukumar N, Chopp DL, Moran B. Extended finite element method and fast marching method for three-dimensional fatigue crack propagation. *Engineering Fracture Mechanics* 2003; **70**(1):29-48.
61. Belytschko T, Moës N, Usui S, Parimi C. Arbitrary discontinuities in finite elements. *International Journal for Numerical Methods in Engineering* 2001; **50**(4):993-1013.
62. Reddy JN. *An Introduction to the Finite Element Method*. McGraw-Hill: New York, 2005.
63. Belytschko T, Gracie R, Ventura G. A review of extended/generalized finite element methods for material modeling. *Modeling and Simulation in Materials Science and Engineering* 2009; **17**(4):1-24.
64. Karihaloo BL, Xiao QZ. Modelling of stationary and growing cracks in FE framework without remeshing: A state-of-the-art review. *Computers and Structures* 2003; **81**(3):119-129.
65. Yazid A, Abdelkader N, Adbelmadjid H. A state-of-the-art review of the X-FEM for computational fracture mechanics. *Applied Mathematical Modelling* 2009; **33**(12):4269-4282.
66. Fries T-P, Belytschko T. The extended/generalized finite element method: An overview of the method and its applications. *International Journal for Numerical Methods in Engineering* 2010; **84**(3):253-304.
67. Aquino W, Brigham JC, Earles CJ, Sukumar N. Generalized finite element method using proper orthogonal decomposition. *International Journal for Numerical Methods in Engineering* 2009; **79**(7):887-906.

68. Fries T-P, Byfut A, Alizada A, Cheng KW, Schröder A. Hanging nodes and XFEM. *International Journal for Numerical Methods in Engineering* 2010: n/a.
69. Bordas S, Nguyen PV, Dunant C, Nguyen-Dang H, Guidoum A. An extended finite element library. *International Journal for Numerical Methods in Engineering* 2006; **71**(6):703-732.
70. Sukumar N, Dolbow JE, Devan A, Yvonnet J, Chinesta F, Ryckelynck D, Lorong P, Alfaro I, Martínez MA, Cueto E, Doblarè M. Meshless methods and partition of unity finite elements. *International Journal of Forming Processes* 2005; **8**(4):409-427.
71. Belytschko T, Black T. Elastic crack growth in finite elements with minimal remeshing. *International Journal for Numerical Methods in Engineering* 1999; **45**(5):601-620.
72. Fleming M, Chu YA, Moran B, Belytschko T. Enriched element-free Galerkin methods for crack tip fields. *International Journal for Numerical Methods in Engineering* 1997; **40**(8):1483-1504.
73. Sukumar N, Prévost JH. Modeling quasi-static crack growth with the extended finite element method, Part I: Computer implementation. *International Journal of Solids and Structures* 2003; **40**(26):7513-7537.
74. Huang R, Sukumar N, Prévost JH. Modeling quasi-static crack growth with the extended finite element method, Part II: Numerical applications. *International Journal of Solids and Structures* 2003; **40**(26):7539-7552.
75. Sukumar N, Moës N, Moran B, Belytschko T. Extended finite element method for three-dimensional crack modelling. *International Journal for Numerical Methods in Engineering* 2000; **48**(11):1549-1570.
76. Nagashima T, Miura N. Elastic-plastic fracture analysis for surface cracks using X-FEM. *8th International Conference on Computational Plasticity*, Barcelona, Spain, 2005.
77. Zi G, Chen H, Xu J, Belytschko T. The extended finite element method for dynamic fractures. *Shock and Vibration* 2005; **12**(1):9-23.
78. Prabel B, Marie S, Combescure A. Using the X-FEM method to model the dynamic propagation and arrest of cleavage cracks in ferritic steel. *Engineering Fracture Mechanics* 2008; **75**(10):2985-3009.
79. Rozycki P, Moës N, Bèchet E, Dubois C. X-FEM explicit dynamics for constant strain elements to alleviate mesh constraints on internal or external boundaries. *Computer Methods in Applied Mechanics and Engineering* 2008; **197**(30-32):349-363.

80. R  thor   J, Gravouil A, Combescure A. An energy-conserving scheme for dynamic crack growth using the extended finite element method. *International Journal for Numerical Methods in Engineering* 2005; **63**(5):631-659.
81. Zamani A, Eslami MR. Implementation of the extended finite element method for dynamic thermoeleastic fracture initiation. *International Journal of Solids and Structures* 2010; **47**(10):1392-1404.
82. Hutchinson JW. Singular behavior at the end of a tensile crack in a hardening material. *Journal of Mechanics and Physics of Solids* 1968; **16**(1):13-31.
83. Rice JR, Rosengren GF. Plane strain deformation near a crack tip in a power-law hardening material. *Journal of Mechanics and Physics of Solids* 1968; **16**(1-12).
84. Anderson MR. Fatigue Crack Initiation and Growth in Ship Structures. *Ph.D. Thesis, Department of Naval Architecture and Offshore Engineering*, Technical University of Denmark, 1998.
85. Sukumar N, Huang ZY, Pr  vost JH, Suo Z. Partition of unity enrichment for bimaterial interface cracks. *International Journal for Numerical Methods in Engineering* 2004; **59**(8):1075-1102.
86. Mo  s N, Belytschko T. Extended finite element method for cohesive crack growth. *Engineering Fracture Mechanics* 2002; **69**(7):813-833.
87. Unger JF, Eckardt S, K  nke C. Modelling of cohesive crack growth in concrete structures with the extended finite element method. *Computer Methods in Applied Mechanics and Engineering* 2007; **196**(41-44):4087-4100.
88. Zi G, Belytschko T. New crack-tip elements for XFEM and applications to cohesive cracks. *International Journal for Numerical Methods in Engineering* 2003; **57**(15):2221-2240.
89. Daux C, Mo  s N, Dolbow JE, Sukumar N, Belytschko T. Arbitrary branched and intersecting cracks with the extended finite element method. *International Journal for Numerical Methods in Engineering* 2000; **48**(12):1741-1760.
90. Dolbow JE, Mo  s N, Belytschko T. An extended finite element method for modeling crack growth with frictional contact. *Computer Methods in Applied Mechanics and Engineering* 2001; **190**(51-52):6825-6846.
91. Baietto MC, Pierres E, Gravouil A. A multi-model X-FEM strategy dedicated to frictional crack growth under cyclic fretting fatigue loadings. *International Journal of Solids and Structures* 2010; **47**(10):1405-1423.
92. Huang R, Pr  vost JH, Huang ZY, Suo Z. Channel-cracking of thin films with the extended finite element method. *Engineering Fracture Mechanics* 2003; **70**(18):2513-2526.

93. Huang Z, Suo Z, Xu G, He J, Prévost JH, Sukumar N. Initiation and arrest of an interfacial crack in a four-point bend test. *Engineering Fracture Mechanics* 2005; **72**(17):2584-2601.
94. Asadpoure A, Mohammadi S. Developing new enrichment functions for crack simulation in orthotropic media by the extended finite element method. *International Journal for Numerical Methods in Engineering* 2006; **69**(10):2150-2172.
95. Bèchet E, Scherzer M, Kuna M. Application of the X-FEM to the fracture of piezoelectric materials. *International Journal for Numerical Methods in Engineering* 2008; **77**(11):1535-1565.
96. Mousavi SE, Grinspun E, Sukumar N. Harmonic enrichment functions: A unified treatment of multiple, intersecting and branched cracks in the extended finite element method. *International Journal for Numerical Methods in Engineering* 2011; **85**(10):1306-1322.
97. Dolbow JE, Moës N, Belytschko T. Modeling fracture in Mindlin-Reissner plates with the extended finite element method. *International Journal of Solids and Structures* 2000; **37**(48-50):7161-7183.
98. Bachene M, Tiberkak R, Rechak S. Vibration analysis of cracked plates using the extended finite element method. *Archive of Applied Mechanics* 2009; **79**(3):249-262.
99. Rabinovich D, Givoli D, Vigdergauz S. XFEM-based crack detection scheme using a genetic algorithm. *International Journal for Numerical Methods in Engineering* 2007; **71**(9):1051-1080.
100. Rabinovich D, Givoli D, Vigdergauz S. Crack identification by 'arrival time' using XFEM and a genetic algorithm. *International Journal for Numerical Methods in Engineering* 2009; **77**(3):337-359.
101. Waisman H, Chatzi E, Smyth AW. Detection and quantification of flaws in structures by the extended finite element method and genetic algorithms. *10th US National Congress on Computational Mechanics*, Columbus, OH, 2009.
102. Fries T-P. A corrected XFEM approximation without problems in blending elements. *International Journal for Numerical Methods in Engineering* 2007; **75**(5):503-532.
103. Laborde P, Pommier J, Renard YS, M. High-order extended finite element method for cracked domains. *International Journal for Numerical Methods in Engineering* 2005; **64**(3):354-381.

104. Stazi FL, Budyn E, Chessa J, Belytschko T. An extended finite element method with higher-order elements for curved cracks. *Computational Mechanics* 2003; **31**(2-3):38-48.
105. Ventura G, Gracie R, Belytschko T. Fast integration and weight function blending in the extended finite element method. *International Journal for Numerical Methods in Engineering* 2008; **77**(1):1-29.
106. Tarancon J, Vercher A, Giner E, Fuenmayor J. Enhanced blending elements for XFEM applied to linear elastic fracture mechanics. *International Journal for Numerical Methods in Engineering* 2008; **77**(1):126-148.
107. Chanine E, Laborde P, Renard Y. Crack tip enrichment in the XFEM using a cutoff function. *International Journal for Numerical Methods in Engineering* 2008; **75**(6):629-646.
108. Chessa J, Wang H, Belytschko T. On the construction of blending elements for local partition of unity enriched finite elements. *International Journal for Numerical Methods in Engineering* 2003; **57**(7):1015-1038.
109. Ventura G, Moran B, Belytschko T. Dislocation by partition of unity. *International Journal for Numerical Methods in Engineering* 2005; **62**(11):1463-1487.
110. Bèchet E, Minnebo H, Moës N, Burgardt B. Improved implementation and robustness study of the X-FEM for stress analysis around cracks. *International Journal for Numerical Methods in Engineering* 2005; **64**(8):1033-1056.
111. Krongauz Y, Belytschko T. EFG approximation with discontinuous derivatives. *International Journal for Numerical Methods in Engineering* 1998; **41**(7):1215-1233.
112. Pais M, Kim NH, Peters J. Discussion on modeling weak discontinuities independent of the finite element mesh. *10th US National Congress on Computational Mechanics*, Columbus, OH, 2009.
113. Sukumar N, Chopp DL, Moës N, Belytschko T. Modeling holes and inclusions by level sets in the extended finite-element method. *Computer Methods in Applied Mechanics and Engineering* 2001; **190**(46-47):6183-6200.
114. Zilian A, Fries T-P. A localized mixed-hybrid method for imposing interfacial constraints in the extended finite element method (XFEM). *International Journal for Numerical Methods in Engineering* 2009; **79**(6):733-752.
115. Pais M, Kim NH. Modeling failure in composite materials with the extended finite element and level set method. *50th AIAA/ASME/ASCE/AHS/ASC Structures, Structural Dynamics, and Materials Conference*, Palm Springs, CA, 2009.

116. Dolbow JE, Merle R. Solving thermal and phase change problems with the extended finite element method. *Computational Mechanics* 2002; **28**(5):339-350.
117. Ji H, Dolbow JE. On strategies for enforcing interfacial constraints and evaluating jump conditions with the extended finite element method. *International Journal for Numerical Methods in Engineering* 2004; **61**(14):2508-2535.
118. Chessa J, Smolinski P, Belytschko T. The extended finite element method (XFEM) for Stefan problems. *International Journal for Numerical Methods in Engineering* 2002; **53**(8):1959-1977.
119. Hettich T, Hund A, Ramm E. Modeling of failure in composites by X-FEM and level sets within a multiscale framework. *Computer Methods in Applied Mechanics and Engineering* 2008; **197**(5):414-424.
120. Hettich T, Ramm E. Interface material failure modeled by the extended finite-element method and level sets. *Computer Methods in Applied Mechanics and Engineering* 2006; **195**(37-40):4753-4767.
121. Mousavi SE, Sukumar N. Generalized gaussian quadrature rules for discontinuities and crack singularities in the extended finite element method. *Computer Methods in Applied Mechanics and Engineering* 2010; **199**(49-52):3237-3249.
122. Mousavi SE, Sukumar N. Generalized Duffy transformation for integrating vertex singularities. *Computational Mechanics* 2010; **45**(2-3):127-140.
123. Natarajan S, Mahapatra DR, Bordas S. Integrating strong and weak discontinuities without integration subcells and example applications in an XFEM/GFEM framework. *International Journal for Numerical Methods in Engineering* 2010; **83**(3):269-294.
124. Yamada T, Nagashima T. A simple and efficient hybrid numerical quadrature scheme for structured extended FEM. *10th US National Congress on Computational Mechanics*, Columbus, OH, 2009.
125. Park K, Pereira JP, Duarte C, Paulino GH. Integration of singular enrichment functions in the generalized/extended finite element method for three-dimensional problems. *International Journal for Numerical Methods in Engineering* 2008; **78**(10):1220-1257.
126. Global Engineering and Materials, Inc. *Computational Software Development*, 2008, available at <http://www.gem-consultant.com/Demo.aspx>.
127. Dassault Systemes. *Abaqus 6.9 Extended Functionality (6.9-EF) Overview - November 2009*, 2009, available at http://www.simulia.com/download/Webinars/6.9_EF/.

128. Dassault Systemes. *Abaqus 6.9 Overview - June 2009*, 2009, available at http://www.simulia.com/download/Webinars/Abaqus69_overview/Abaqus69Overview-new.html.
129. Giner E, Sukumar N, Tarancon J, Fuenmayor J. An Abaqus implementation of the extended finite element method. *Engineering Fracture Mechanics* 2009; **76**(3):347-368.
130. Hansbo A, Hansbo P. A finite element method for the simulation of strong and weak discontinuities in solid mechanics. *Computer Methods in Applied Mechanics and Engineering* 2004; **193**(33-35):3524-3540.
131. Song J-H, Areias PMA, Belytschko T. A method for dynamic crack and shear band propagation with phantom nodes. *International Journal for Numerical Methods in Engineering* 2006; **67**(6):868-893.
132. Rabczuk T, Zi G, Gerstenberger A, Wall WA. A new crack tip element for the phantom-node method with arbitrary cohesive cracks. *International Journal for Numerical Methods in Engineering* 2008; **75**(5):577-599.
133. Liu Y, Mahadevan S. Threshold stress intensity factor and crack growth rate prediction under mixed-mode loading. *Engineering Fracture Mechanics* 2007; **74**(3):332-345.
134. Pais, M. *2D MATLAB XFEM Codes*, 2010, available at <http://www.matthewpais.com/2Dcodes>.
135. Rhee H, Salama M. Mixed-mode stress intensity factors solutions for a warped surface flaw by three-dimensional finite element analysis. *Engineering Fracture Mechanics* 1987; **28**(2):203-209.
136. Tanaka K. Fatigue crack propagation from a crack inclined to the cyclic tension axis. *Engineering Fracture Mechanics* 1974; **6**(3):493-507.
137. Yan X, Zhang Z. Mixed mode criteria for the materials with different yield strengths in tension and compression. *Engineering Fracture Mechanics* 1992; **42**(1):109-116.
138. Viana, FAC. *SURROGATES Toolbox User's Guide, Version 2.1*, 2010, available at <http://sites.google.com/site/fchegury/surrogatestoolbox>.
139. Cenaero. *Morfeo*, 2010, available at http://www.cenaero.be/Page_Generale.asp?DocID=21686&la=1&langue=EN.
140. Shi J, Chopp DL, Lua J, Sukumar N, Belytschko T. Abaqus implementation of extended finite element method using a level set representation for three-dimensional fatigue crack growth and life predictions. *Engineering Fracture Mechanics* 2010; **77**(14):2840-2863.

141. Wyart E, DufLOT M, Coulon D, Martiny P, Pardoën T, Remacle J-F, Lani F. Substructuring FE-XFE approaches applied to the three-dimensional crack propagation. *Journal of Computational and Applied Mechanics* 2008; **215**(2):626-638.
142. Renard, Y, Pommier, J. *Getfem++*, 2010, available at <http://download.gna.org/getfem/html/homepage>.
143. Bordas, S. *Downloads*, 2010, available at <http://people.civil.gla.ac.uk/~bordas/codes.html>.
144. Cherepanov GP. The propagation of cracks in a continuous medium. *Journal of Applied Mathematics and Mechanics* 1967; **31**(3):503-512.
145. Westergaard I. Bearing pressures and cracks. *Journal of Applied Mechanics* 1939; **6**(1):49-53.
146. Williams M. On the stress distribution at the base of a stationary crack. *Journal of Applied Mechanics* 1957; **24**(1):109-114.
147. Duarte C, Hamzeh OH, Lyszka TJ, Tworzydło WW. A generalized finite element method for the simulation of three-dimensional dynamic crack propagation. *Computer Methods in Applied Mechanics and Engineering* 2001; **190**(15-17):2227-2262.
148. Lua J, Shi J, Lu Z, Liu Y. Life prediction of aerospace structures by combined XFEM and advanced fatigue models. *51st AIAA/ASME/ASCE/AHS/ASC Structures, Structural Dynamics, and Materials Conference*, Orlando, FL, 2010.
149. Liu XY, Xiao QZ, Karihaloo BL. XFEM for direct evaluation of mixed mode SIFs in homogenous and bi-materials. *International Journal for Numerical Methods in Engineering* 2004; **59**(8):1103-1118.
150. Bilby BA, Cardew GE. The crack with a kinked tip. *International Journal of Fracture* 1975; **11**(4):708-712.
151. Erdogan F, Sih GC. On the crack extension in plates under plane loading and transverse shear. *Journal of Basic Engineering* 1963; **85**:519-525.
152. Nuismer RJ. An energy release rate criterion for mixed mode fracture. *International Journal of Fracture* 1975; **11**(2):708-712.
153. Richard HA, Fulland M, Sander M. Theoretical crack path prediction. *Fatigue and Fracture of Engineering Materials and Structures* 2005; **28**(1-2):3-12.
154. Feng M, Ding F, Jiang Y. A study of loading path influence on fatigue crack growth under combined loading. *International Journal of Fatigue* 2006; **28**(1):19-27.

155. Guidault P-A, Allix O, Champaney L, Cornuault C. A multiscale extended finite element method for crack propagation. *Computer Methods in Applied Mechanics and Engineering* 2008; **197**(5):381-399.
156. Sun CT. *Mechanics of Aircraft Structures*. John Wiley and Sons: Hoboken, 2006.
157. Tanaka K, Nakai Y, Yamashita M. Fatigue growth threshold of small cracks. *International Journal of Fatigue* 1981; **17**(5):519-533.
158. Dassault Systemes. *Dassault Systemes Accelerates Exploration of Real-World Product Performance with Abaqus 6.10-EF*, 2010, available at <http://www.3ds.com/company/news-media/press-releases-detail/release/dassault-systemes-accelerates-exploration-of-real-world/single/3233/?cHash=88be0d34424cf37fc71fb63619e5849d>.
159. Langlais TE, Vogel JH, Chase TR. Multiaxial cycle counting for critical plane methods. *International Journal of Fatigue* 2003; **25**(7):641-647.
160. Laborde P, Pommier J, Renard Y, Salaün M. High-order extended finite element method for cracked domains. *International Journal for Numerical Methods in Engineering* 2005; **64**(3):354-381.
161. Khosrovanah AK, Dowling NE. Fatigue loading history reconstruction based on the rainflow technique. *International Journal of Fatigue* 1990; **12**(2):99-106.
162. Rice RC, editor. *Fatigue Design Handbook*. Society of Automotive Engineers: Warrendale, 1997.
163. Rychlik I. A new definition of the rainflow cycle counting method. *International Journal of Fatigue* 1987; **9**(2):119-121.
164. Rychlik I. Simulation of load sequences from rainflow matrices: Markov method. *International Journal of Fatigue* 1996; **18**(7):429-438.
165. Collins JA. *Failure of Materials in Mechanical Design: Analysis, Prediction, Prevention*. John Wiley and Sons: New York, 1993.
166. Nieslony A. Determination of fragments of multiaxial service loading strongly influencing the fatigue of machine components. *Mechanical Systems and Signal Processing* 2009; **23**(8):2712-2721.
167. Nieslony, A. *Rainflow for MATLAB*, 2010, available at http://www.mathworks.com/matlabcentral/fox_files/3026/3/content/index.html.
168. Karolczuk A, Macha E. A review of critical plane orientation in multiaxial fatigue failure criteria of metallic materials. *International Journal of Fracture* 2005; **134**(3-4):267-304.

169. Papadopoulos IV, Davoli P, Foria C, Fillippini M, Bernasconi A. A comparative study of multiaxial high-cycle fatigue criteria for metals. *International Journal of Fatigue* 1997; **19**(3):219-235.
170. Pitoiset X, Preumont A. Spectral methods for multiaxial random fatigue analysis of metallic structures. *International Journal of Fatigue* 2000; **22**(7):541-550.
171. Wang CH, Brown MW. Life prediction techniques for variable amplitude multiaxial fatigue - Part I: theories. *Journal of Engineering Materials and Technology* 1996; **118**(3):367-370.
172. Wang CH, Brown MW. Life prediction techniques for variable amplitude multiaxial fatigue - Part II: comparison with experimental results. *Journal of Engineering Materials and Technology* 1996; **118**(3):371-374.
173. Newman JC. *FASTRAN II - A fatigue crack growth structural analysis program*. NASA 104159, NASA, 1992.
174. Myers R. *Classical and Modern Regression with Applications*. Duxbury Thomson Learning: Pacific Grove, 2000.
175. Kleijnen J. Kriging metamodeling in simulation: A review. *European Journal of Operational Research* 2009; **182**(3):707-716.
176. Martin J, Simpson T. Use of kriging models to approximate deterministic computer models. *AIAA Journal* 2005; **43**(4):853-863.
177. Stein M. *Interpolation of Spatial Data: Some Theory for Kriging*. Springer: New York, 1999.
178. Cheng B, Titterton D. Neural networks: A review from a statistical perspective. *Statistical Science* 1994; **9**(1):2-54.
179. Smola A, Scholkopf B. A tutorial on support vector regression. *Statistics and Computing* 2004; **14**(3):199-222.
180. Tada H, Paris P, Irwin G. *The Stress Analysis of Cracks Handbook*. ASME Press: New York, 1987.
181. Murakami Y. *Stress Intensity Factors Handbook*. Pergamon Press: New York, 1987.
182. Waisman H, Chatzi E, Smyth AW. Detection and quantification of flaws in structures by the extended finite element method and genetic algorithms. *International Journal for Numerical Methods in Engineering* 2009; **82**(3):303-328.
183. Abu Kassim AM, Topping BHV. Static renalysis: A review. *Journal of Structural Engineering* 1987; **113**(5):1029-1045.

184. Wu B, Li Z. Static reanalysis of structures with added degrees of freedom. *Communications in Numerical Methods in Engineering* 2006; **22**(4):269-281.
185. Wu B, Lim C, Li Z. A finite element algorithm for reanalysis of structures with added degrees of freedom. *Finite Elements in Analysis and Design* 2004; **40**(13-14):1791-1801.
186. Sherman J, Morisson W. Adjustment of an inverse matrix corresponding to a change in one element of a given matrix. *Annals of Mathematical Statistics* 1950; **21**:124-127.
187. Li Z, Lim C, Wu B. A comparison of several reanalysis methods for structural layout modifications with added degrees of freedom. *Structural and Multidisciplinary Optimization* 2008; **36**(4):403-410.
188. Chen Y, Davis TA, Hager WW, Rajamanickam S. Algorithm 887: CHOLMOD, supernodal sparse Cholesky factorization and update/downdate. *ACM Transactions on Mathematical Software* 2009; **35**(3):1-14.
189. Davis TA. *Direct Methods for Sparse Linear Systems*. Society of Industrial and Applied Mathematics: Philadelphia, 2006.
190. Davis, TA. *CHOLMOD: Supernodal Sparse Cholesky Factorization and Update/Downdate*, 2010, available at <http://www.cise.ufl.edu/research/sparse/cholmod/>.
191. Davis TA, Hager WW. Modifying a sparse Cholesky factorization. *SIAM Journal on Matrix Analysis and Applications* 1999; **20**(3):606-627.
192. Davis TA, Hager WW. Multiple-rank modifications of a sparse Cholesky factorization. *SIAM Journal on Matrix Analysis and Applications* 2001; **22**(4):997-1013.
193. Davis TA, Hager WW. Row modifications of a sparse Cholesky factorization. *SIAM Journal on Matrix Analysis and Applications* 2005; **26**(3):621-639.
194. Davis TA, Hager WW. Dynamic supernodes in sparse Cholesky update/downdate and triangular solves. *ACM Transactions on Mathematical Software* 2009; **35**(4):1-23.
195. Amestoy M, Davis TA, Duff IS. An approximate minimum degree ordering algorithm. *SIAM Journal on Matrix Analysis and Applications* 1996; **17**(4):886-905.
196. Amestoy P, Davis TA, Duff IS. Algorithm 837: AMD, an approximate minimum degree ordering algorithm. *ACM Transactions on Mathematical Software* 2004; **30**(3):381-388.

197. "g-Force." *Wikipedia: The Free Encyclopedia*. Wikimedia Foundation, Inc. 21 Oct. 2011. Web. 25 Oct. 2011.
198. Aerospace Web. *Bank Angle and G's*, 2010, available at <http://www.aerospaceweb.org/question/performance/q0146.shtml>.
199. "Banked Turn." *Wikipedia: The Free Encyclopedia*. Wikimedia Foundation, Inc. 15 Oct. 2011. Web. 25 Oct. 2011.
200. Boeing. *767 Family - Technical Information*, 2010, available at <http://www.boeing.com/commercial/767family/specs.html>.
201. "Jet Fuel." *Wikipedia: The Free Encyclopedia*. Wikimedia Foundation, Inc. 23 Oct. 2011. Web. 25 Oct. 2011.
202. "Angle of Attack." *Wikipedia: The Free Encyclopedia*. Wikimedia Foundation, Inc. Web.
203. Pippy R. Approximate Probabilistic Optimization of a Wingbox Model Using Exact-Capacity-Approximate-Response-Distribution (ECARD). *M.S. Thesis, Mechanical Engineering*, University of Florida, 2008.
204. Choklovshi, T. *Pointed-tip wings at low Reynolds numbers*, 2011, available at <http://www-scf.usc.edu/~tchklovs/Proposal.htm>.
205. Lobert G. Spanwise lift distribution of forward and aft-swept wings in comparison to the optimum distribution form. *Journal of Aircraft* 1981; **18**(6):496-498.
206. NASA. *Inclination effects on lift*, 2010, available at <http://www.grc.nasa.gov/WWW/K-12/airplane/incline.html>.
207. Rocket and Space Technology. *Drag Coefficient*, 2011, available at <http://www.braeunig.us/space/cd.htm>.
208. "Lift (force)." *Wikipedia: The Free Encyclopedia*. Wikimedia Foundation, Inc. 24 Oct. 2011. Web. 25 Oct. 2011.
209. He MY, Hutchinson JW, Becher PF. Crack deflection at an interface between dissimilar elastic materials. *International Journal for Solids and Structures* 1989; **25**(9):1053-1067.
210. He MY, Hsueh CH, Becher PF. Deflection versus penetration of a wedge-loaded crack: Effects of branch-crack length and penetrated-layer width. *Composites: Part B* 2000; **31**(4):299-308.
211. Zhang Z, Suo Z. Split singularities and the competition between crack penetration and debond at a bimaterial interface. *International Journal of Solids and Structures* 2007; **44**(13):4559-4573.

212. He JW, Li N, Jia M, Wen SP, Jia RP. Effect of interface layer on fatigue crack growth in an aluminum laminate. *Fatigue and Fracture of Engineering Materials and Structures* 2004; **27**(3):171-176.
213. Kao-Walter S, Ståhle P, Chen SH. A finite element analysis of a crack penetrating or deflecting into an interface in a thin laminate. *Key Engineering Materials* 2006; **312**:173-178.
214. Archard JF. Contact and rubbing of flat surfaces. *Journal of Applied Physics* 1953; **24**(8):981-988.
215. Mukras S, Kim NH, Sawyer WG, Jackson DB, Bergquist LW. Numerical integration schemes and parallel computation of wear prediction using finite element method. *Wear* 2009; **266**(7-8):822-831.
216. Sutradhar A, Paulino GH, Gray LJ. *Symmetric Galerkin Boundary Element Method*. Springer-Verlag: Heidelberg, 2008.

BIOGRAPHICAL SKETCH

Matthew Jon Pais graduated from the University of Missouri in 2007 magna cum laude and honors scholar with a Bachelor of Science in Mechanical Engineering. As an undergraduate student he participated in a National Science Foundation sponsored Research Experience for Undergraduates (REU) at the University of Missouri at Rolla and worked as an undergraduate research assistant which resulted in the undergraduate honors thesis, *Hydroxyapatite Reinforced Dental Composites*. He joined the University of Florida in 2007 after receiving the Alumni Fellowship where he worked with Dr. Nam-Ho Kim on his Ph.D. in Mechanical Engineering. He spent the summer of 2010 at the Idaho National Laboratory where he modeled failure by liquid metal embrittlement. He received his Ph.D. from the University of Florida in the fall of 2011.